Design of Impurity Influx Monitor (Divertor) for ITER

Hiroaki OGAWA, Tatsuo SUGIE
Atsushi KATSUNUMA* and Satoshi KASAI

Tokamak Diagnostic Group
Fusion Research and Development Directorate

JAEA-Technology

Design of Impurity Influx Monitor (Divertor) for ITER

Hiroaki OGAWA, Tatsuo SUGIE※, Atsushi KATSUNUMA* and Satoshi KASAI

Division of Advanced Plasma Research
Fusion Research and Development Directorate
Japan Atomic Energy Agency
Naka-shi, Ibaraki-ken

Because of the changes of interfaces between ITER and the Impurity Influx Monitor (divertor) accompanied with the change of the ITER design to a reduced size machine, changes in the design of the monitor are required. In this design work, optics compatible with new interfaces, a calibration system and an alignment system of the optical axis and the focus were designed and investigated. The design of the optical systems was simplified to save the cost. To simplify the optics, the design of the collection optics was changed from an off-axis aspherical mirror system, which is a previous design, to a simple Cassegrain telescope system composed of simple spherical mirrors and lenses. In addition, a micro lens array is inserted just in front of the fiber bundle to increase the light detected. The ray-trace analysis shows that the spatial resolution of ITER requirement (50 mm) will be achieved by these optical systems designed here. The in-situ sensitivity calibration will be realized by applying the light on a micro retro-reflector array installed in front of the plasma facing first mirror from the outside the vacuum chamber through the same optics for plasma measurement and measuring the intensity of the reflected light from the array by using the same optics. In addition, optical design of an adjustment system and a focusing system, and a conceptual design of the shutter system of the monitor were carried out. Moreover, the detector system for the monitor was investigated and designed.

※ ITER-IT Naka
* NIKON Corporation

ITER 用ダイバータ不純物モニターの設計

日本原子力研究開発機構

核融合研究開発部門 先進プラズマ研究開発ユニット

小川　宏明、杉江　達夫※、勝沼　淳*、河西　敏

　　　ITER の設計変更に伴い、ダイバータ不純物モニターと ITER 間のインターフェイスが変わり、ダイバータ不純物モニターの光学系の設計を変更することが必要となった。今回の光学設計では、新しいインターフェイスに則したプラズマ計測用光学系、感度較正用光学系、光軸調整用光学系及びピント調整用光学系のそれぞれについて光学設計を行った。光学設計に際しては、使用する光学素子を共通化することによる製作コストの削減をはかった。製作コストの低減に向けて、前回の設計で採用した軸外し非球面鏡の集光光学系を凹面鏡と補正レンズから構成されるカセグレンテレスコープへと変更して、光学素子の簡素化を図った。また、集光光学系の結像面にマイクロレンズアレイを設置して、測定視野を拡げることにより、検出する光量を増加させることができる光学系とした。光線追跡法による解析を行って、ITERで要求されている空間分解能 (50 mm) を満たすことができる光学系を設計することができた。感度較正用光学系については、プラズマを直視する第一ミラーの前面にマイクロリトローリフレクターアレイを設置し、標準光源からの光をプラズマ測定用光学系に入射してアレイに当て、その反射光を測定することにより測定用光学系のその場感度較正が可能であることを示した。さらに、第一ミラーの前面に設置するシャッターの概念設計及び検出系の設計検討を実施した。

那珂核融合研究所（駐在）：〒311-0193　茨城県那珂市向山 801-1

※ ITER 国際チーム・那珂

* （株）ニコン

Contents

目　　次

1. Introduction

The main function of the Impurity Influx Monitor (divertor) is to measure the parameters of impurities and isotopes of hydrogen (tritium, deuterium and hydrogen) in the divertor plasmas by using spectroscopic techniques in the wavelength range of 200 - 1000 nm. The detailed requirements are shown in Table 1-1 and references [1-1, 2]. The expected impurities are carbon, tungsten, beryllium and copper originating from the divertor target plate and from the surface of the first wall in the main chamber. Neon, argon, krypton or other impurity gases injected into the plasma for radiation cooling in the divertor and the plasma edge will also be observed [1-3].

In the divertor plasma, many spectral lines from neutral and ionized atoms are emitted from vacuum ultraviolet to visible region due to low electron temperature and high electron density. In present tokamak experiments, visible spectrometer is used to study the divertor plasma, because no vacuum extension is necessary. In ITER divertor diagnostics, same technologies can be applied except that the measurements are required for the full duration of the ITER pulse (> 600 s) and special provisions are necessary to measure in the harsh environment for diagnostic components.

The ITER international team and the Japan Home Team (Japan Participant Team) had designed the Impurity Influx Monitor (divertor) during the EDA and CDA phases [1-4~8]. Because the machine size of ITER was reduced after EDA phase, interfaces between ITER and the monitor changed. In order to install in the present ITER, changes in the design of the monitor are required.

In this report, details of new optical design compatible with new interface are described. In addition, a calibration system, alignment systems of the optical axis and the focus, and are discussed. Moreover, conceptual design of shutter is reported. Finally, design of optical detectors and data acquisition system is reported.

2. Design of Optics

2.1 Overview of the System

Impurity Influx Monitor (divertor) observes divertor region using four optical systems; i) central optics with mirrors installed in the divertor cassette, ii) side optics through the gap between the divertor cassettes, iii) optics from the equatorial port, iv) optics from the upper port as shown in Figs. 2.1-1 and 2.1-2. Detailed viewing fans from the divertor cassette named IV, OV, IH and OH of central optics installed in the divertor cassette are also shown in Fig. 2.1-2. The two-dimensional measurement in the poloidal plane will be performed by using these four optical systems.

The four optical systems mentioned above are complementary to each other. The optical system with mirrors installed in the divertor cassette has a better spatial resolution along the divertor plates from the bottom to the top region of the plate, because the lines of sights are almost perpendicular to the plates. In addition, the signals are not affected by the emissions from the main plasma, because the lines of sights do not through the main plasma. However, the range of the observation is limited to a small area near the divertor

plate as shown in Fig. 2.1-2. The optical system through the gap between the divertor cassettes observes divertor plasmas from the strike point to the X-point, but does not observe the divertor plate itself.

The optical systems from the upper port and from the equatorial port will be able to observe large area of the divertor plasmas except the area near the inner and outer strike point, respectively. The lines of sights are almost parallel to the divertor plates as shown in Fig. 2.1-1. It causes the better spatial resolution in the horizontal direction but along the divertor plate.

In the previous design, the collection optics for each viewing fan was composed of off-axis aspherical mirrors and had different optical parameters. To simplify the optics, the design of the collection optics for Impurity Influx Monitor will be changed from an off-axis aspherical mirror system to a simple Cassegrain telescope system composed of simple spherical mirrors and lenses as shown in Fig. 2.1-3 and the collection optics for each viewing fan having same optical parameters. In addition, a micro lens array will be inserted just in front of the fiber bundle to increase the light detected as shown in Fig.2.1-4.This micro lens array is piled up many micro lens, which is thin spherical lens with thickness of 0.25 mm, length of 7.35 mm and width of 4 mm. The optical parameters for the collection optics are summarizes in Table 2.1-1.

2.2 Design of Optics from Divertor Port

2.2.1 Overview of the Optics from the Divertor Port

There are two optical systems in the divertor port. One is an optical system (named central optics) observing the plasma through the mirror optics installed in the central region of the divertor cassette. Another is an optical system (named side optics) observing the plasma through the gap between the divertor cassettes by using a mirror optics installed just behind the gap as shown in Fig. 2.2.1-1. Figure 2.2.1-2 is the enlarged view at the divertor cassette.

The central optics in the divertor cassette has four viewing fans named IV, OV, IH and OH as shown in Fig. 2.2.1-2. The IV and OV observe the inner and outer lower-side of the divertor plasma from the dome by using convex mirrors installed in the dome. The IH and OH observe the inner and outer upper-side of the divertor from the bottom by using convex mirrors installed in the bottom of the divertor cassette, respectively. Each viewing fan has baffle plates in front of the first mirror to reduce the particle bombardment on the first mirror.

The light from the each viewing fan is reflected by mirrors mounted in the aperture for exhausting and guided to the window on the end of the divertor port. After that, the light goes through the labyrinth in the biological shield, and then the light is focused on the corresponding micro lens array (43 channels) by the collection optics. The arrangement of micro lens arrays for each viewing fan is shown in Fig. 2.2.1-3. The micro lens (effective area: 0.25 mm × 2.0 mm) is made of fused silica. An optical fiber, which core diameter is 200 μm and the clad diameter is 250 μm, is attached on the end on the micro lens to guide the light to spectrometers.

By using the side optics through the gap between the divertor cassettes, we will be able to observe the plasma from the plasma strike points to the X-point. The light from the divertor plasma goes through the gap

and then the light is guided to the window on the end of the divertor port by a mirror system located near the backside of the divertor cassette. After that, the light goes through the labyrinth in the biological shield and then the light focused on the micro lens array (73 channels) by the collection optics. The following optics is same as that mentioned above.

2.2.2 Design of the Central Optics

Ray-trace analysis has been carried out by using the CODE V optical design software for each viewing fan. Traced rays are shown in Figs. 2.2.2-1, 2, 3 and 4 for IV, OV, IH and OH, respectively. Here, five lines of sight of F1, F2, F3, F4 and F5 among 43 channels were selected as typical lines of sight which correspond to the lines of sight started from the y=-5.25 mm, -2.5 mm, 0.0 mm, 2.5 mm and 5.25 mm at the micro lens array, respectively as shown in Fig.2.2.1-3.

The spot diagrams for the line of sight of F1, F2, F3, F4 and F5 on the divertor plate are shown in Figs. 2.2.2-5, 6, 7 and 8 for the viewing fan IV, OV, IH and OH, respectively. Here, the rays are emitted from the central point (indicated by cross in the figures) of the end of the micro lens. The result for the viewing fan OH was not so good. For the line of sight F5, the spot is spread up to 6 mm in the perpendicular direction but it still satisfies the requirement of spatial resolution of 50 mm. For other lines of sight, it seems that the simple optics with spherical mirrors has a sufficient performance.

The irradiance distribution has been analyzed in order to study the spatial resolution at the divertor plate for each line of sight. Here, we assume that the light is emitted from the area of the end of the micro lens (effective area: 0.25 mm × 2.0 mm) as shown in Fig. 2.2.2-9. The relative distributions of irradiances on the divertor plate for each line of sight have been calculated. The results are shown in Figs. 2.2.2-10, 11, 12 and 13 with contours for the viewing fan IV, OV, IH and OH, respectively. From the figures, the spatial resolution of 10 mm will be achieved for all viewing fans of the central optics. The results of the spatial resolutions are summarized in Table. 2.2.2-1.

Footprints of the rays started from 4 corners of the micro lens array (indicated in Fig.2.2.2-14) have been calculated for each surface in the optics to estimate the necessary areas of mirrors, apertures and windows of the penetration optics. Figures 2.2.2-14, 15 and 16 show the footprints on the mirror surfaces located at the entrance of the divertor cassette and at the dome, and on the window for the viewing fan IV, respectively. From these results, mirror and aperture sizes in the optics will be able to be decided.

Transmissivity and collecting solid angle for the central optics have been evaluated. The numbers of photons N_d (photons·s^{-1}) incident on the detector is

$$N_d = I_{div} \cdot T_{pe} \cdot T_f \cdot T_{sp} \cdot \Omega_d \cdot S_d$$
$$= I_{div} \cdot T_{pe} \cdot T_f \cdot T_{sp} \cdot \Omega_m \cdot S_m , \qquad (2.2.2-1)$$

where I_{div} is the intensity of the spectral line emitted in the divertor plasma, T_{pe} is the transmissivity of the optics from the divertor to the end of the fiber, T_f is the transmissivity of the fiber to the spectrometer, T_{sp} is

the transmissivity of the spectrometer, Ω_d is the effective solid angle to the optics at the divertor plasma, S_d is the area of the image of the micro lens, Ω_m is the effective solid angle on to the micro lens (collecting solid angle) and S_m is the area of the micro lens as shown in Fig. 2.2.2-17. In this design work, Ω_m and S_m are 8.465×10^{-4} sr, 5.0×10^{-7} m². T_{pe} which depends on wavelength is summarized in Table 2.2.2-2. Here, we use molybdenum (Mo) mirrors it the dome of the divertor cassette, aluminum (Al) mirrors for other mirrors and fused silica (SiO₂) windows and lenses. Other parameters T_{sp} and T_f are shown in the previous report [1-5, 6].

2.2.3 Design of the Side Optics

Two optical systems will be installed on the both sides of the divertor cassette. Ray-trace analysis has been carried out by using the CODE V for one of two optical systems, because each has a same optical arrangement. Traced rays are shown in Fig. 2.2.3-1. Here, F1, F2, F3, F4 and F5 correspond to the lines of sight started from the y = 9.0 mm, 4.5 mm, 0.0 mm, -4.5 mm and -9.0 mm at the micro lens array, respectively. The mirror arrangement and traced rays near the divertor is shown in Fig. 2.2.3-2.

The spot diagrams for the line of sight of F1, F2, F3, F4 and F5 on the imaginary plane (see Fig. 2.2.3-1(b)) located near the dome are shown in Figs. 2.2.3-3. Here, the rays are emitted from the center of the end of the optical fiber.

The irradiance distribution has been analyzed in order to study the spatial resolution at the imaginary plane for each line of sight. Here, we assume that the light is emitted from the area of the end of the micro lens (0.25 mm × 2.0 mm). The calculated irradiance distribution on the imaginary plane are shown in Fig. 2.2.3-4 by contours. It has been confirmed that the spatial resolution of 35 mm will be achieved for all lines of sight. The results of the spatial resolutions are also summarized in Table 2.2.2-1.

Footprints of the rays started from 4 corners of the micro lens array have been calculated to estimate the necessary areas of mirrors, apertures and windows of the penetration optics. Figures 2.2.3-5 and 6 show the footprints on the concave mirror surfaces located near the divertor cassette and on the window, respectively. From these results, mirror and aperture sizes in the optics will be able to be determined.

Trasmissivity and collecting solid angle for the side optics have been evaluated as same as the central optics. The values of Ω_m (=8.465×10^{-4} sr) and S_m (=5.0×10^{-7} m²) were used for the calculation. However, the effective S_m becomes small, because the width of the gap between the divertor cassettes is 10 mm. The trasmissivity of the penetration optics are summarized in Tables 2.2.3-1.

2.3 Design of Equatorial Port Optics and Upper Port Optics
2.3.1 Overview of Equatorial Port Optics and Upper Port Optics

These optical systems observe the divertor region from the equatorial port and the upper port as shown in Fig. 2.1-1. The light from the divertor plasma goes through the header optics in each port plug, and then is guided to the window on the end of each port. After that, the light goes through the labyrinth in the biological shield of each port, and then the light is focused on the micro lens array (71 channels) by the collection optics.

The micro lens (effective area: 0.25 mm × 2.0 mm) is made of fused silica. An optical fiber, which has a core diameter of 200 μm and a clad diameter of 250 μm, is attached on the end on the micro lens to guide the light to spectrometers.

2.3.2 Design of Equatorial Port Optics

Ray-trace analysis has been carried out by using the ZEMAX optical design software for the optics with a 71-channel micro lens array. Traced rays are shown in Fig. 2.3.2-1. Here, F1, F2, F3, F4 and F5 correspond to the lines of sight started from the y = 8.75 mm, 4.25 mm, 0.0 mm, -4.25 mm and -8.75 mm at the micro lens array, respectively. The mirror arrangement and traced rays near the header optics is also shown in Fig. 2.3.2-1(b) and Fig. 2.3.2-2.

The spot diagrams for the line of sight of F1, F2, F3, F4 and F5 on the imaginary plane (see Fig. 2.3.2-1(a)) located near the dome are shown in Fig. 2.3.2-3. Here, the rays are emitted from the center of the end of the micro lens.

The irradiance distribution has been analyzed in order to study the spatial resolution at the imaginary plane for each line of sight. Here, we assume that the light is emitted from the area of the end of the micro lens (effective area: 0.25 mm × 2.0 mm). The irradiance distribution on the imaginary plane for each line of sight has been calculated. The results are shown in Figs. 2.3.2-4 by contours for the optics with a 71-channel micro-lens array. It has been confirmed from the figures that the spatial resolution of 48 mm will be achieved for all lines of sight. The results of the spatial resolutions are summarized in Table 2.2.2-1.

Footprints of the rays started from 4 corners of the micro lens array have been calculated to estimate the necessary areas of mirror, apertures and windows of the penetration optics. Figures 2.3.2-5 and 2.3.2-6 show the footprints on the concave mirror surfaces located in the header optics and on the window, respectively. From these results, mirror and aperture sizes in the optics will be able to be determined.

As same as section 2.2.2, the effective solid angle on to the micro lens (collecting solid angle) Ω_m was 8.465×10^{-4} sr and S_m was 5.0×10^{-7} m^2.

The trasmissivity of the penetration optics from the equatorial port has been calculated similarly to those of the divertor optics and is summarized in Tables 2.3.2-1.

For the integration point of view, CAD work has been made in cooperation with ITER-IT at Garching JWS. As the result, it is confirmed that the equatorial port optics will be consistent with space allowed for integration. However, the detailed integration work and the minor modification of the optics will be needed.

2.3.3 Design of Upper Port Optics

Ray-trace analysis has been carried out by using the ZEMAX for the optics with a 71-channel micro lens array. Traced rays are shown in Fig. 2.3.3-1. Here, F1, F2, F3, F4 and F5 correspond to the lines of sight started from the y = 8.75 mm, 4.25 mm, 0.0 mm, -4.25 mm and -8.75 mm at the micro lens array, respectively (Fig. 2.3.3-1(a)).

The spot diagrams for the line of sight of F1, F2, F3, F4 and F5 on the imaginary plane located near the dome are shown in Figs. 2.3.3-2. Here, the rays are emitted from the center of the end of the micro lens.

The irradiance distribution has been analyzed in order to study the spatial resolution at the imaginary plane for each line of sight. Here, we assume that the light is emitted from the area of the end of the micro lens (effective area: 0.25 mm × 2.0 mm). The irradiance distribution on the imaginary plane for each line of sight has been calculated. The results are shown in Figs. 2.3.3-3 by contours. It has been confirmed from the figures that the spatial resolution of 37 mm will be achieved for all lines of sight. The results of the spatial resolutions are summarized in Table 2.2.2-1.

Footprints of the rays started from 4 corners of the micro lens array have been calculated to estimate the necessary areas of mirrors, apertures and windows of the penetration optics. Figures 2.3.3-4 and 2.3.3-5 show the footprints on the concave mirror surfaces located in the header optics and on the window, respectively. From these results, mirror and aperture sizes in the optics will be able to be determined.

As same as section 2.2.2, the effective solid angle on to the micro lens (collecting solid angle) Ω_m was 8.465×10^{-4} sr and S_m was 5.0×10^{-7} m^2.

The trasmissivity T_{pe} of the penetration optics from the upper port has been calculated similarly to those of the divertor optics and the trasmissivity is summarized in Table 2.3.3-1.

For the integration point of view, CAD work has been made in cooperation with ITER-IT at Garching JWS. As the result, it is confirmed that the upper port optics will be consistent with space allowed for integration. However, the detailed integration work and the minor modification of the optics will be needed.

2.4 Summary of Optical Performance and Issues

The optical performance for each viewing fan is described in the corresponding sections. In this section, the overall optical-performance will be summarized.

The estimated effective solid angles on to the micro lens (collecting solid angles) Ω_m are shown in Table 2.4-1 for each viewing fan. The effective solid angles are 8.465×10^{-4} sr for all optical systems. The value of Ω_m times S_m (Sectional area of the micro lens) is 4.23×10^{-10} sr·m^2 for each viewing fan. Table 2.4-2 shows the value of $T_{pe} \cdot \Omega_m \cdot S_m$ for each viewing fan at the wavelength of 300 nm. The values of $T_{pe} \cdot \Omega_m \cdot S_m$ are almost same as the previous design values. [1-6] Therefore, almost same signal strength will be obtained by these systems designed here.

Table 2.2.2-1 shows the summary result of the ray-trace analysis for the spatial resolution. The analysis indicates that the spatial resolutions performed by the central optics through mirrors in the divertor cassette, the side optics through the gap between the divertor cassettes, the equatorial port optics and the upper port optics will be ≤ 10 mm, ≤ 35 mm, ≤ 48 mm and ≤ 37 mm, respectively.

From the above description, the optics designed here will meet the ITER requirement for parameter ranges and for spatial resolutions. For the measurement accuracies, more detailed estimation should be necessary.

2.5 In-situ Calibration System

Optical components of ITER, such as mirrors, windows etc., mounted close to the plasma will be exposed to higher levels of radiation due to neutron, gamma-ray and/or particle irradiations than in present devices. An additional potential damaging effect for the first mirrors is the formation of coatings of impurities, such as Be, W, C, etc. due to erosion and re-deposition of the materials of the first wall and the divertor. Small amount of loose particles can form dust and this is also a potential problem especially for mirrors in the divertor. Measurements to minimize the degradation of their performance by these effects, such as changes in the reflectivity, have been studied. Protective and mitigating measurements are adopted in the system designs: for example, the plasma is viewed through a small aperture for the optics from an equatorial and an upper port, and baffle plates are inserted in front of the first mirror for the optical systems which have mirrors in the divertor cassette. However, it will not be possible to prevent the degradation completely.

In order to make the required measurements it is important to know the sensitivity of the optical systems and, since this may change due to the environmental effects, in-situ calibration is required. Table 2.5-1 shows the candidate in-situ sensitivity calibration methods for optical systems. It is not feasible to install a light source in the vacuum chamber of ITER during operations and so an alternative method is needed. In-situ and remote calibration methods, which will be installed in the strong radiation field, are required.

Here, an in-situ calibration system using a micro retro-reflector array is studied as a possible method. The scheme and detailed studies of the in-situ calibration system will be described and the remaining issues to be solved will be discussed in the following sections.

2.5.1 Scheme of Sensitivity Calibration

For the optics in the divertor cassette, micro retro-reflector arrays are installed between the baffle plates, where there is minimum neutral particle bombardment, located in front of the first mirror as shown in Fig. 2.5.1-1(a). For the optics in the upper and equatorial port, a micro retro-reflector array is installed on the shutter (Fig. 2.5.1-1(b)). Figure 2.5.1-2 shows a micro retro-reflector array. During the plasma operation, the micro retro-reflector array should be covered to prevent particle deposition as shown in Fig. 2.5.1-1(b). The micro retro-reflector array is moved to the front of the first mirror during the calibration.

Here, we use a micro retro-reflector array instead of a conventional retro-reflector so that almost all the incident light reflects back to the emission point through the spherical mirror installed in the header optics as a first mirror. Figure 2.5.1-3 compares schematically the reflected ray for a retro-reflector and a micro retro-reflector array. If we use a retro-reflector, almost all the incident light does not go back to the emission point.

During the installation phase of the ITER diagnostics, sensitivity calibration should be carried out with standard light sources set in front of the first mirror of each optics as shown in Fig. 2.5.1-4. On the other hand, during the operation phase of ITER, a standard light is set behind the biological shield or in the diagnostic

room and the light is applied to the micro retro-reflector array through the same optics as used in the plasma measurement. The reflected light is measured with a spectrometer or a detector to estimate the sensitivity change.

Three methods have been considered to apply the light on the micro retro-reflector array as below:

a) The light is introduced from the exit slit of a dedicated spectrometer for calibration, which has a suitable F number to the numerical aperture (NA) of the optical fiber, and then guided to the collection optics through an optical fiber. The light is applied on the micro retro-reflector array through the same optics for measurement. The reflected light comes back to the collection optics. The light is reflected by a half mirror located in the collection optics and leaded to a detector. (Fig. 2.5.1-5(a))

b) The light is introduced to an optical fiber by an optical splitter located between the spectrometer and the selector box, and then guided to the collection optics through an optical fiber. The light is applied on the micro retro-reflector array through the same optics for measurement. The reflected light comes back to the collection optics and focuses on the same end of the optical fiber. The light is leaded to the optical splitter by the optical fiber and to the spectrometer. (Fig. 2.5.1-5(b))

c) The light is introduced from the exit slit of a dedicated spectrometer for calibration, which has a suitable F number to NA of the optical fiber, and then guided to the collection optics through an optical splitter by an optical fiber. The light is applied on the micro retro-reflector array through the same optics for measurement. The reflected light comes back to the collection optics and focuses on the same end of the optical fiber. The light is leaded to the optical splitter by the optical fiber, and then to a detector. (Fig. 2.5.1-5(c))

The method a) has a simple optics with no optical splitter. However, it has a half mirror in the collection optics. Therefore, a suitable aperture should be needed in front of the detector to prevent a stray light caused by the reflection on the convex mirror in the collection optics. The methods b) and c) have optical splitters, but have no half mirror in the collection optics. Therefore, the each collection optics has a simple structure. In order to determine the best method, we need to carry out development of micro retro-reflector array, R&D of calibration method, etc.

2.5.2 Optics and Ray-trace Analysis

The three methods mentioned in the previous section have different optics from the light source to the entrance of the collection optics, but have same optics from the collection optics to the micro retro-reflector. The important point is to return the incident light on the same position of the incident point precisely and sufficiently after the reflection with the micro retro-reflector. Therefore, the ray-trace analysis was carried out between the end of the micro-lens array, which is inserted in front of the end of the optical fiber, and the micro retro-reflector array for the upper port optics as shown in Fig. 2.5.2-1 by using the ZEMAX. The rays start from the micro-lens array and go through the collection optics. The rays are reflected by the micro retro-reflector array and come back to the incident points through the same optics. Figure 2.5.2-2 shows a

plane view on the micro retro-reflector array used in the ray trace analysis. Spot diagram of returned rays on the image surface (surface of the micro lens array) is shown in Fig. 2.5.2-3. Here, we assumed the rays start from five field points which (x, y) coordinates are (0 mm, 11.25 mm), (0 mm, 5.75 mm), (0 mm, 0 mm), (0 mm, -5.75 mm) and (0 mm, -11.25 mm) for field 1, 2, 3, 4 and 5, respectively. The detailed spot diagrams for the field 1, 2, 3, 4 and 5 are shown in Figs. 2.5.2-4(a), (b), (c), (d) and (e). From these figures, it is confirmed that the rays come back in to the circle with the radius of 10 μm from the starting point.

Figure 2.5.2-5 shows the irradiance of the light source on the micro retro-reflector array. Here, we assumed a square light source with a uniform emissivity (size of 2.0 mm × 0.25 mm: see Fig. 2.5.2-5) is located at the field 3 (0, 0) on the plane of the micro lens array. It is found from this figure that a square 5 mm on a side is sufficient size for the micro retro-reflector array. However, we adopted 10 mm as the array size considering safety factor of 2 and productivity. The irradiance of the reflected light by the micro retro-reflector array on the collection lens is shown in Fig. 2.5.2-6. Almost reflected light comes back into the collection lens if we assume the reflectance is 1(unity) for each mirror. The reflected light does not spread at the collection lens. In the figure, the strange hexagonal pattern appears. In order to confirm that the hexagonal pattern is caused by the plasma facing spherical first mirror in the header optics, the ray trace was carried out by changing the spherical mirror to a plane mirror. Figure 2.5.2-7 shows the irradiance of the light source located at the field 3 (0, 0) on the collection lens with the plane mirror. In the figure, there is no strange pattern. If we use a micro retro-reflector array with much smaller retro-reflector unit, the strange irradiance distribution may be inconspicuous.

Figure 2.5.2-8 shows the irradiance of the returned light on the image surface (surface of the micro lens array). From the figure, it is confirmed that almost all the light emitted from the light source comes back into the same micro lens of the micro-lens array. The displacement of the optical axis is less than few μm as shown in Fig. 2.5.2-4(c). The intensity of the returned light will be discussed in the next section.

From above results, this calibration method has a potential to calibrate the optical sensitivity of the Impurity Influx Monitor (divertor) during the operation phase of ITER.

2.5.3 Estimation of Detected Signal

Detected signal has been estimated for the method b) as a reference. The incident photons on to the entrance slit of the spectrometer N_d [photons/nm/s] is presented as follows;

$$N_d = I_s \cdot \Omega_s \cdot A_s \cdot T_o \cdot T_f \ (2 \times 0.25)/\pi, \qquad\qquad (2.5.3-1)$$

I_s :   Intensity of light source [w/nm/m^2/s/sr],

Ω_s: Solid angle of optics at light source [sr],

A_s: Area of light source [m^2],

T_o :   Transmissitity of optics,

         (Light source − micro retro-reflector array - end of the micro lens),

T_f: Transmissitity of optical fiber,

(2 × 0.25)/π : Area of the micro lens/ Area of circle with a diameter of 2.0 mm.

The geometric aspect around the micro lens is shown in Fig. 2.5.3-1. The light from the optical fiber with NA = 0.2 enters the micro lens and a fraction (0.25 × 2.0)/π of the incident light is emitted from the micro lens to the collection optics.

Signal strength per one pixel of detector S [electrons/pixel/s] is presented as follows;

$$S = N_d \cdot R \cdot T_{sp} \cdot d \cdot L \cdot (A_p/A_d) \cdot Q, \tag{2.5.3-2}$$

R :	NA of spectrometer /NA of optical fiber at the entrance slit (NA: Numerical Aperture), Here, R=1 is assumed,
A_p :	Area of pixel of detector [m^2],
A_d :	Area of the image on the detector [m^2],
T_{sp} :	Transmissity of spectrometer,
d:	Inverse liner dispersion on the entrance slit [nm/mm],
L:	Width of the entrance slit [mm],
Q :	Quantum efficiency of the detector.

Reflectivities of mirror materials and transmissivities of typical optical fibers are shown in Fig. 2.5.3-2 [2-1] and Fig. 2.5.3-3, respectively. Here, we assume that molybdenum (Mo) is used for the plasma facing first mirror and the micro retro-reflector array, and aluminum (Al) is used for other mirrors. The spectrometers for the UV region (200 – 400 nm) are located in the port cell and the spectrometers for the visible region (400 – 1000 nm) are located in the diagnostic room. We assume that optical fibers of 2 m long are used for the UV region and optical fibers of 100 m long are used for the visible region. Lenses and windows made of fused silica (SiO$_2$) are assumed. Transmissivities of optical components for the in-situ calibration optics are shown in Table 2.5.3-1. For calculation, we assume to use a xenon lamp (HAMAMATSU: L7810) for the light source and a back-thinned type CCD (HAMAMATSU) for the detector. Typical optical parameters used in the calculation are summarized in Table 2.5.3-2. The calculated results are shown in Table 2.5.3-2 and Fig. 2.5.3-4. From these table and figure, sufficient signals will be detected by this calibration method.

2.5.4 Concluding Remarks and Issues

In-situ calibration methods for the Impurity Influx Monitor (divertor) have been considered. Detailed study of the in-situ calibration methods by using a light source located outside the vacuum vessel has been carried out. Ray-trace analysis shows that the optics for calibration has a sufficient performance. Sufficient signal to noise ratio will be obtained by the method.

The ray-trace analysis and the estimation of the signal to noise ratio have been carried out by using ideal micro retro-reflector array, beam splitter, detector, spectrometer and optics. The flux of the light coming on to the detector after reflected on the micro retro-reflector array depends on the manufacturing accuracy of the micro retro-reflector array, optics and the optical adjustment such as alignment and focusing. Therefore,

mock-up test will be required to confirm the practical performance and to find out problems to be solved before the detailed design. Moreover, alternative and complementary methods (shown in Table 2.5-1) should be studied.

2.6 Optical Alignment System and Focusing System

Spectroscopic measurement systems in ITER observe plasmas through the optical paths with labyrinths in order to prevent the neutron streaming. And, it is anticipated that the optical components on the optical axis move by heat distortion and electromagnetic force, etc. Therefore, the adjustment mechanism, which always monitors and corrects the displacement of optical axis, becomes necessary.

During the installation phase, optical axis adjustment will be carried out at a room temperature. After that, the vacuum vessel, the blanket and the divertor are baked at the temperature of 200°C ~ 240°C by water for wall conditioning. During the operation, those components are cooled by water (inlet temperature of 100°C and the outlet temperature of 150°C) against the heat load from the plasma [2-2]. Therefore, the optical axis greatly deviates from that in the room temperature by the heat distortion. It is possible to adjust the optical axis against the displacement caused by the heat distortion from the room temperature to the constant expected operating temperature. But, it will be very difficult to predict the displacement caused by the temperature change and the electromagnetic force on the optical components during the plasma discharge. The real time control system for optical alignment will be necessary.

2.6.1 Scheme of Optical Alignment

The prototype optical alignment system had been constructed and the performance had been tested under the ITER EDA task agreement of R&D task (Task agreement number: N 55 TT 05 FJ, Task ID number: T489-JA). In this design task, the optical system of the Impurity Influx Monitor (divertor) has been changed to increase detected signals and to simplify the optics. Here, we describe the optical alignment system for the new optics.

The fundamental concept, which is the same as the previous one, has been applied. The alignment will be carried out by tilting and shifting the mirror mounted in the labyrinth at the biological shield as shown in Fig. 2.6.1-1. Here, following three illumination methods and the displacement detecting methods have been considered.

a) The light is applied on a small diffuser located at the suitable position in the header optics through the same optics for plasma measurements from the outside of the vacuum vessel. The image of the diffuser is focused on a CCD camera by using a dedicated optics. (Fig. 2.6.1-2(a))

b) A dedicated small light source is installed at the suitable position on the optical fiber bundle connected with the collection optics. The image of the light source is focused on the target located in the header optics. The image is observed by a dedicated optics with a CCD camera. (Fig. 2.6.1-2(b))

c) The light is applied on a small diffuser located at the suitable position in the header optics by a light

source located in the vacuum vessel. The image of the diffuser is focused on a CCD camera by using a dedicated optics.

2.6.2 Optics for Optical Alignment System

The design of the collection optics for Impurity Influx Monitor (divertor) has been changed from an off-axis aspherical mirror system to a simple Cassegrain telescope system as shown in Fig. 2.6.2-1. This change enables to install a dedicated optics for alignment in the collection optics without obstructing the aperture for plasma measurements as shown in Fig. 2.6.1-2.

In the method a), the light, such as laser, is introduced into the dedicated optics for alignment and is applied on the target installed in the header optics. A small diffuser is set on the target. The image of the diffuser is focused on the CCD camera as shown in Fig. 2.6.1-2(a). A filter, which transmits the laser light, is inserted in front of the CCD camera to prevent a stray light. The displacement of the optical axis of the plasma measurement system is deduced from the image position of the diffuser on the CCD. In this method, it is important to align the optical axis of the alignment system with that of the plasma measurement system precisely.

In the method b), the light is introduced into the collection optics from a small light source located on the unit of optical fiber bundle as shown in Fig. 2.6.1-2(b). The image is focused on the target in the header optics. The image is observed by the dedicated optics for alignment. The target has a special pattern or a small diffuser to identify the position of the image on the target. The image is observed by the dedicated optics for alignment. The displacement of the optical axis of the plasma measurement system is deduced from the image position on the target. In this method, it is needed to illuminate the target in order to observe the special pattern by the CCD camera.

If it is possible to set a light source in the vacuum vessel to illuminate the diffuser or to set a light source on the target in the header optics as mentioned in the method c), the alignment system becomes simple.

The optical performance of the alignment system has been studied by ray-trace analysis (Fig. 2.6.2-2). Fig. 2.6.2-3 shows a point spread function of the field 1 ($y = 0$ mm) on the CCD. Here, the distance between the field 1 and the lens of the CCD camera is 14040 mm. As a result, sufficient image quality (spot size < 20 μm) will be obtained on the CCD.

2.6.3 Focusing System

The focusing of the optics for Impurity Influx Monitor (divertor) is performed by moving the unit composed of a small spherical mirror, a field lens in the collection optics and an optical fiber bundle attached. The ray-trace analysis has indicated that the image of the micro lens array is focused on the suitable plane in the header optics and spread into the plasma. Therefore, it will be possible to focus the optics by using the alignment method b). If we move the position of the unit, where the image of the light source has a minimum size, the focusing will be carried out.

2.6.4 Concluding Remarks and Issues

Here, the quantitative analysis has not been carried out. Therefore, it is needed to estimate the signal strength on the CCD camera and the S/N ratios for three methods mentioned above. The mock-up test should be carried out. Moreover, alternative and complementary methods should be studied.

2.7 Integration of Measurement, Calibration, Alignment and Focusing Optics

Figure 2.7-1 shows a schematic view of the integrated optical systems for plasma measurements, calibration (Fig. 2.5.1-5(b), alignment (Fig. 2.6.1-2(a), (b)), and focusing. It will be possible to take each measurement without disturbing other optical systems.

2.8 Consideration of Possible Concepts for First Mirror Shutters

The optics of the Impurity Influx Monitor (divertor) is installed in the three ports, i.e. divertor, equatorial and upper ports. In these optics, a shutter is necessary to protect front-end components (first mirror facing a plasma) against sputtering, deposition, erosion, etc. during the plasma termination, plasma disruption, discharge cleaning etc. Requirement for a shutter on ITER is normally open [2-2] even if an electric power or pneumatic power for actuator is down and is closed in abnormal events mentioned above or discharge cleaning.

There are several kinds of shutters (flap, rotary disk, pendulum, iris, rotary valve, etc.), which are driven by electrical or pneumatic actuator, or electromagnetic force ($j \times B_t$ (toroidal field) force) [2-2]. Among these shutters, we propose new concepts of mechanical shutters (flap type and rotary disk type) using an electric actuator for following reasons.

(1) Mechanical shutters are stiff. We can make them using a conventional technology so that we obtain higher reliability.

(2) The shutters that do not use $j \times B_t$ force as an actuator can operate in the glow discharge cleaning without B_t.

(3) We can add another function to the shutter on our proposed ones as described below.

However, there is a few demerits for our proposed shutter mechanism, that is, response of the shutter is slow, so we may not use this shutter against fast events. We need many components of the shutter mechanism and the long route to an actuator mounted on the port plug.

In upper and equatorial ports, an installation space of the shutter is very narrow. So, it is necessary to design compact size shutter. Also, we have designed the shutter having another function for the in-situ calibration in the upper and equatorial ports mentioned at the previous section.

Figure 2.8-1 shows the schematic diagram of the flap type shutter mechanism that is installed near the end top of the upper port plug. The shutter mechanism is mounted on a base plate on which mirror holders are mounted. These are installed in a housing that is mounted in the port plug. Shutter can be closed/opened by using an electric linear actuator with an electromagnetic brake mounted outside a vacuum flange of the port plug (see Fig. 2.8-1(b)). The shutter is flap type and micro retro-reflector array (size: 10 mm ×10 mm) is put

on the shutter surface that faces on the first mirror at the closed position for the in-situ calibration as shown in Fig. 2.8-1(c). The shutter size is ~75 mm in diameter and ~10 mm in thickness with a honeycomb structure to reduce nuclear heating. The normal position of the shutter is the full-open position and it can rotate around the fixed pivot bearing by ~85 degree. The shutter has an arm (shutter-arm, length: ~25 mm) to couple with the connecting bar by flexible pivot bearings as shown in Fig. 2.8-1(c). The flexible pivot bearings are used at each connecting point.

The piston-crank mechanism is used to convert the rectilinear motion of the actuator into rotary motion of the shutter around the pivot. The piston-crank mechanism consists of the crank (shutter arm), connecting bar, piston (slider and cylinder). Two bell crank levers are used to change the direction of the rectilinear motion. One of them is coupled with the connecting bar that is coupled with the piston (slider and cylinder). The cylinders of the piston are supported on the base plate cooled by water.

Replacing piston (slider and cylinder), connecting bar and flexible pivot bearing (free), we introduce another driving mechanism with stranded wires, wire-tension adjuster, wire-support wheel/wire-tension adjuster, bell-crank-lever, etc. as shown in Fig.2.8-1 (d). These parts of the driving mechanism are dual structure to open and close the shutter. The stranded wire becomes loose as increasing temperature due to the thermal expansion. In order to absorb the looseness of the wire, the wire-tension adjuster is introduced in the driving mechanism. The route of the wire can easily be changed and the nuclear heating of the wires may be little compared with the piston (slider and cylinder).

Another shutter mechanism for a rotary disk type shutter is shown in Fig. 2.8-2 (a). The driving mechanism of the rotary disk consists of stranded wires, wire-tension adjuster, wire-support wheel/wire-tension adjuster, etc. It is nearly the same mechanism as one in Fig. 2.8-1(d). Figure 2.8-2(b) is the schematic diagram of the top and side views of the rotary disk shutter and the part of the driving mechanism. The rotary disk shutter is put in front of the first mirror to be vertical to the central line of the viewing fan and rotated around the axis of the fixed pivot bearing (rotating angle between closed position and open position is ~50 degrees). Figure 2.8-2(c) shows the schematic diagram of the wire-winding mechanism, rotary feedthrough and electric stepping motor. The wire-winding mechanism consists of two wheels to wind the wire, two wire-support wheels and worm gear connected to the rotary feedthrough. Two wheels are rotated by the worm gear connecting the feedthrough and stepping motor. When the worm gear rotates in the clock-wise direction, one wheel winds one wire and another wire is un-winded simultaneously, and then the shutter is opened. For the rotation of the worm gear in the counter clock-wise direction, the forward wheel un-winds the wire and backward one winds the wire simultaneously, and the shutter is closed. These types of shutter mechanisms can be also applied to the equatorial port plug.

Figure 2.8-3 shows the conceptual structure of the fixed pivot bearing. This pivot bearing is adopted to keep the precise rotating axis. The shutter arm connects to the shaft of the bearing. Also, the shaft is welded to one side of the spiral spring. Other side of the spring is welded to the inside wall of the bearing housing to prevent the shutter from chattering during the plasma operation and to maintain the normal position of the shutter (full-open position). The sensors (simple mechanical contact switch) in Figs.2.8-1(c) and 1.8-2(b)

monitor open- and close-status of the shutter. Switches connected with two MI-cables supply small voltage between two MI-cables. When the shutter-arm or rotary disk shutter contacts the sensor, the voltage drop is detected.

The pivot bearings, bell-crank-levers, pistons (slider and cylinder), wire-tension adjusters, wire-support wheel/wire-tension adjusters and wheel to change the wire direction must be oil-free to be mounted in the radiation and vacuum environment, and also, the materials of these parts should be selected to have radiation hardness.

The interface with vacuum region is the linear motion feedthrough with flexible double-sealed bellows or rotary feedthrough as shown in Figs.2.8-1(b) and 2.8-2(c). Space between two bellows of linear motion feedthrough is pumped out through the exhaustion connector that is also used to introduce He probe gas to detect leak. Usually, shrinkage stress is act on the double-sealed bellows of the feedthrough because the inside of the bellows is vacuum. The feedthrough is supported at the vacuum flange by using axial guide bearing. The actuator and feedthrough are directly connected and are mounted in the Support/holder put outside the vacuum flange.

The electric linear actuator is used to drive the shutter, which has an electromagnetic brake to softly touch the heat sink at full-open position and damper at closed one to protect the shutter from the impact. The stroke of the actuator is more than 30 mm. Required torque of the actuator must be withstood to torque of the spiral spring of the pivot bearing, shrinkage stress of the feedthrough bellows, weight in the direction of the axis of two sliders, and frictional force of the rotating axis and between slider and cylinder.

Most of parts of the shutter mechanism are put in radiation environment, therefore nuclear heating issue is very important. It is necessary to remove the heat from parts of the shutter mechanism. The base plate is cooled by water, so the cylinder supported on the base plate, fixed pivot bearings, dual wire-tension adjusters, wire-support wheel/wire-tension adjusters, etc. are cooled by heat conduction. Also, in order to cool the shutter/crank lever and bell crank lever, heat sinks cooled by water are put on the base plate in order to adhere shutter and bell crank lever. However, cooling of the flexible pivot bearings and sliders is difficult.

The following R&D is necessary for a realization of the shutter.

(1) Development of the fixed and flexible pivot bearings to be able to use vacuum and radiation environments.

(2) Development of the linear motion feedthrough with flexible double-sealed bellow and oil-free axial guide bearing, and rotary feedthrough with oil-free.

(3) Development of wire-winding mechanism and dual wire-tension adjuster to be able to use in vacuum and radiation environments.

3. Investigation of Optical Detector

3.1 Objectives

Conceptual design of a two-dimensional (2-D) optical detector had been performed by the Japan Home Team during the EDA phase. There were no detectors satisfying the requirements for detection area and the time resolution in that time. The methods of detector control and data acquisition have been not yet considered for application to discharges beyond 600 s in ITER until now. In this work, a fast 2-D detector for the spectrometer using optical filters and a 2-D detector for the spectrometer with a low and a high dispersion are designed. Data acquisition and control systems are also designed.

3.2 Required Performance

The requirement for the time resolution for the Impurity Influx Monitor (divertor) is shown in Table 1-1 [3-1 ~ 6]. The outlines of the spectrometers, whose optical design was carried out in the EDA phase, are shown in Figs.3.2-1 ~ 4 and specifications of each spectrometer are shown in Table 3.2-1 [3-6]. In the recent design of the spectrometers, two types of the detector are needed. One is a detector to measure the detailed time evolution of the intensity of the selected spectral lines emitted from various divertor positions simultaneously with filter spectrometer (FS). The other one is to measure the spectral lines in a wide wavelength range emitted from the selected position of the divertor region with the visible survey spectrometer (VSS) and the high dispersion spectrometer (HDS).

3.3 Basic Performance

The design work for the detector is carried out by using current commercial-based multi-channel detectors, data acquisition modules, PC and LAN.

3.3.1 Detector for Filter Spectroscopy (FS)

In the recent optical design of FS, an image of the 18×18 optical fiber array is focused on the detector. In order to measure intensities of the each optical fiber simultaneously, 2-D PIN diode array detector is selected in this design. Figure 3.3.1-1 shows the details of the active area of Hamamatsu C4675-103 detector. Table 3.3.1-1 shows specifications of this detector. The advantage to use such a 2-D detector is the simultaneity of the each element because the current-voltage conversion amplifiers are connected to each element of photodiode array individually, thereby high-speed parallel signal processing is allowed. The block diagram of this detector is shown in Fig. 3.3.1-2. When light enters a photodiode, photoelectric conversion occurs in the photodiode and the photocurrent I_p is generated. The photocurrent then flows thorough the current-to-voltage conversion amplifier feedback resistance R_f and is output as voltage $V (= I_p \times R_f)$. The C4675 series use current-to-voltage conversion amplifiers connected to each of the 256-element photodiodes to perform parallel signal processing. A low noise bias circuit is used to reduce the photodiode junction capacitance. As a result, flat output response is obtained at frequency up to 10 kHz (C4675-103), which satisfies the required time resolution of 1 ms. Figure 3.3.1-3 shows the photosensitivity of C4675.

Photosensitivity in the short wavelength region (less than 400 nm) depends on the window material (flat glass). Therefore, the photosensitivity in the short wavelength region can be increased easily by changing the window material to the quartz. Figure 3.3.1-4 shows the dimensional outline of the C4675 detector. The size of this detector is acceptable for the recent design of FS.

Unfortunately, Hamamatsu S4529 used as a sensor of the C4675 detector will be stopped to product in a near future. But new photodiode array (S3805) can be replaced as a sensor of C4675. Photosensitivity of S3805 shown in Fig. 3.3.1-5 is almost same as that of S4529. Figure 3.3.1-6 shows the details of the active area and Table 3.3.1-2 shows the specifications. This array has a large active area compared with S4529. The optical and electric characteristics of S3805 satisfy the required characteristics.

In the recent design of FS, the magnification of the spectrometer is unity, each fiber is arranged 0.3 mm pitch, which is too narrow to be fit the each optical fiber to the each detector element (show Fig.3.3.1-6). If each fiber was arranged 1.5 mm pitch, image of optical fiber corresponds with the detector element but the spectrometer became larger compared with recent design. If the magnification of spectrometer changes from unity (recent design) to 5, image of optical fiber corresponds with the detector element as shown in Fig. 3.3.1-7and only small change of spectrometer (design of the camera) must be needed.

In order to adjust the signal level to the data acquisition system, the pre-amplifier system is necessary. Table 3.3.1-3 shows specifications of a low noise DC amplifier module, NF Circuit CA206L2. The gain of this amplifier can be controlled by the external signal. So, the signal level of each channel can be adjustable individually. It also realizes high density mounting by using a single-in-line package.

3.3.2 Detector for Visible Survey Spectrometer (VSS) and High Dispersion Spectrometer (HDS)

In the recent design of VSS and HDS, 12 optical fibers were arranged in front of the entrance slit. The light is dispersed by the grating and focused on the detector. In order to get higher quantum efficiency, an electron multiplying CCD (EMCCD) with faster readout time and a large active area is selected for both spectrometers.

The quantum efficiency of the EMCCD (ANDOR DU741N) is shown in Fig. 3.3.2-1 and specifications are shown in Table 3.3.2-1. Unlike a conventional CCD, the sensitivity of the EMCCD is not limited by the readout noise of the output amplifier even when operated at high readout speeds because it enables charge from each pixel to be multiplied on the sensor before readout. This is achieved by adding a solid state Electron Multiplying (EM) register. As the EM register has several hundred stages that use higher voltages than normal clock, charge is transferred through each stage with the phenomenon of impact ionization, which is utilized to produce secondary electrons and then charge is multiplied. When this is done over the several hundred stages, the resultant gain can be controlled from unity to hundreds or even thousands of times with a very low noise factor.

In order to reduce the crosstalk between each channel, each optical fiber (core/cladding = 0.2/0.25 mm) is arranged with 0.3 mm pitch (total 3.55 mm). Because magnification of spectrometer is 1.83 in the recent design of VSS, the image height on the detector becomes 6.50 mm, which is larger than the active area of the

detector. If the magnification of spectrometer is changed to 1.76, the image height becomes 6.248 mm and the pitch of each optical fiber corresponds with 33 pixels of the detector as shown in Fig. 3.3.2-2. The inversed linear dispersion on the detector is changed from 2.134 to 2.052 as changing the magnification of the spectrometer. Therefore, the dispersion corresponding to a 2-pixel width of the detector is changed from 0.102 nm to 0.066 nm due to reduced pixel size from 24 μm to 16 μm. For the same reason the magnification of relay optics of HDS must be changed from 3.7 (the recent design) to 1.76. The magnification of the spectrometer is unity in the previous design. So the dispersion of HDS is not changed, but the reduction of the pixel size increases a resolving power of HDS.

The readout time is estimated from Table 3.3.2-2.

$$T = 1600 \text{ (pixel/scan)}/3 \times 10^6 \text{ (s/pixel)} \times 12 \text{ (scan)} + 4.9 \text{ (μs/pixel)} \times 400 \text{ (pixel)}$$
$$= 8.36 \text{ ms}$$

This value is enough for the requirement of both VSS and HDS.

The dimensional outline of DU741N is shown in Fig. 3.3.2-3. The size is adequate to the present design of HDS and VSS.

3.3.3 Operation under Strong Magnetic Field

It is wonder that the magnetic field affects the operation of the CCD detector. The CCD detector used in the high magnetic field is investigated. Figure 3.3.3-1 shows the experimental arrangement of the *in situ* observations of the orientation of the growing amino-acid crystals in the magnetic field [3-7]. In this system, a CCD camera is mounted on the bore of the superconducting magnetic coil. The strength of magnetic field excited by the superconducting magnet is up to 5 T and the images were recorded using the CCD camera and a VTR system. There is no trouble on the CCD detector. The Of course, the CCD camera used in this system is not the same as that for HDS and VSS, but this result indicates that the magnetic filed affects only small effect on the CCD detector.

3.4 Scheme of Control System for Detector

C4675 detector is designed to suppress the power consumption and it can be operated with two DC power supplies (±15V). Therefore, it can be controlled by the turn-on/off of the power supplies, which is easy to be realized by using a conventional mechanical switch controlled by PC. A gain of the preamplifier of each channel can be also controllable by the software individually.

Operational conditions of the DU741 detector (pixel readout rate, vertical clock speed, electron multiplier gain, detector temperature, data acquisition, the data storage and so on) can be changed by the software via the standard USB port. The PC-based package software for DU741 is already prepared. It can be built for own application from the ground up and integrated custom-designed experiment via C, C++, Visual Basic, LabVIEW or Delphi to name just some of the possible implementation languages.

3.5 Scheme of Data Acquisition System for Detector

For the C4675 detector 256-channel ADC is necessary. By using simultaneous-sampling module (mainly less than 8 channels/module) with higher accuracy (> 16 bit) and higher sampling time (> 10 ksample/s), more than 32 modules are needed. Therefore, multifunction data acquisition system such as NI PXI-6259 is selected to reduce the space. It has an onboard amplifier designed for fast settling time at high scanning rates, ensuring 16-bit accuracy even when measuring with all channels at maximum speeds. Figure 3.5-1 shows the electrical connection of data acquisition system. Eight modules are mounted on one standard PXI rack and connected to the PC-PCI bus. This module can be controlled from the PC by using LabVIEW software. The synchronized operation of multiple devices is confirmed by using the PXI trigger bus. The setting time for the multi-channel measurement determines the accuracy and the time interval of each channel. This value depends on the input signal range as shown in the Table. 3.5-1. When the signal range is larger than ±0.5 V, setting time is less than 2 μs and all of 32 channels of the each module can be measured within 62 μs. That is, all of the 256 channel data from the detector can be measure within 62 μs. The data is transferred to the storage device via PCI data bus and send to the data acquisition system of ITER (CODAC) via LAN every 1 ms. The transfer rate and the total amount of data are estimated in the type of 10^4 sample/s (10 times over sampling for the requirement) shown in Fig.3.5-2.

Transfer rate = 256 (channel) × 2 (B/channel/sample) × 10^4 (sample/s) = 5.12 MB/s

Total amount of data = 5.12 MB/s × 1000 s = 5.12 GB

These values are acceptable for the present PCI data bus (133 MB/s) and the storage device such as HD and DVD mounted on the local PC. The transfer rate and total amount of data to CODAC from all of 24 detectors is estimated.

Transfer rate = 0.512 MB/s/detector × 24 detector = 12.288 MB/s

Total amount of data = 12.288 MB/s × 1000 s = 12.288 GB

These values are acceptable for present LAN based on the Gbit Ethernet (125 MB/s) and large storage device such as RAID.

Data acquisition system of DU741N is included in the detector control program. Figure 3.5-3 shows the electrical connection of the detector and local data acquisition system. The data transfer rate and total amount of data are estimated for the 10 ms/scan as shown in Fig. 3.5-4.

Transfer rate = 2 (B/channel/scan) × 1600 (channels/point) × 12 (point) × 100 (scan/s)

    = 3.84 MB/s

Total amount of data = 3.84 MB/s × 1000 s = 3.84 GB

These values are acceptable for present USB 2.0 bus data transfer rate (60 MB/s) and the storage device. In the previous design, 32 spectrometers are used in VSS and 2 spectrometers are used in HDS. From this design, the transfer rate and total amount of data to CODAC is estimated.

Transfer rate = 3.84 MB/s/spectrometer × 34 spectrometer = 130.56 MB/s

Total amount of data = 3.84 GB/spectrometer × 34 spectrometer = 130.56 GB

The data transfer rate is larger than the transfer rate of the LAN based on the Gbit Ethernet and total

amount of data is too large to use the real time feedback control in the present data acquisition system. It is more realistic that only selected data for using the feedback control is sent to CODAC at real time and other data are transferred after the discharge is turned-off.

3.6 Summary

The detector for the Impurity Influx Monitor Spectroscopy is designed in accordance with the requirements of ITER.

Main results are as follows:

1) Detector system should be composed of two kinds of the detector such as photodiode arrays for FS and CCD detectors for VSS and HDS.

2) Requirements can be satisfied by using proposed detectors

3) The local control and data acquisition system can be realized by using present commercial-based data acquisition modules, PC, data storage devices and LAN.

3.7 Future Work

Necessary future works are summarized here.

1) Optical design

- Detailed optical design of spectrometer including the detector

- Mechanical design of spectrometer

2) Search and selection of detector

- Faster readout CCD detectors to reduce the time difference between the measured spectral lines

- New techniques to get higher quantum efficiency in the UV and NIR wavelength range

- New techniques of the 2-D detector with parallel processing

3) Development of data acquisition system

- Reconsideration of concept of data acquisition according to the data acquisition devices in future

- Development of software for the detector control and the data acquisition in local system

- Interface with CODAC

- Detailed design

4. Conclusion

The design work of impurity Influx Monitor (divertor) was carried out for new ITER design and following results are obtained.

(1) The analysis indicates that the spatial resolutions performed by the central optics through mirrors in the divertor cassette, the side optics through the gap between the divertor cassettes, the equatorial port optics and the upper port optics will be ≤ 10 mm, ≤ 35 mm, ≤ 48 mm and ≤ 37 mm, respectively.

(2) From these results, the optics designed here will meet the ITER requirement for parameter ranges and for

spatial resolutions.

(3) Detailed study of the in-situ calibration methods by using a light source located outside the vacuum vessel has been carried out. Ray-trace analysis shows that the optics for calibration has a sufficient performance. Sufficient signal to noise ratio will be obtained by the method

(4) Design work of optical alignment system and the focusing system were carried out. As a result, sufficient image quality will be obtained for the alignment system.

(5) Conceptual design of the mechanical shutter was carried out and necessary R&D was listed.

(6) Detector system should be composed of two kinds of the detector such as photodiode arrays for FS and CCD detectors for VSS and HDS and requirements can be satisfied by using proposed detectors.

(7) The local control and data acquisition system can be realized by using present commercial-based data acquisition modules, PC, data storage devices and LAN.

Acknowledgement

References

[1-1] A. E. Costley, K. Ebisawa, P. Edmond, et al., "Overview of the ITER diagnostic system", in Proceedings of the International Workshop on "Diagnostics for Experimental Fusion Reactors" (1997).

[1-2] International Tokamak Activity Web page on Diagnostics; Measurement requirement for ITER, http://www.rijnh.nl/ITPA/.

[1-3] T. Sugie, A. Costley, A. Malaquias, W. Walker, "Spectroscopic Diagnostics for ITER", Journal of Plasma and Fusion Reserch, Vol. 79, No. 10, 1051 (2003).

[1-4] K. Ebisawa, "Divertor impurity monitoring system", in:ITER Design Description Document, (1998).

[1-5] T. Sugie, H. Ogawa, A. Katsunuma, et al., "Divertor impurity monitoring system", Final report for the design task D 323-J1,TA No: S 91 TD 31 95-08-04, (1998).

[1-6] T. Sugie, H. Ogawa, A. Katsunuma, et al., "Design of divertor impurity monitoring system for ITER (II)", JAERI-Tech 98-047 (1998).

[1-7] T. Sugie, H. Ogawa, T. Nishitani, et al., "Divertor impurity monitor for the International Thermonuclear Experimental Reactor", Rev. Sci. Instrum. 70, (1999) 351.

[1-8] T. Sugie, A. Costley, A. Malaquias, et al., "Spectroscopic Measurement System for ITER Divertor Plasma", Proc. 30th EPS Conf. on Contr. Fusion and Plasma Phys., 27A, P-4.63 (CD-ROM) (2003).

[2-1] H. Weaver and H. P. R. Frederikse, "Optical properties of metals and semiconductors", in: *CRC Handbook of Chemistry and Physics*, D. R. Lide, ed., CRC Press, Boca Raton (1994).

[2-2] C. I. Walker, "ITER Diagnostic Shutter System Practice" ITER-D-2224D7 (2004).

[3-1] A. E. Costley, K. Ebisawa, P. Edmond, et al., "Overview of the ITER diagnostic system", in Proceedings of the International Workshop on "Diagnostics for Experimental Fusion Reactors" (1997).

[3-2] International Tokamak Activity Web page on Diagnostics; Measurement requirement for ITER, http://www.rijnh.nl/ITPA/.

[3-3] A. E. Costley, et al., in *Diagnostics for Experimental Thermonuclear Fusion Reactors (Plenum Press, New York, 1998)* 41.

[3-4] V. S. Mukhovatov, et al., in *Diagnostics for Experimental Thermonuclear Fusion Reactors (Plenum Press, New York, 1998)* 25.

[3-5] K. Ebisawa, Divertor Impurity Monitoring System, in *ITER Design Description Document*, (1998).

[3-6] T. Sugie, et al., "Design of divertor impurity monitoring system for ITER (II)", JAERI-Tech 98-047 (1998).

[3-7] K. Ogawa, et al., J. Chem. Eng. Jp. 35 (2002) 1123.

Table 1-1 Requirements for Impurity Influx Monitor (divertor)

• Impurity Species Monitor

Parameter	Parameter range	Spacial Res.	Time Res.	Accuracy
Be influx	4×10^{16}-2×10^{19}	Integral	10 ms	10 % (rel.)
C influx	4×10^{16}-2×10^{19}	Integral	10 ms	10 % (rel.)
Cu influx	4×10^{15}-2×10^{18}	Integral	10 ms	10 % (rel.)
W influx	4×10^{14}-2×10^{17}	Integral	10 ms	10 % (rel.)
Ne, Ar, Kr influx	4×10^{16}-8×10^{18}	Integral	10 ms	10 % (rel.)

• Key Divertor Parameter

Parameter	Parameter range	Spatial res.	Time res.	Accuracy
"Ionization front" position	TBD	~ 100 mm	1 ms	-

• Impurity and D, T Influx in Divertor

Parameter	Parameter range	Spatial res.	Time res.	Accuracy
$\Gamma_{Be}, \Gamma_{C}, \Gamma_{W}$	10^{17} - 10^{22} at/s	50 mm	1 ms	30 %
$\Gamma_{D} \Gamma_{T}$	10^{19} - 10^{25} at/sec	50 mm	1 ms	30 %

• Divertor Helium Density

Parameter	Parameter range	Spatial res.	Time res.	Accuracy
N_{He}	10^{17} - 10^{21} m^{-3}	-	1 ms	20 %

• n_T/n_D, n_H/n_D in Divertor

Parameter	Parameter range	Spatial res.	Time res.	Accuracy
n_T/n_D	0.1 – 10	Integral	100 ms	20 %
n_H/n_D	0.01 - 0.1	Integral	100 ms	20 %

• Ion Temperature in Divertor

Parameter	Parameter range	Spatial res.	Time res.	Accuracy
T_i	0.3-200 eV	50 mm (along legs) 3 mm (across legs)	1 ms	20 %

Table 2.1-1 Optical parameters for collection optics.

Focal length	2856.7 mm
Magnification	1/5
Diameter of incidence pupil	100 mm
NA at micro lens	0.0196
Solid angle without secondary mirror obscuration	9.98×10^{-4} sr
Solid angle of the obscuration by secondary mirror and support structure	1.514×10^{-4} sr
Effective solid angle of collection optics	8.465×10^{-4} sr
Area of micro lens	$2.0 \times 0.25 = 0.5$ mm^2

Table 2.2.2-1 Estimated spatial resolution for the three lines of sight of F1, F3 and F5 of each viewing fan.

Viewing fan	Line of sight		Spatial resolution (mm)
i) Central optics (through mirrors in the divertor cassette)	IV	F1	9.0
		F2	8.4
		F3	7.7
		F4	7.4
		F5	7.1
	OV	F1	7.7
		F2	7.1
		F3	7.1
		F4	7.1
		F5	7.1
	IH	F1	9.7
		F2	9.0
		F3	8.4
		F4	7.7
		F5	7.7
	OH	F1	6.8
		F2	6.5
		F3	5.8
		F4	5.8
		F5	5.2
ii) Side optics (through gap between divertor cassettes)		F1	33
		F2	27
		F3	25
		F4	22
		F5	22
iii) From equatorial port		F1	46
		F2	45
		F3	48
		F4	44
		F5	46
iv) From upper port		F1	36
		F2	35
		F3	36
		F4	35
		F5	35

Table 2.2.2-2 Summary of the trasmissivity T_{pe} of the penetration optics for central optics

IV, OV Optics

wave length nm	200	300	400	500	600	700	800	900	1000
Mo	0.65	0.60	0.55	0.59	0.57	0.57	0.55	0.60	0.81
3 Mo mirrors	0.27	0.22	0.17	0.21	0.19	0.19	0.17	0.22	0.53
Al	0.93	0.93	0.92	0.92	0.92	0.9	0.87	0.89	0.94
5 Al mirrors	0.70	0.70	0.66	0.66	0.66	0.59	0.50	0.56	0.73
SiO2	0.96	0.96	0.96	0.97	0.97	0.97	0.97	0.97	0.97
10 SiO2 surfaces	0.66	0.66	0.66	0.74	0.74	0.74	0.74	0.74	0.74
Total	0.13	0.10	0.07	0.10	0.09	0.08	0.06	0.09	0.29

IH,OH Optics

wave length nm	200	300	400	500	600	700	800	900	1000
Mo	0.65	0.60	0.55	0.59	0.57	0.57	0.55	0.60	0.81
2 Mo mirrors	0.42	0.36	0.30	0.35	0.32	0.32	0.30	0.36	0.66
Al	0.93	0.93	0.92	0.92	0.92	0.9	0.87	0.89	0.94
5 Al mirrors	0.70	0.70	0.66	0.66	0.66	0.59	0.50	0.56	0.73
SiO2	0.96	0.96	0.96	0.97	0.97	0.97	0.97	0.97	0.97
10 SiO2 surfaces	0.66	0.66	0.66	0.74	0.74	0.74	0.74	0.74	0.74
Total	0.20	0.17	0.13	0.17	0.16	0.14	0.11	0.15	0.36

Table 2.2.3-1 Summary of the trasmissivity T_{pe} of the penetration optics for side optics.

wave length nm	200	300	400	500	600	700	800	900	1000
Mo	0.65	0.60	0.55	0.59	0.57	0.57	0.55	0.60	0.81
1 Mo mirrors	0.65	0.60	0.55	0.59	0.57	0.57	0.55	0.60	0.81
Al	0.93	0.93	0.92	0.92	0.92	0.9	0.87	0.89	0.94
7 Al mirrors	0.60	0.60	0.56	0.56	0.56	0.48	0.38	0.44	0.65
SiO2	0.96	0.96	0.96	0.97	0.97	0.97	0.97	0.97	0.97
10 SiO2 surfaces	0.66	0.66	0.66	0.74	0.74	0.74	0.74	0.74	0.74
Total	0.26	0.24	0.20	0.24	0.23	0.20	0.15	0.20	0.39

Table 2.3.2-1 Summary of the trasmissivity T_{pe} of the penetration optics for equatorial port optics.

wave length nm	200	300	400	500	600	700	800	900	1000
Mo	0.65	0.60	0.55	0.59	0.57	0.57	0.55	0.60	0.81
1 Mo mirrors	0.65	0.60	0.55	0.59	0.57	0.57	0.55	0.60	0.81
Al	0.93	0.93	0.92	0.92	0.92	0.9	0.87	0.89	0.94
8 Al mirrors	0.56	0.56	0.51	0.51	0.51	0.43	0.33	0.39	0.61
SiO2	0.96	0.96	0.96	0.97	0.97	0.97	0.97	0.97	0.97
10 SiO2 surfaces	0.66	0.66	0.66	0.74	0.74	0.74	0.74	0.74	0.74
Total	0.24	0.22	0.19	0.22	0.22	0.18	0.13	0.17	0.36

C´. 2.3.3-1 Summary of the trasmissivity T_{pe} of the penetration optics for upper port optics.

wave length nm	200	300	400	500	600	700	800	900	1000
Mo	0.65	0.60	0.55	0.59	0.57	0.57	0.55	0.60	0.81
1 Mo mirrors	0.65	0.60	0.55	0.59	0.57	0.57	0.55	0.60	0.81
Al	0.93	0.93	0.92	0.92	0.92	0.9	0.87	0.89	0.94
5 Al mirrors	0.70	0.70	0.66	0.66	0.66	0.59	0.50	0.56	0.73
SiO2	0.96	0.96	0.96	0.97	0.97	0.97	0.97	0.97	0.97
10 SiO2 surfaces	0.66	0.66	0.66	0.74	0.74	0.74	0.74	0.74	0.74
Total	0.30	0.28	0.24	0.29	0.28	0.25	0.20	0.25	0.44

Table 2.4-1 Calculated solid angle Ω_m for each viewing fan.

Viewng fan	Solid Angle on the Micro Lens Ω_m (sr)	× sectional area of the Micro Lens * $\Omega_m \cdot S_m$ (sr·m²)	Magnification Image on micro lens/Object
i) Central optics (through mirrors in the divertor cassette)	8.465E-4	4.233E-10	1/5
ii) Side optics (through gap between divertor cassettes)	8.465E-4	(4.233E-10)	1/5
iii) From equatorial port	8.465E-4	4.233E-10	1/5
iv) From upper port	8.465E-4	4.233E-10	1/5

Note: * Sectional area of the Micro Lens S_f is 4.0E-7 m².

Table 2.4-2 $T_{pe} \cdot \Omega_m \cdot S_m$ for evaluation of optical performance.

Viewing fan	× sectional area of the Micro Lens* $\Omega_m \cdot S_m$ (sr·m²)	Transmissivity of penetration optics T_{pe} (at 300 nm)	$T_{pe} \cdot \Omega_m \cdot S_m$ (sr·m²) (at 300 nm)
i) Central optics (through mirrors in the divertor cassette)	4.233E-10	0.10 (for IV, OV) 0.17 (for IH, OH)	4.233E -11 7.196 E-11
ii) Side optics (through gap between divertor cassettes)	(4.233E-10)	0.24	(1.016E-10)
iii) From equatorial port	4.233E-10	0.22	9.931 E-11
iv) From upper port	4.233E-10	0.28	1.185 E-10

Table 2.5-1 Candidate in-situ sensitivity calibration methods

Light source	Method	Problems, Issues
Standard light source	Put the light source in the vacuum chamber	Developing the light source that can withstand neutron/gamma/particle radiation
	Introduce the light source by remote handling system (during the maintenance phase)	Long intervals; developing the light source that can withstand gamma radiation; interface with the remote handling system
	Introduce the light from the outside of the vacuum chamber	Not all of system is included in calibration.
Emission from plasma	Branching ratio of spectral lines	Relative calibration vs wavelength; need absolute calibration vs at least single wavelength point
	Use neutral beam emission	Limited wavelength points. Beam viewing is needed
	Use Z_{eff} derived by CXRS	Difficult for systems viewing divertor region.
	Use bremsstrahlung emission	Precise plasma parameter measurements are needed.
	Standard plasma operation for calibration	Sufficient experience in ITER is necessary.

Table 2.5.3-1 Transmissivity of optical components for in-situ calibration system of upper port.

Upper optics (Method (b))				Reflectivity/Transmissivity						
			Material	200 nm	250 nm	300 nm	400 nm	600 nm	800 nm	1000 nm
Splitter Optics	1	Lens	Fused Silica	0.960	0.960	0.960	0.960	0.970	0.970	0.970
	2	Half mirror	Al+Fused Silica	0.460	0.462	0.463	0.462	0.460	0.435	0.476
	3	Lens	Fused Silica	0.960	0.960	0.960	0.960	0.970	0.970	0.970
Collection Optics	4	micro lens +Field lens	Fused Silica	0.960	0.960	0.960	0.960	0.970	0.970	0.970
	5		Al	0.926	0.924	0.925	0.924	0.920	0.870	0.952
	6		Al	0.926	0.924	0.925	0.924	0.920	0.870	0.952
	7		Fused Silica	0.960	0.960	0.960	0.960	0.970	0.970	0.970
Labyrinth	8		Al	0.926	0.924	0.925	0.924	0.920	0.870	0.952
	9		Al	0.926	0.924	0.925	0.924	0.920	0.870	0.952
Window	10		Fused Silica	0.960	0.960	0.960	0.960	0.970	0.970	0.970
	11		Fused Silica	0.960	0.960	0.960	0.960	0.970	0.970	0.970
Port plug and Header	12		Al	0.926	0.924	0.925	0.924	0.920	0.870	0.952
	13		Mo	0.660	0.690	0.590	0.544	0.565	0.560	0.640
Micro Retro-reflector	14		Mo	0.660	0.690	0.590	0.544	0.565	0.560	0.640
	15		Mo	0.660	0.690	0.590	0.544	0.565	0.560	0.640
	16		Mo	0.660	0.690	0.590	0.544	0.565	0.560	0.640
Port Plug and Header	17		Mo	0.660	0.690	0.590	0.544	0.565	0.560	0.640
	18		Al	0.926	0.924	0.925	0.924	0.920	0.870	0.952
Window	19		Fused Silica	0.960	0.960	0.960	0.960	0.970	0.970	0.970
	20		Fused Silica	0.960	0.960	0.960	0.960	0.970	0.970	0.970
Labyrinth	21		Al	0.926	0.924	0.925	0.924	0.920	0.870	0.952
	22		Al	0.926	0.924	0.925	0.924	0.920	0.870	0.952
Collection Optics	23		Fused Silica	0.960	0.960	0.960	0.960	0.970	0.970	0.970
	24		Al	0.926	0.924	0.925	0.924	0.920	0.870	0.952
	25		Al	0.926	0.924	0.925	0.924	0.920	0.870	0.952
	26	micro lens +Field lens	Fused Silica	0.960	0.960	0.960	0.960	0.970	0.970	0.970
Splitter Optics	27	Lens	Fused Silica	0.960	0.960	0.960	0.960	0.970	0.970	0.970
	28	Half mirror	Al+Fused Silica	0.460	0.462	0.463	0.462	0.460	0.435	0.476
	29	Lens	Fused Silica	0.960	0.960	0.960	0.960	0.970	0.970	0.970
Sub Total				0.0178	0.0218	0.0101	0.0066	0.0085	0.0044	0.0230

				(2 m)	(2 m)	(2 m)	(2 m)	(100m)	(100m)	(100m)
Optical fiber	1			0.65	0.87	0.94	0.98	0.74	0.84	0.87
	2			0.65	0.87	0.94	0.98	0.74	0.84	0.87
Spectrometer										
Collimator	3			0.85	0.85	0.85	0.85	0.85	0.85	0.85
Grating	4			0.50	0.50	0.50	0.60	0.60	0.60	0.60
Camera	5			0.85	0.85	0.85	0.85	0.85	0.85	0.85
Sub Total				0.153	0.273	0.319	0.416	0.237	0.306	0.328

Table 2.5.3-2 Light source, detector, typical optical parameters used in the calculation, and calculated results.

Item		Unit	200nm	250nm	300nm	400nm	600nm	800nm	1000nm
Light source L7810 (HAMAMATSU)	Irradiance (at 50 cm)	mW/cm² /nm	0.1	0.28	0.6	1.1	1.2	1.2	1.2
1 mm dia. light assumed	Radiance: I_s	mW/cm² /nm/sr	3.185E+04	8.918E+04	1.911E+05	3.504E+05	3.822E+05	3.822E+05	3.822E+05
Aperture (dia:0.2 mm)	Area: A_s	cm²	3.140E-04	3.140E-04	3.140E-04	3.140E-04	3.140E-04	3.140E-04	3.140E-04
Solid angle (at light source): Ω_s		sr	1.256E-01	1.256E-01	1.256E-01	1.256E-01	1.256E-01	1.256E-01	1.256E-01
Loss of micro lens			0.16	0.16	0.16	0.16	0.16	0.16	0.16
Strength of Incident light to the optics (Ignore Transmission)		mW/nm	2.010E-01	5.627E-01	1.206E+00	2.211E+00	2.412E+00	2.412E+00	2.412E+00
Strength on the entrance slit (In the circle of 0.2 mm dia)		mW/nm	3.568E-03	1.226E-02	1.216E-02	1.468E-02	2.046E-02	1.058E-02	5.558E-02
Strength on the detector (In the circle of 0.2 mm dia)		mW/nm	5.45E-04	3.35E-03	3.88E-03	6.11E-03	4.86E-03	3.24E-03	1.82E-02
		W/nm	5.45E-10	3.35E-09	3.88E-09	6.11E-09	4.86E-09	3.24E-09	1.82E-08
		J/s/nm	5.45E-10	3.35E-09	3.88E-09	6.11E-09	4.86E-09	3.24E-09	1.82E-08
Photon Energy		J	9.93E-19	7.94E-19	6.62E-19	4.97E-19	3.31E-19	2.48E-19	1.99E-19
Inverse dispersion: d (VSS Spectrometer)		nm/mm	2.1	2.1	2.2	2.1	2.1	2.2	2.1
Photons on the detector (In the circle of 0.2 mm dia)		photons/s /nm	2.30E+08	1.77E+09	2.58E+09	5.17E+09	6.16E+09	5.74E+09	3.86E+10
Photons on the detector pixel (24µm×24µm)		photons/s /nm	4.22E+06	3.24E+07	4.72E+07	9.46E+07	1.13E+08	1.05E+08	7.06E+08
Quantum efficiency of detector : Q Back illumination CCD (Hamamatsu)			0.65	0.73	0.47	0.6	0.92	0.82	0.23
Signal of detector		e-/pixel/s	2.74E+06	2.37E+07	2.22E+07	5.68E+07	1.04E+08	8.61E+07	1.62E+08
Dark count of detector	(0 ℃)	e-/pixel/s	200	200	200	200	200	200	200
	(25 ℃)	e-/pixel/s	4000	4000	4000	4000	4000	4000	4000
Output		1.2 mV/e-							
Output signal		mV	3.29E+06	2.84E+07	2.66E+07	6.81E+07	1.25E+08	1.03E+08	1.95E+08
Dark	(0 ℃)	mV	240	240	240	240	240	240	240
	(25 ℃)	mV	4800	4800	4800	4800	4800	4800	4800
S/N	(0 ℃)		1.37E+04	1.18E+05	1.11E+05	2.84E+05	5.19E+05	4.31E+05	8.12E+05
	(25 °C)		6.85E+02	5.92E+03	5.55E+03	1.42E+04	2.59E+04	2.15E+04	4.06E+04

Table 3.2-1 Functions and outline specifications of proposed spectrometers

· Visible survey spectrometer

Parameters to be measured	Impurity species, Impurity and D/T influx
Wavelength range	200 nm - 1000 nm (simultaneously)
Wavelength resolution	~0.1 nm
Time resolution	10 ms
Spatial resolution	~12 sight lines for divertor legs

· Filter spectrometer

Parameters to be measured	2-dimensional impurity and D/T influx, Ionization front, Helium density (n_e, T_e)
Wavelength range	200 nm - 1000 nm (~12 lines)
Wavelength resolution	~1 nm
Time resolution	1 ms
Spatial resolution	~50 mm

· High dispersion spectrometer

Parameters to be measured	n_T/n_D and n_H/n_D ratio, Ion temperature, Particle Energy Distribution
Wavelength range	200 nm - 1000 nm
Wavelength resolution	<0.01 nm
Time resolution	10 ms
Spatial resolution	~12 sight lines for divertor legs

Table 3.3.1-1 Specifications of Multi-channel Pin-Diode array detector (Hamamatsu C4675)

General Rating

Parameters	Rating	Unit
Photodiode	Si PIN photodiode array (Made by Hamamatsu S4529)	-
Number of element	16 x 16 (256)	-
Active area (per 1 element)	0.95 x 0.95	mm
Element pitch	1.1	mm
Output type	Current-voltage conversion method, 256-ch parallel analog voltage output	-
Dimensional outline	136 (W) x 136(H) x 153.5(D)	mm
Weight	2.1	kg

Absolute maximum ratings

Parameters	Symbol	Value	Unit
Operating temperature	T_{opr}	0 to +50	°C
Strage temperature	T_{stg}	-21 to +50 (no condensation)	°C
Supply voltage	V_S	18	V

Electrical and optical characteristics (Typ. T_a=25 °C)

Parameters	Symbol	C4075-103	Unit
Spectral responsse range	λ	400 to 1000	nm
Output uniformity	-	15	%
Amp. gain	-	10^7	V/A
Frequency response	-	DC to 10 k	Hz
Supply voltage	V_S	15	V
Current consumption	P	2.5	W

Table 3.3.1-2 Specification of Multi-channel Pin-Diode array (Hamamatsu S3805)

General Rating

Parameters	Symbol	Value	Unit
Number of element	-	16 x 16 (256)	
Active area (per 1 element)	A	1.3 x 1.3	mm
Element pitch	-	1.5	mm
Package	-	Glass epoxy PC board	
Window material	-	Flat glass	

Absolute maximum ratings

Parameters	Symbol	Value	Unit
Reverse voltage	V_R	15	V
Consumption electric power	P	150	mW
Operating temperature	T_{opr}	-20 to +60	°C
Strage temperature	T_{stg}	-20 to +80	°C

Electrical and optical characteristics

Parameters	Symbol	Condition	Min.	Typ.	Max.	Unit
Spectral responsse range	λ			320 to 1000		nm
Peak sensitive wavelength	λ_p			800		nm
Photo sensitivity	S	$\lambda = \lambda_p$	0.4	0.5		A/W
Dark current	I_D	$V_R = 5$ V		0.1	1.0	nA
Cut-off frequency	f_c	$V_R = 5$ V, $R_L = 50\Omega$, $\lambda = 690$ nm		100		MHz
Rise time	t_r	$V_R = 5$ V, $R_L = 50\Omega$, $\lambda = 690$ nm		3.5		ns
Terminal capacitance	C_t	$V_R = 5$ V, $f = 1$ MHz		15		pF

Table 3.3.1-3 Specifications of CA-296L2 Amplifier

Model	CA-206L2
Description	Programmable Gain Amplifier
Input configuration	unbalanced
Gain	1, 2, 5, 10, x 1, x 10
Frequency response	DC to 500kHz
Full power bandwidth	DC to 100kHz
Max. output voltage	±10V
Max. output current	±5 mA
Supply voltage :	±15V
Dimensions (mm)	51.5 x 14 x 5.5, 20 pins
Package	Single-in-line package

Table 3.3.2-1 Specifications of EM-CCD Detector (ANDOR DU741N)

Camera Overview

Active Pixels	1600 x 400
Pixel Size (W x H; μm)	16 x 16
Image Area (mm)	25.6 x 6.4
Active Area Pixel Well Depth (e-; typical)	150,00
Output Saturation (e-; typical) 　　　High Responsivity Mode 　　　High Signal Mode	 300,00 1,300,000
Max spectra per sec (FVB) High Responsivity Mode High Signal Mode	 400 380
Read Noise @ 3MHz (e-, typical) High Responsivity Mode High Signal Mode (EM on)	 18 <1

System Characteristics

Pixel Readout Rate (MHz)	3, 1, 0.05
Linearity (%, maximum)	1
Vertical Clock Speed (μs)	4.9 to 50 (software selectable)
Electron Multiplier Gain (software controlled)	1 – 1000 times
Digitization (at all readout speeds)	16 bit
Camera window type	Single quartz window, AR coating available

Table 3.3.2-2 Specifications of EM-CCD Detector (ANDOR DU741N) (continued)

Dark Current and Background Events

Dark Current	
@-70°C (-e/pix/sec) for back illuminated device [front illuminated device]	0.003 [0.002]
@-100°C (-e/pix/sec) for back illuminated device [front illuminated device]	0.0001 [0.00008]
EM-CCD Amplified Background Events (events/pix) @ x1000 EM Gain, minimum exposure, -70°C	0.005

System Readout Noise (e-; typical)

Pixel Readout Rate (MHz)	High Responsivity Output	Electron Multiplying Output	
		(EM off)	(EM on)
0.05	2.5	10	<1
1	7	22	<1
3	18	35	<1

Table 3.5-1 Specifications of NI6559 Data Acquisition Module

Analog Input

Number of channels

NI 6254/NI 6259.................................... 16 differential or 32 single ended

ADC resolution .... 16 bits

Sampling rate

    Maximum.. 1.25 MS/s single-channel

                                   1.00 MS/s multichannel

    Minimum... 0 S/s

Timing accuracy .... 50 ppm of sample rate

Timing resolution .... 50 ns

Input coupling.. DC

Input range .... ±10, ±5, ±2, ±1, ±0.5, ±0.2, ±0.1 V

Maximum working voltage for analog

inputs (signal + common mode) .... ±11 V of AI GND

Input impedance

  AI+ to AI GND................................ >10 GΩ/2 in parallel with 100 pF

  AI– to AI GND................................ >10 GΩ/2 in parallel with 100 pF

Input bias current .... ±100 pA

Crosstalk (at 100 kHz)

Adjacent channels . ... -75 dB

Nonadjacent channels. .... -95 dB

Small signal bandwidth (–3 dB) .... 1.7 MHz

Data transfers .... DMA (scatter-gather), interrupts,

                                     Programmed I/O

Settling Time for Multichannel Measurements

Range (V)	±60 ppm of Step (±4 LSB for Full Scale Step)	±15 ppm of Step (±1 LSB for Full Scale Step)
±10, ±5, ±2, ±1	1 μs	1.5 μs
±0.5	1.5 μs	2 μs
±0.2, ±0.1	2 μs	8 μs
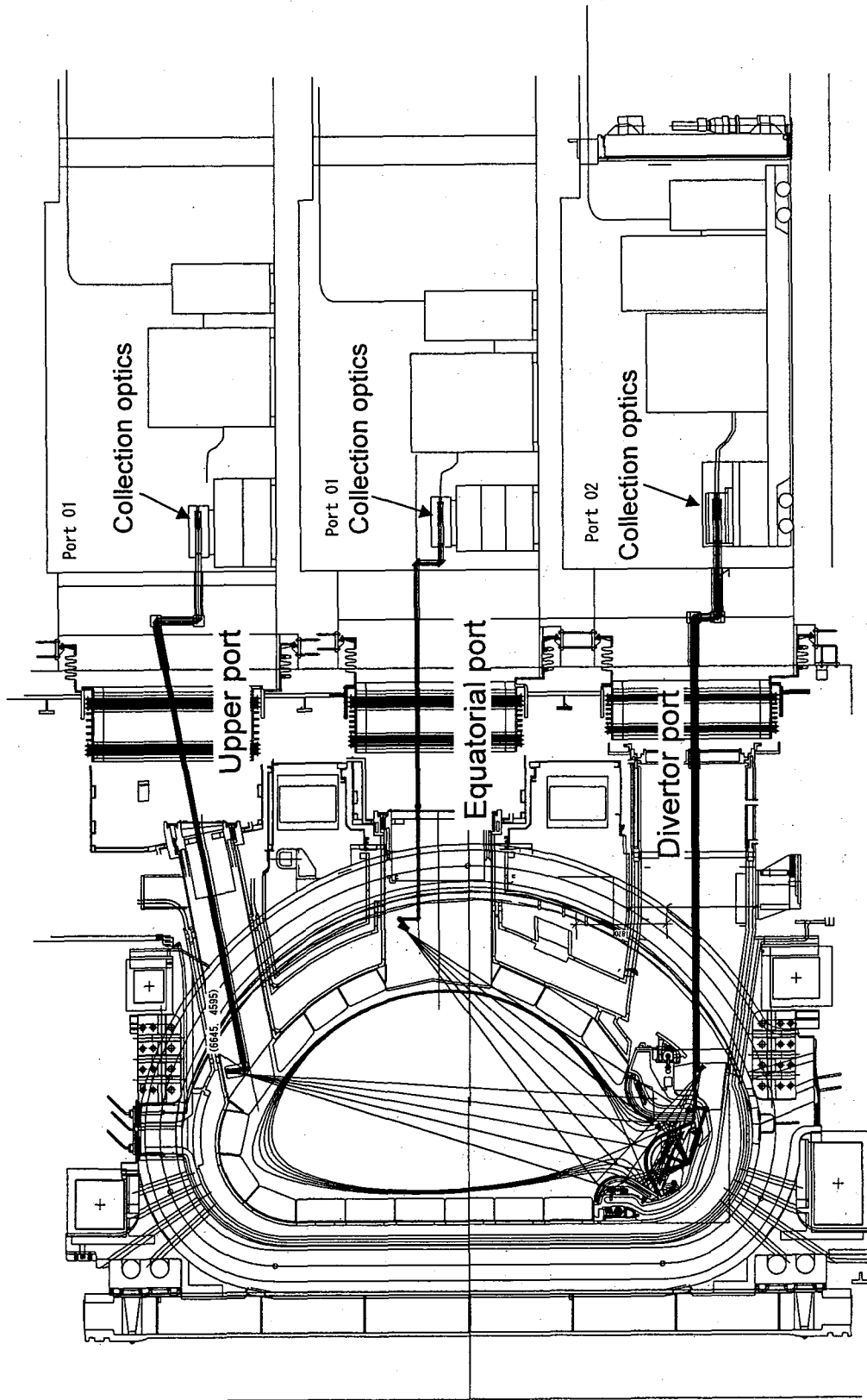
Fig. 2.1-1 Viewing fans of Impurity Influx Monitor (divertor).

(a)

From Upper Port
(71 sight lines)

From Equatorial Port
(71 sight lines)

Through the gap (10 mm)
between the divertor
cassettes
(73 sight lines)

Dome

Divertor Port

Mirrors for
central optics

From divertor cassette
(43 sight lines each)

Mirrors for
central optics

Mirrors for
side optics

(b)

IH

IV

OV

OH

central optics
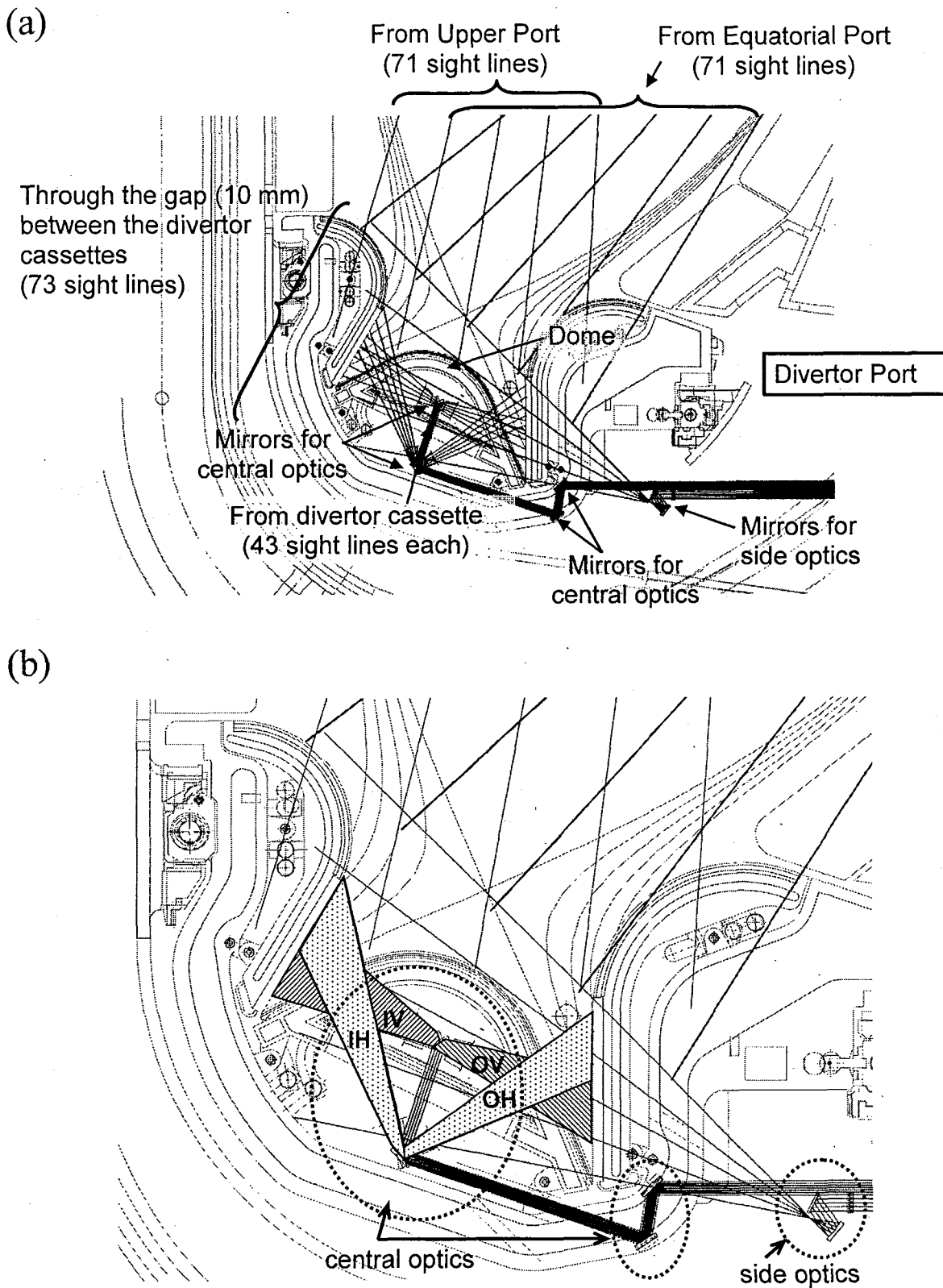
side optics

Fig. 2.1-2 Viewing fans of central and side optics in the divertor region.
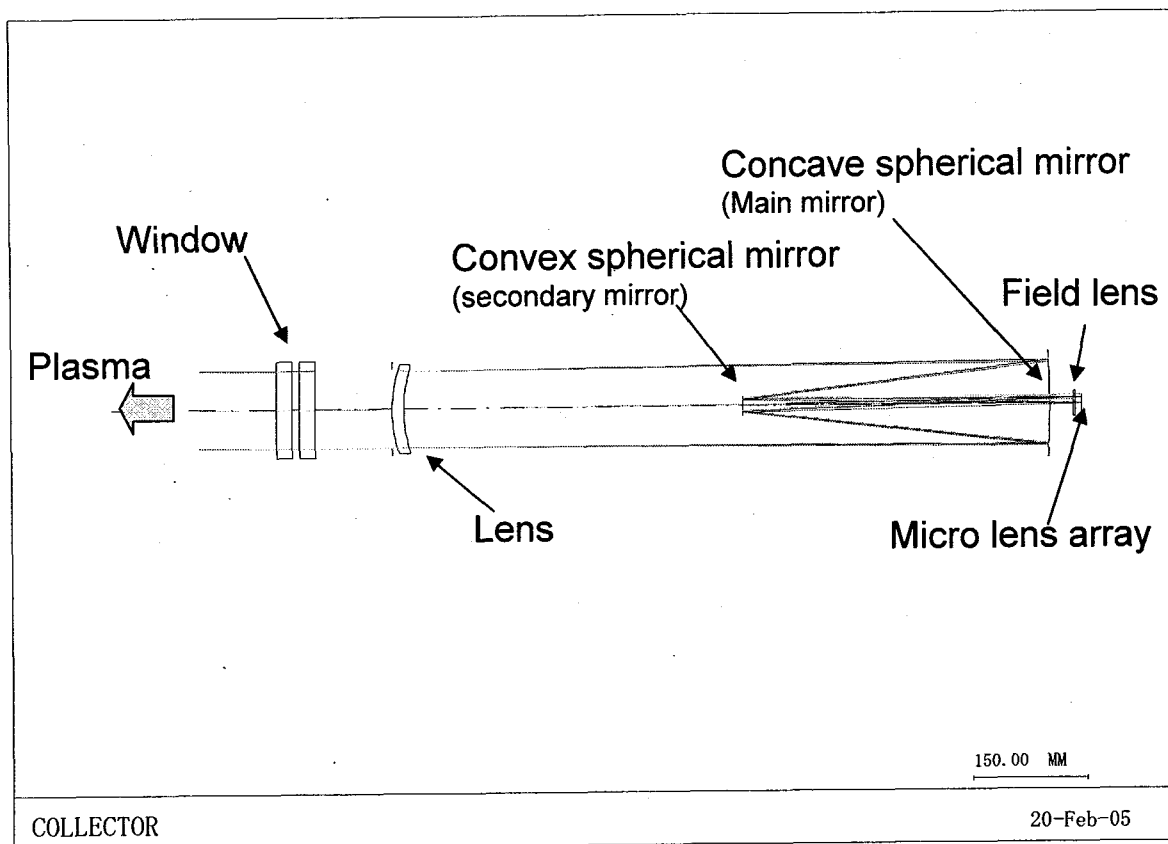
Fig. 2.1-3 Collection optics.

< Top View for central optics of divertor>
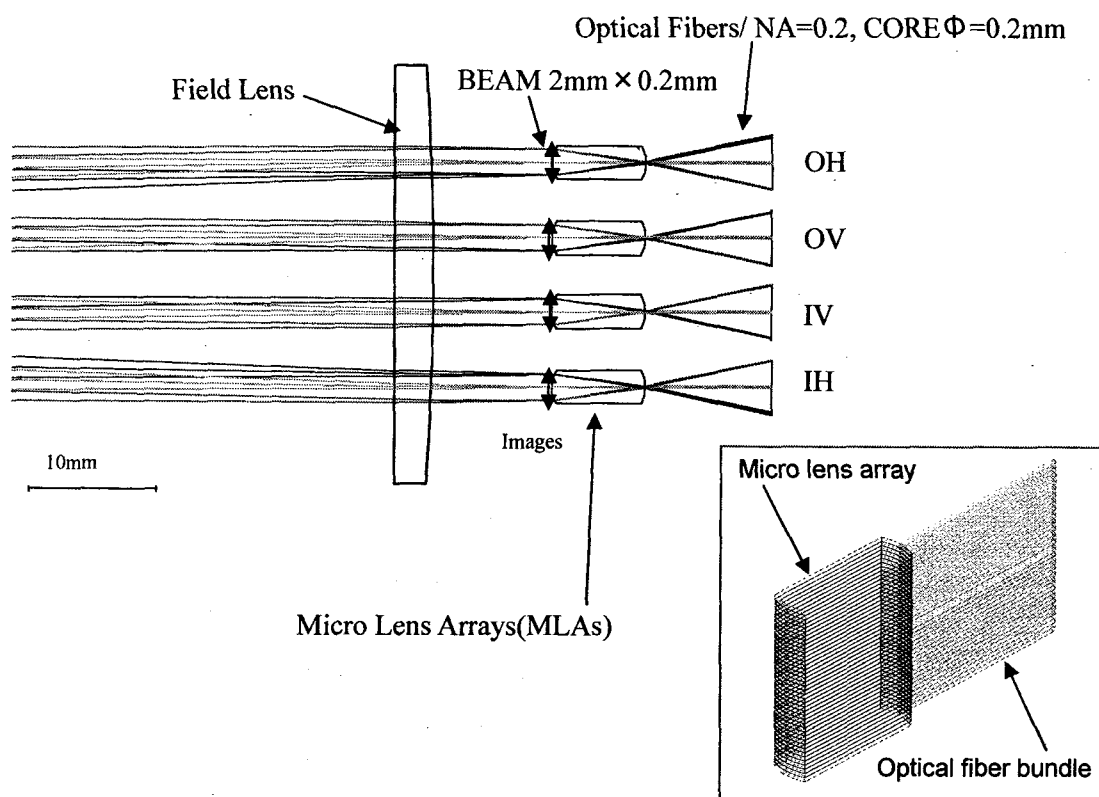
Fig. 2.1-4 Micro lens array is inserted just in front of the fiber bundle to increase the light collected.
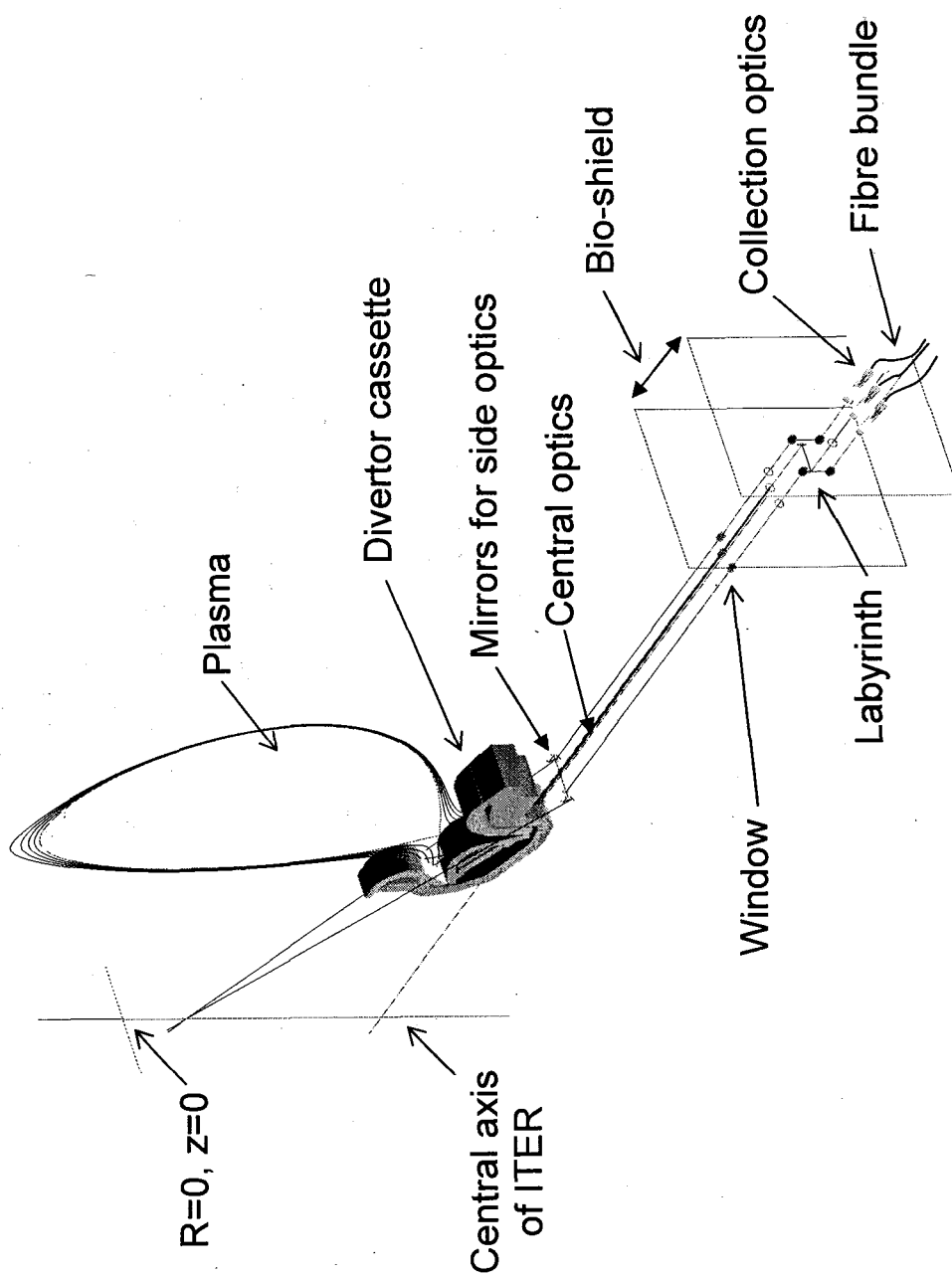
Fig. 2.2.1-1 Schematic view of the measurement optical systems from the divertor cassette and the divertor port
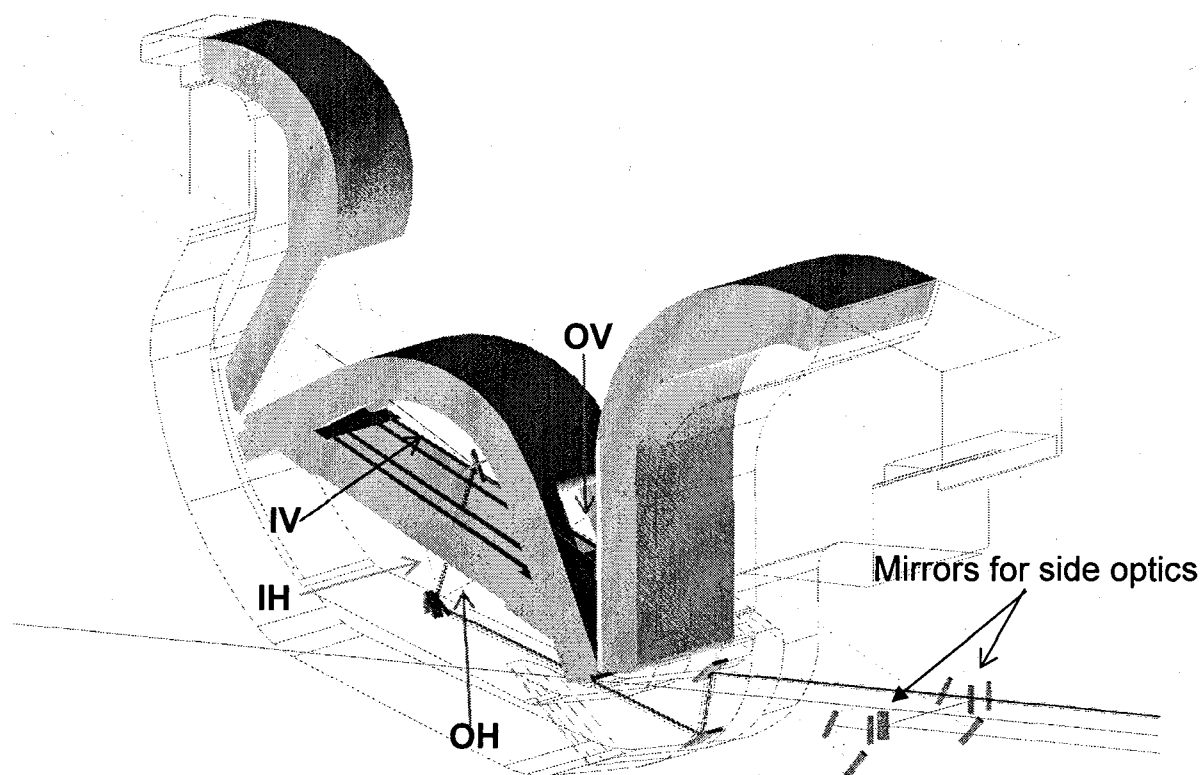
Fig. 2.2.1-2 Mirror arrangement and viewing fans in and just outside the divertor cassette.
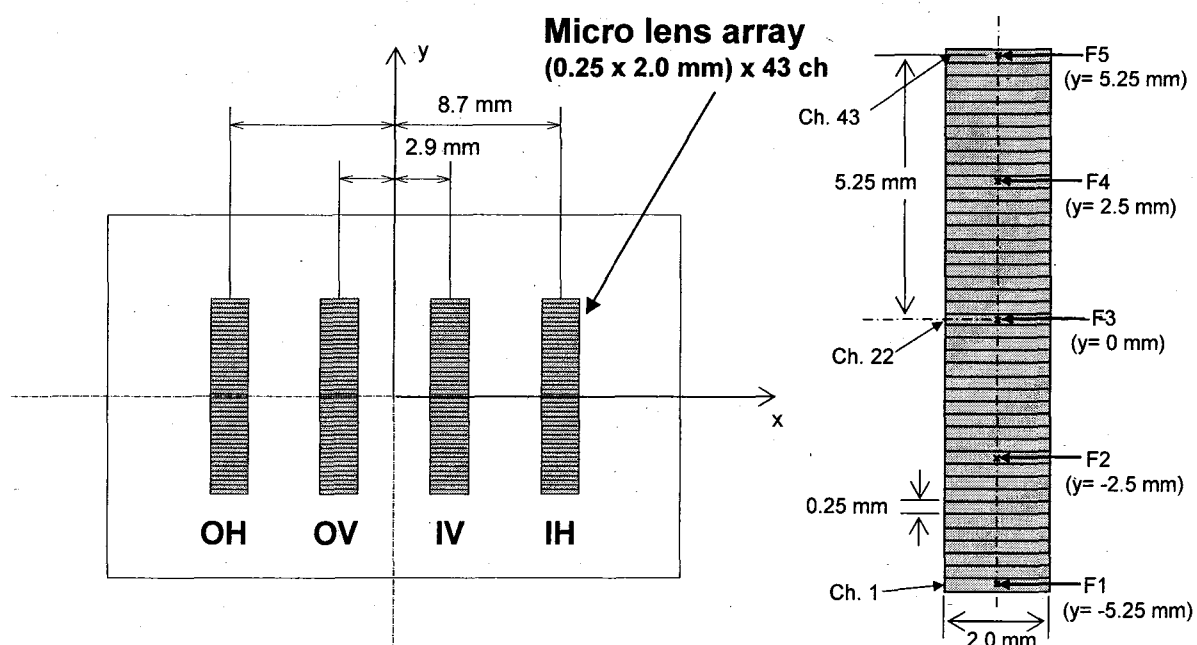
Fig. 2.2.1-3 End of view of micro lens arrays for each viewing fan in Fig1.1.2-2.

<Cross section view>

Top view in the bio-shield

F1
F2
F3
F4
F5

At Fiber Array
F5
F4
F3
F2
F1

Collection optics

Plasma
(Inner divertor region)

2000.00 MM

IV-2005   24-Feb-05
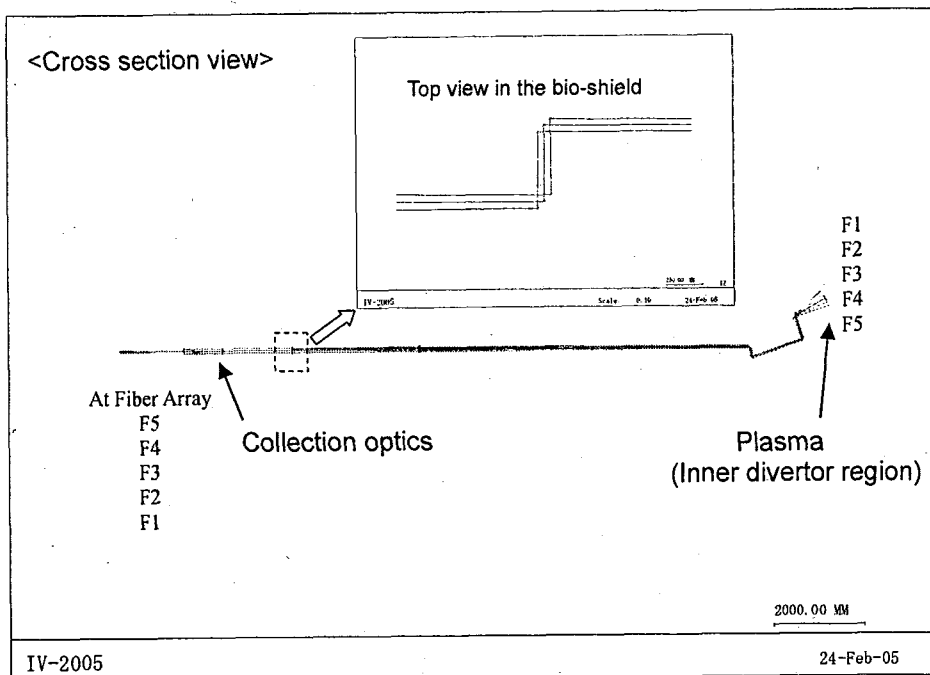
Fig. 2.2.2-1 (a) Traced rays for viewing fan IV.

Divertor plate

F1
F2
F3
F4
F5

Plasma
(Inner divertor region)

250.00 MM

IV-2005   Scale: 0.10   24-Feb-05
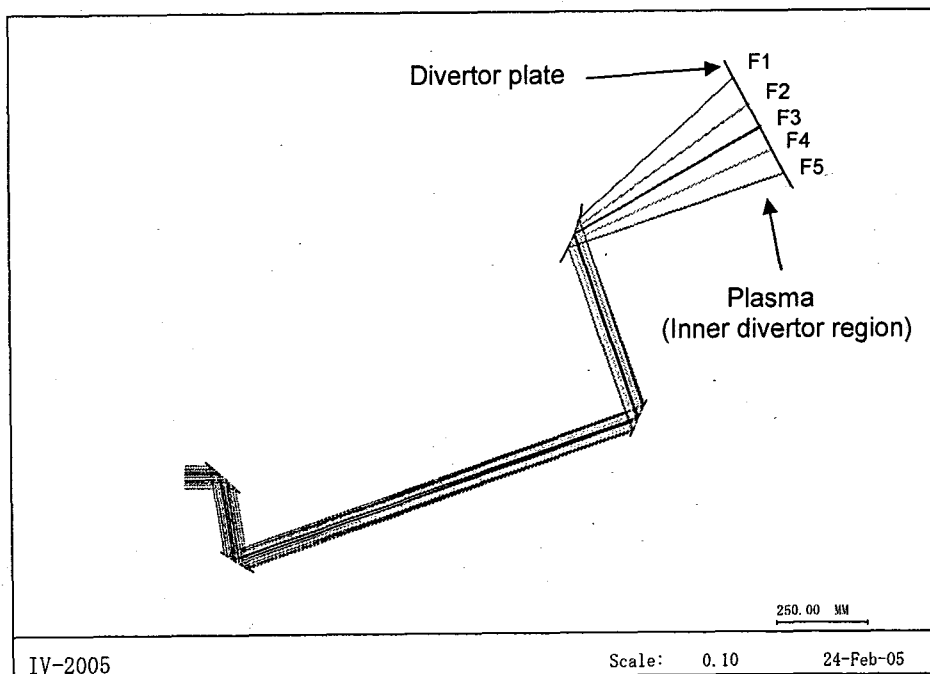
Fig. 2.2.2-1 (b) Expanded view of the traced rays for viewing fan IV in the divertor cassette.
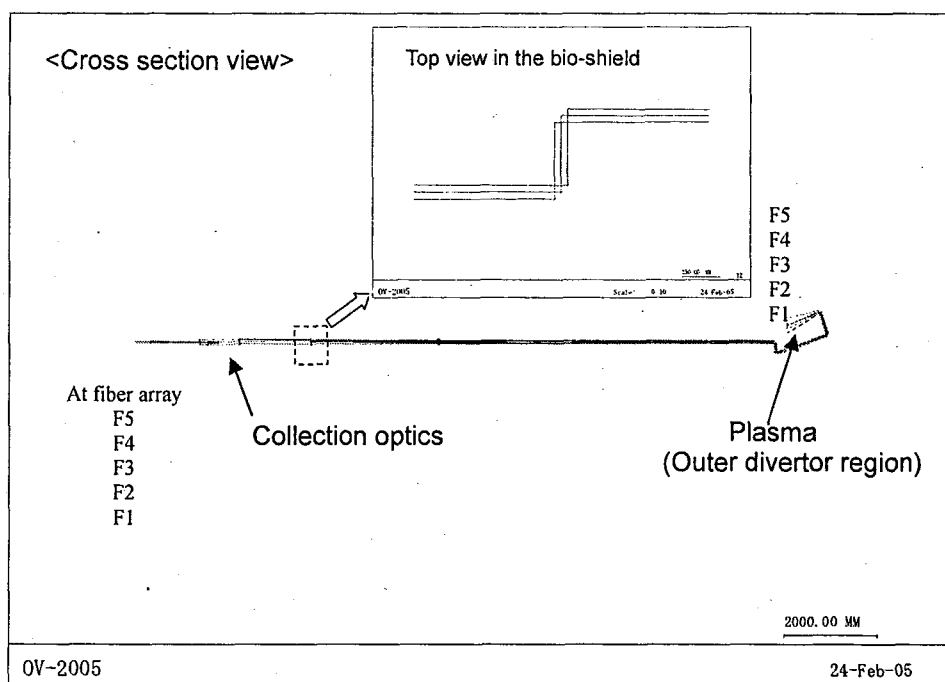
Fig. 2.2.2-2 (a) Traced rays for viewing fan OV.
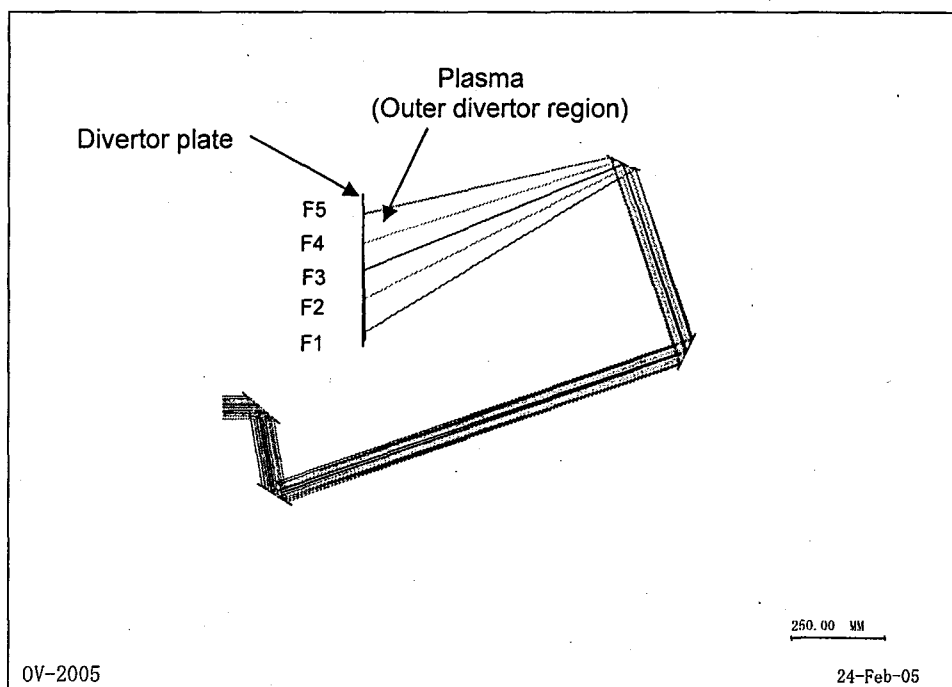
Fig. 2.2.2-2 (b) Expanded view of the traced rays for viewing fan OV in the divertor cassette.
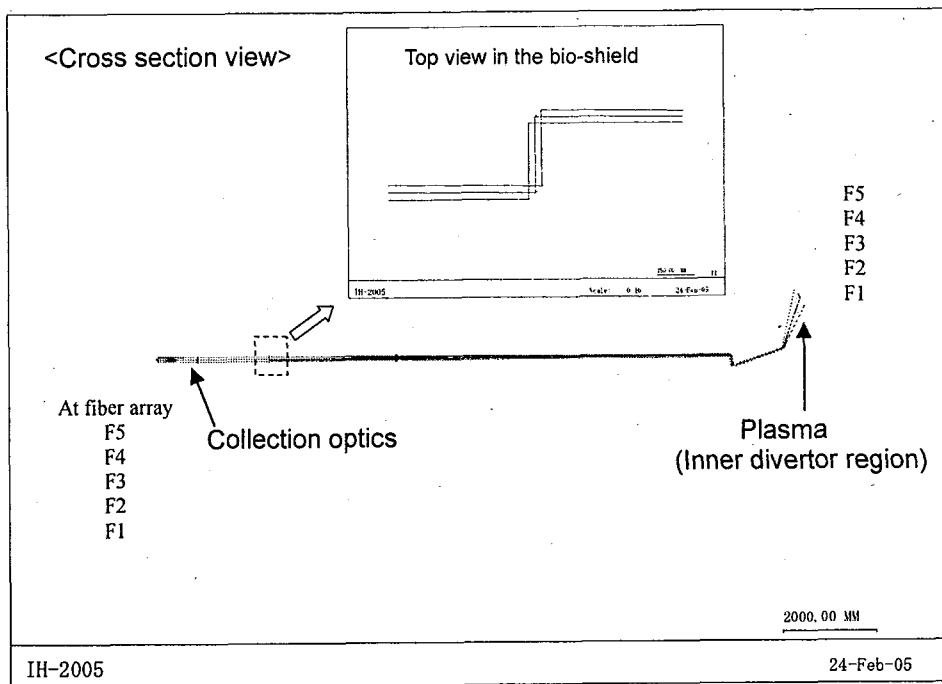
Fig. 2.2.2-3 (a) Traced rays for viewing fan IH.
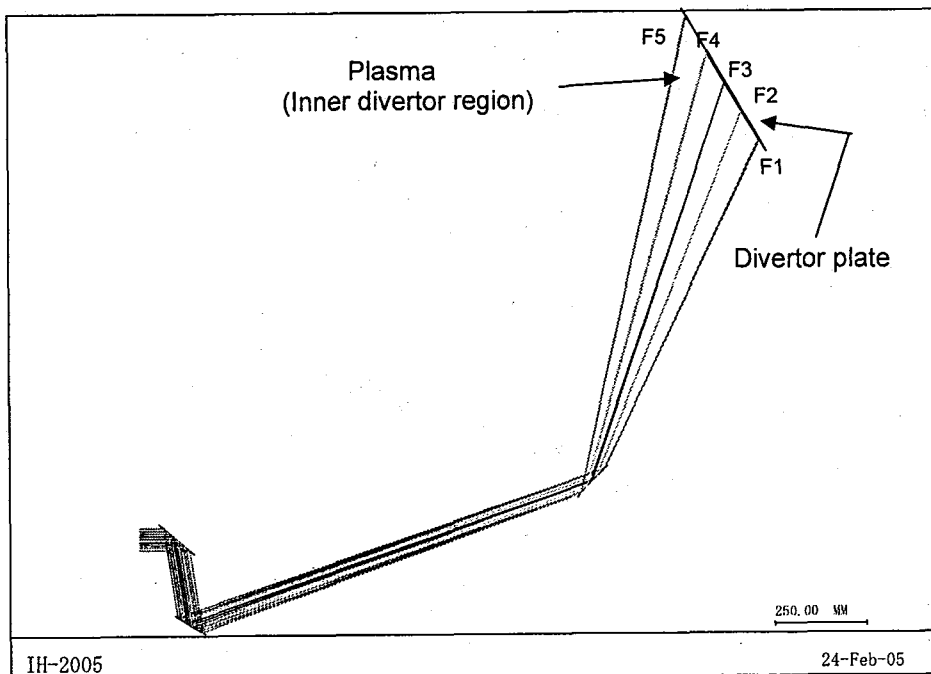
Fig. 2.2.2-3 (b) Expanded view of the traced rays for viewing fan IH in the divertor cassette.
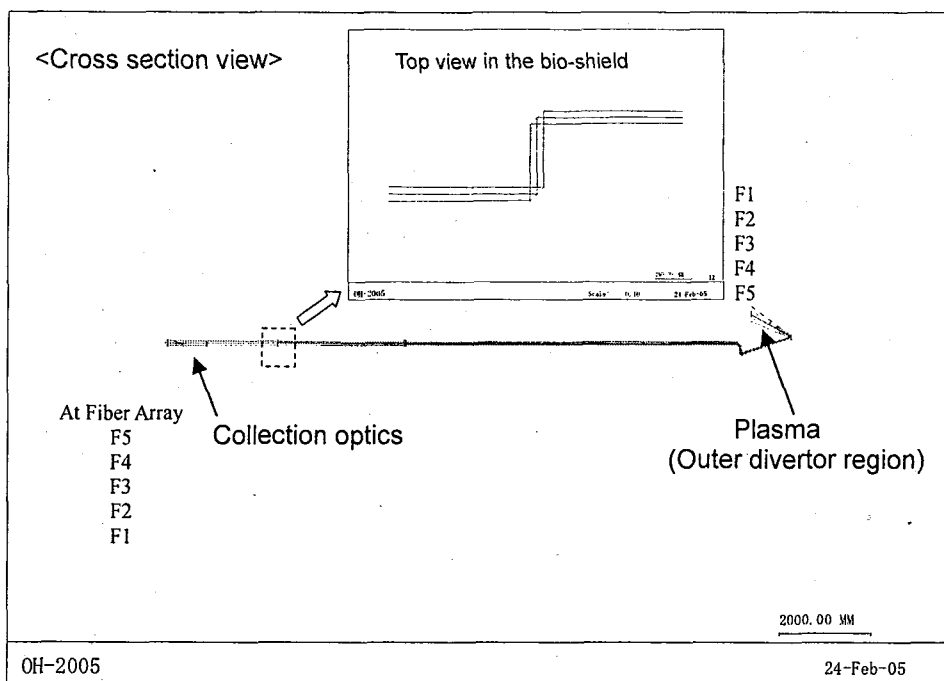
Fig. 2.2.2-4 (a) Traced rays for viewing fan OH.
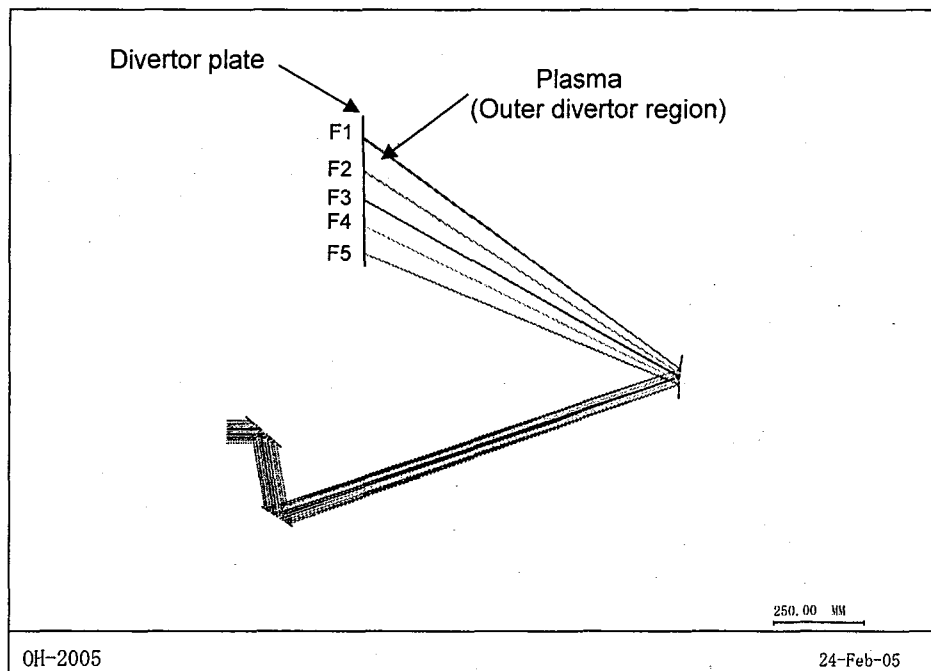
Fig. 2.2.2-4 (b) Expanded view of the traced rays for viewing fan OH in the divertor cassette.
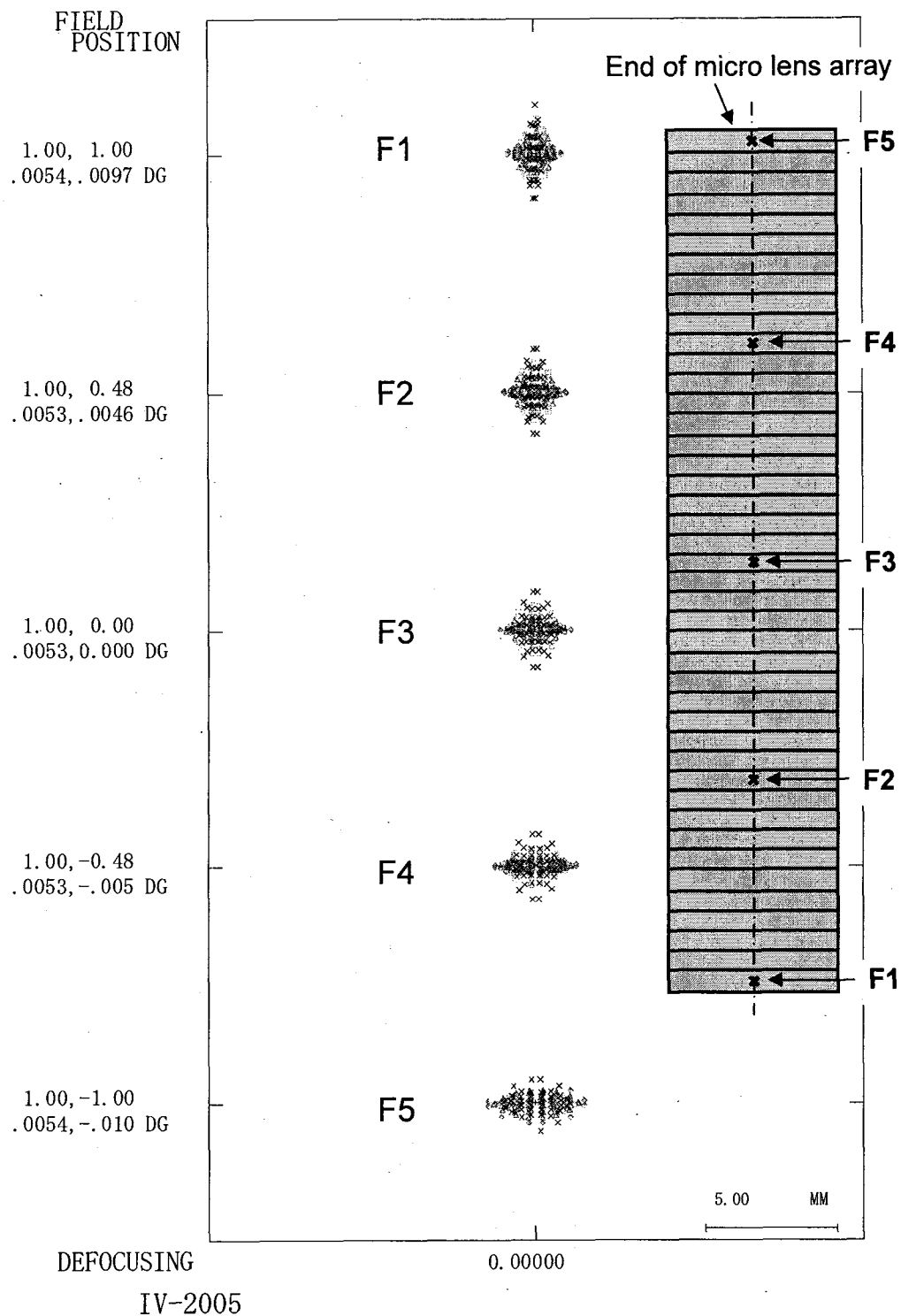
Fig. 2.2.2-5 Spot diagrams on the divertor plate for the viewing fan IV. Rays of the each field (F1, F2, F3, F4, F5) start from the center of the micro lens.
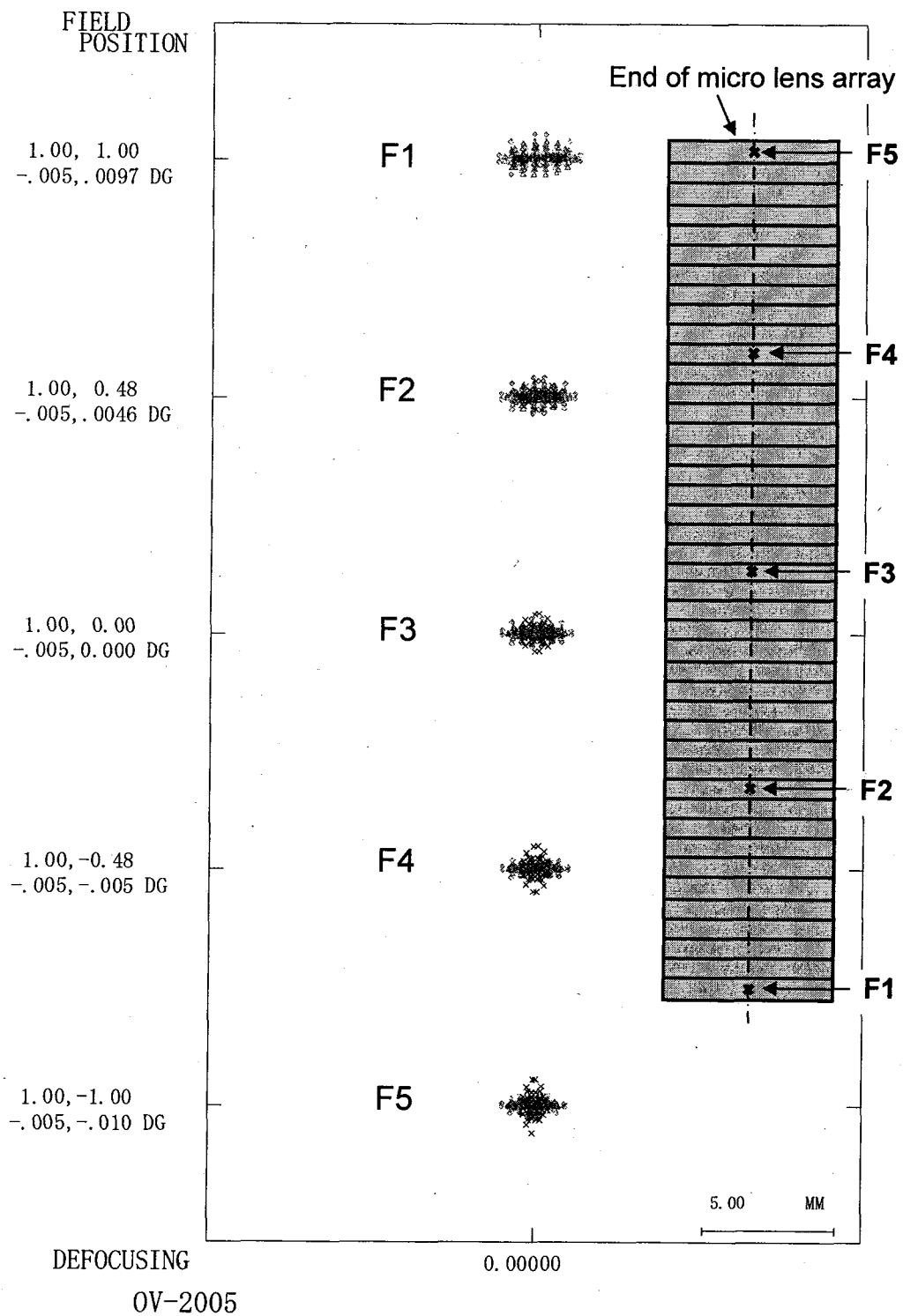
Fig. 2.2.2-6 Spot diagrams on the divertor plate for the viewing fan OV. Rays of the each field (F1, F2, F3, F4, F5) start from the center of the micro lens.
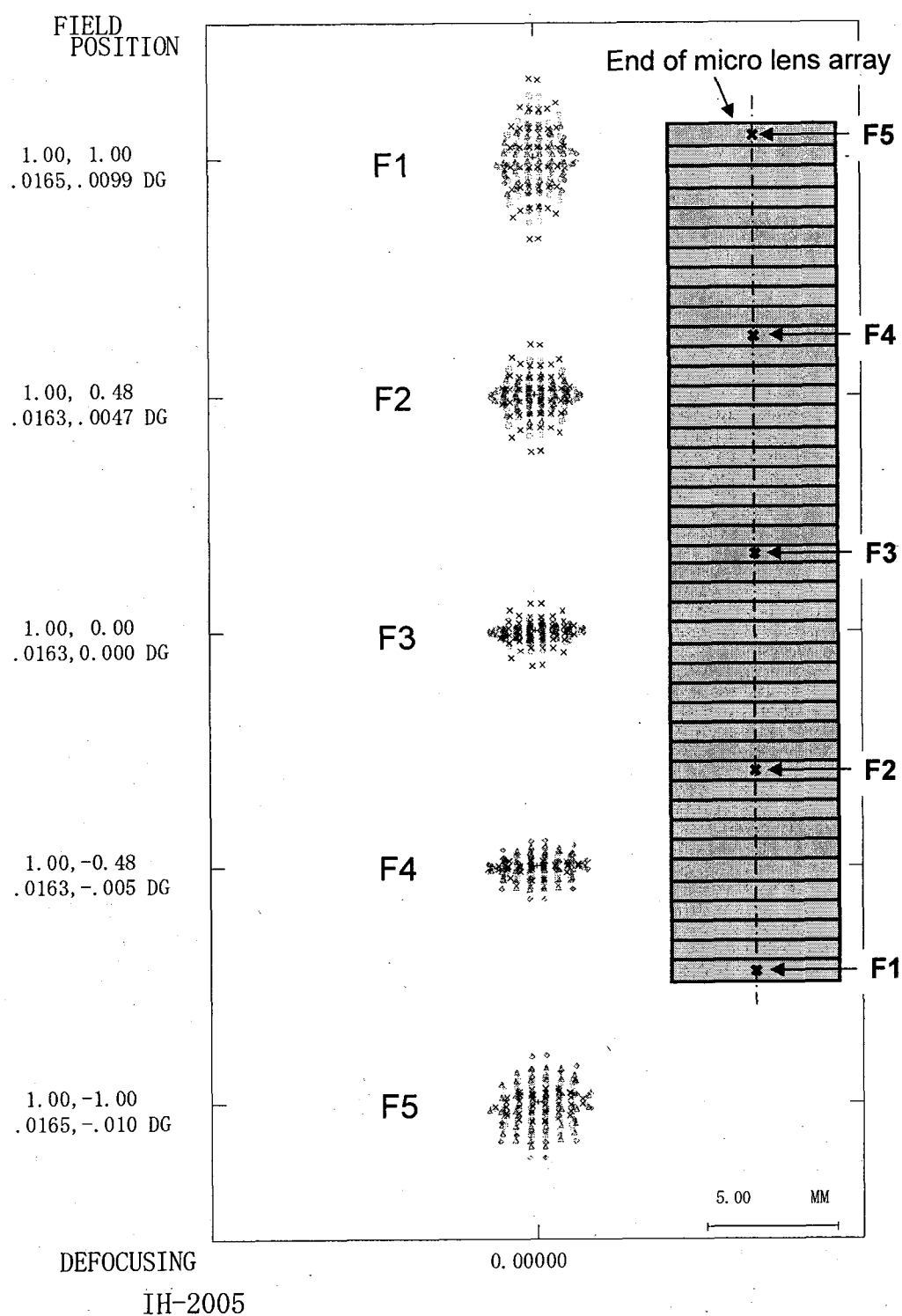
Fig. 2.2.2-7 Spot diagrams on the divertor plate for the viewing fan IH. Rays of the each field (F1, F2, F3, F4, F5) start from the center of the micro lens.
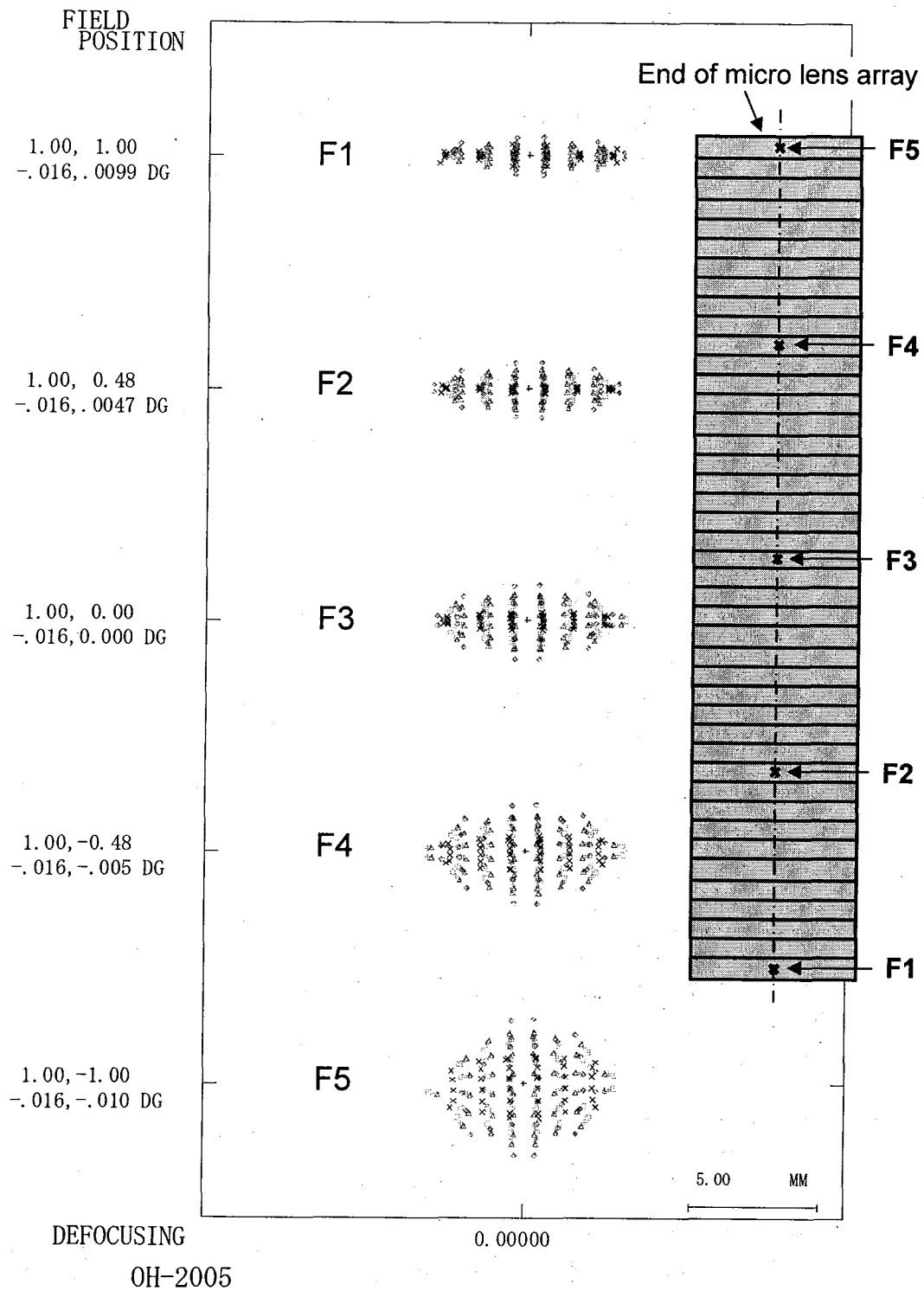
Fig. 2.2.2-8 Spot diagrams on the divertor plate for the viewing fan OH. Rays of the each field (F1, F2, F3, F4, F5) start from the center of the micro lens.
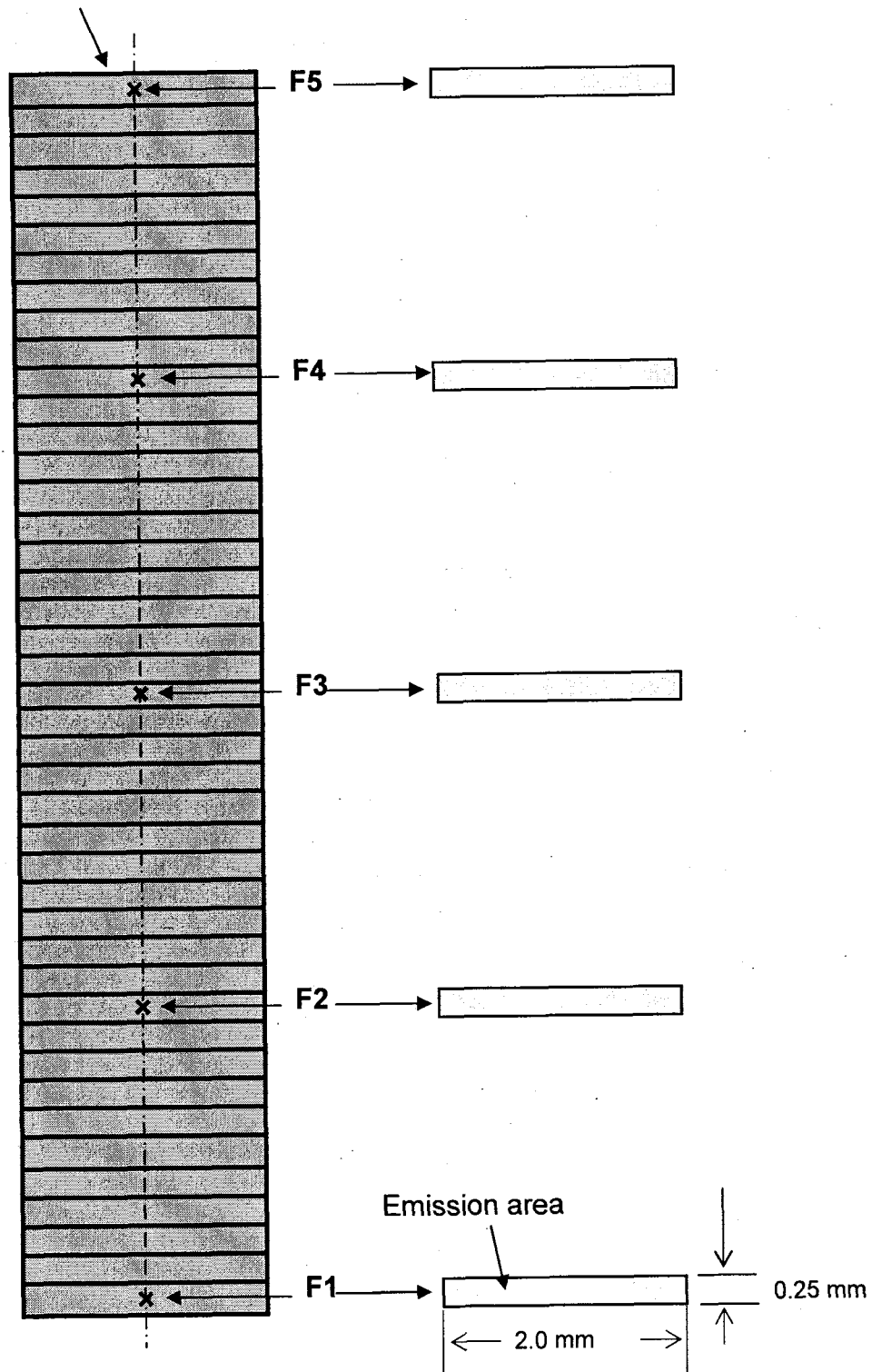
Fig. 2.2.2-9 Light is emitted from the area of the end of the micro lens corresponding line of sight (F1, F2, F3, F4, F5). We assume the uniform emission from the each area.
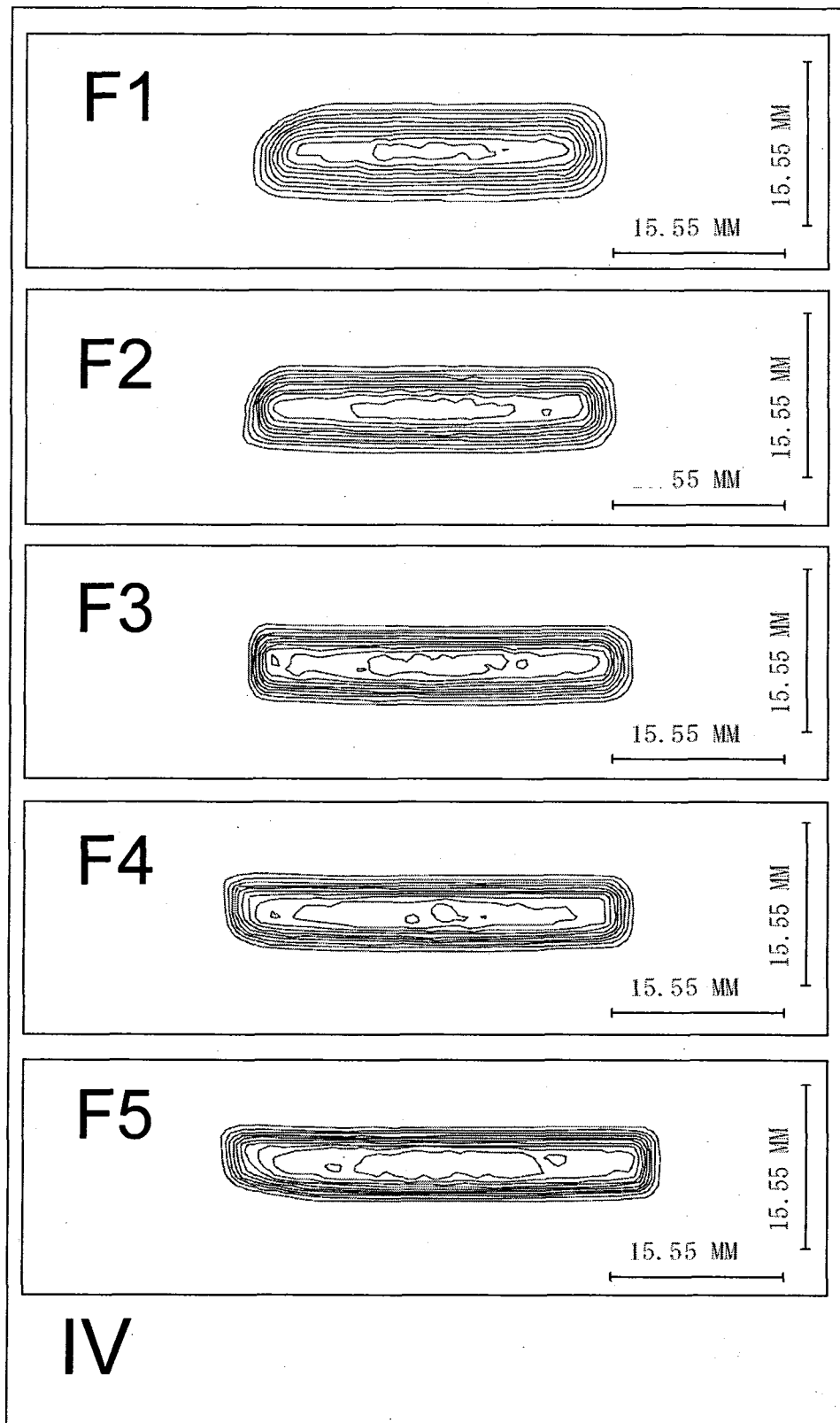
Fig. 2.2.2-10 Relative distributions of irradiances on the divertor plate for each line of sight of the viewing
fan IV. (Contour)
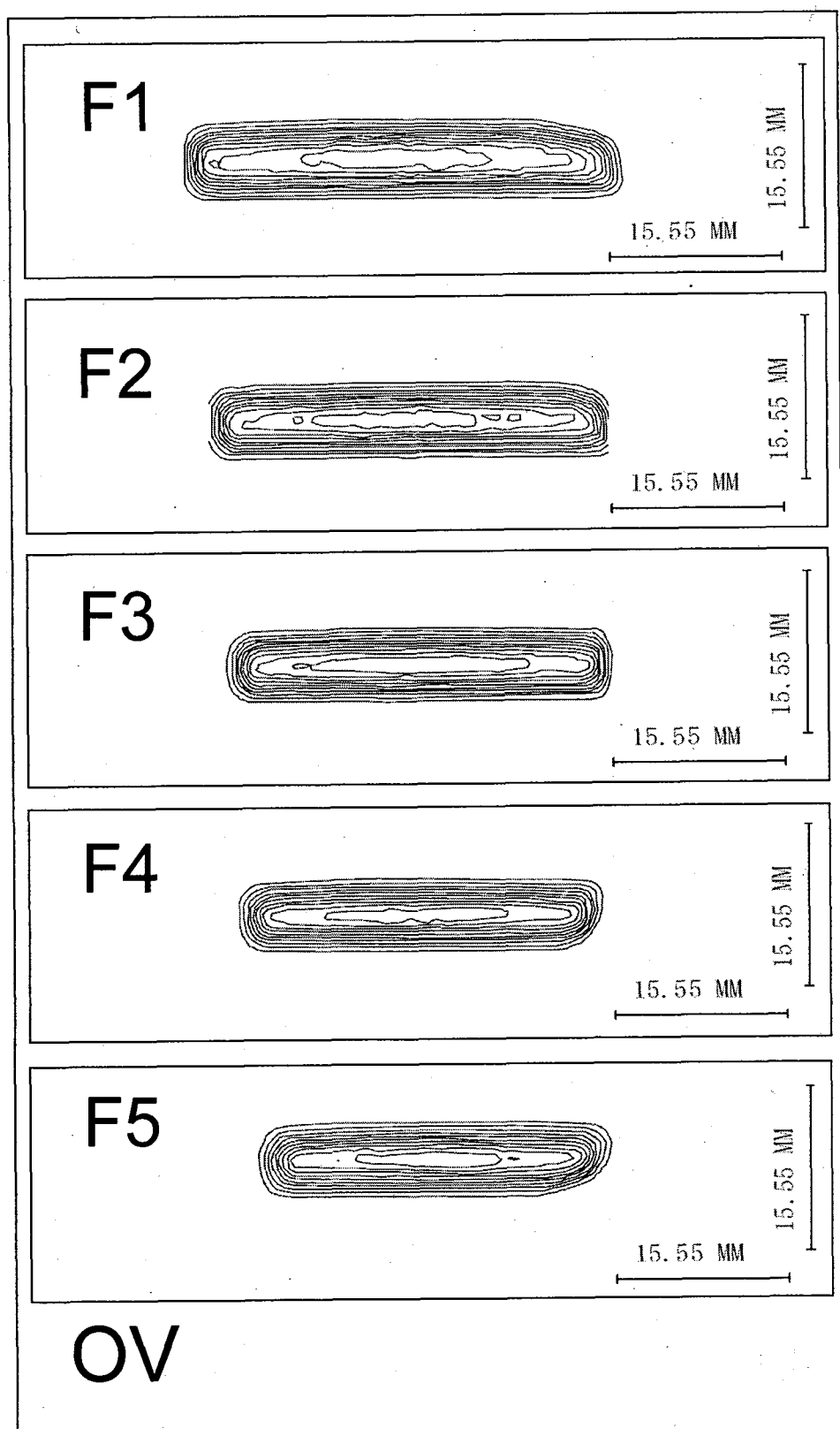
Fig. 2.2.2-11 Relative distributions of irradiances on the divertor plate for each line of sight of the viewing fan OV. (Contour)
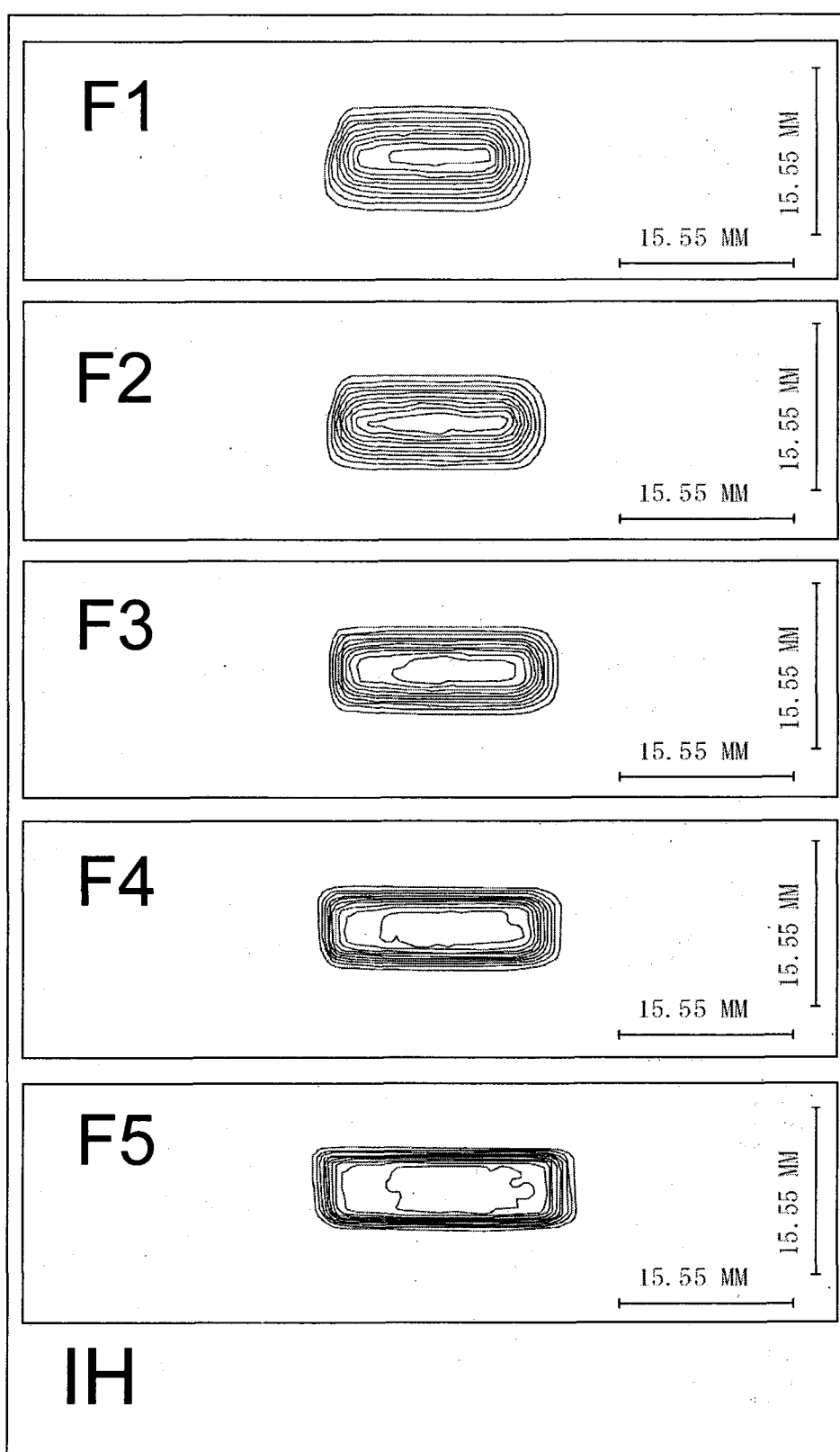
Fig. 2.2.2-12 Relative distributions of irradiances on the divertor plate for each line of sight of the viewing fan IH. (Contour)
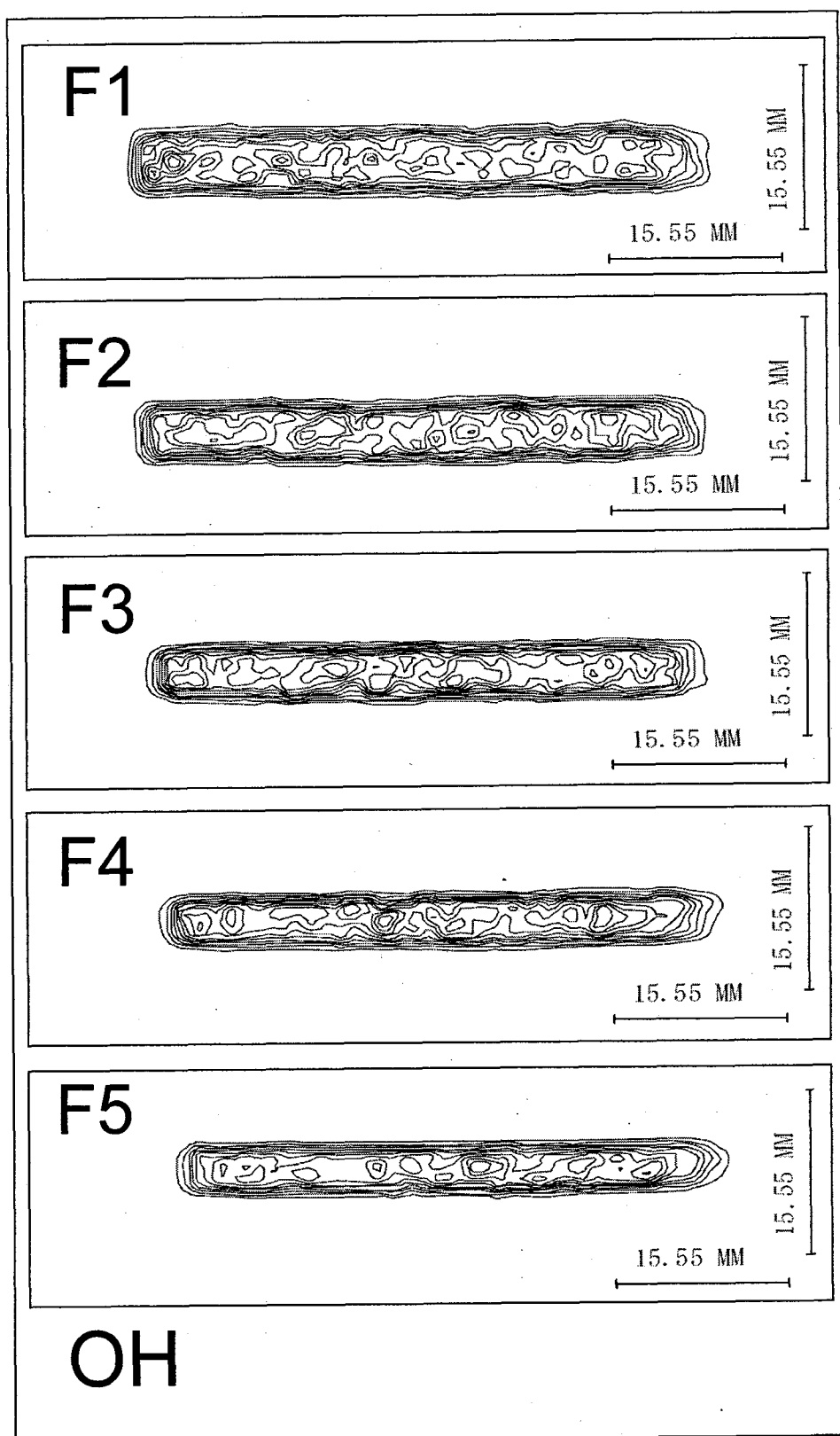
Fig. 2.2.2-13 Relative distributions of irradiances on the divertor plate for each line of sight of the viewing fan OH. (Contour)
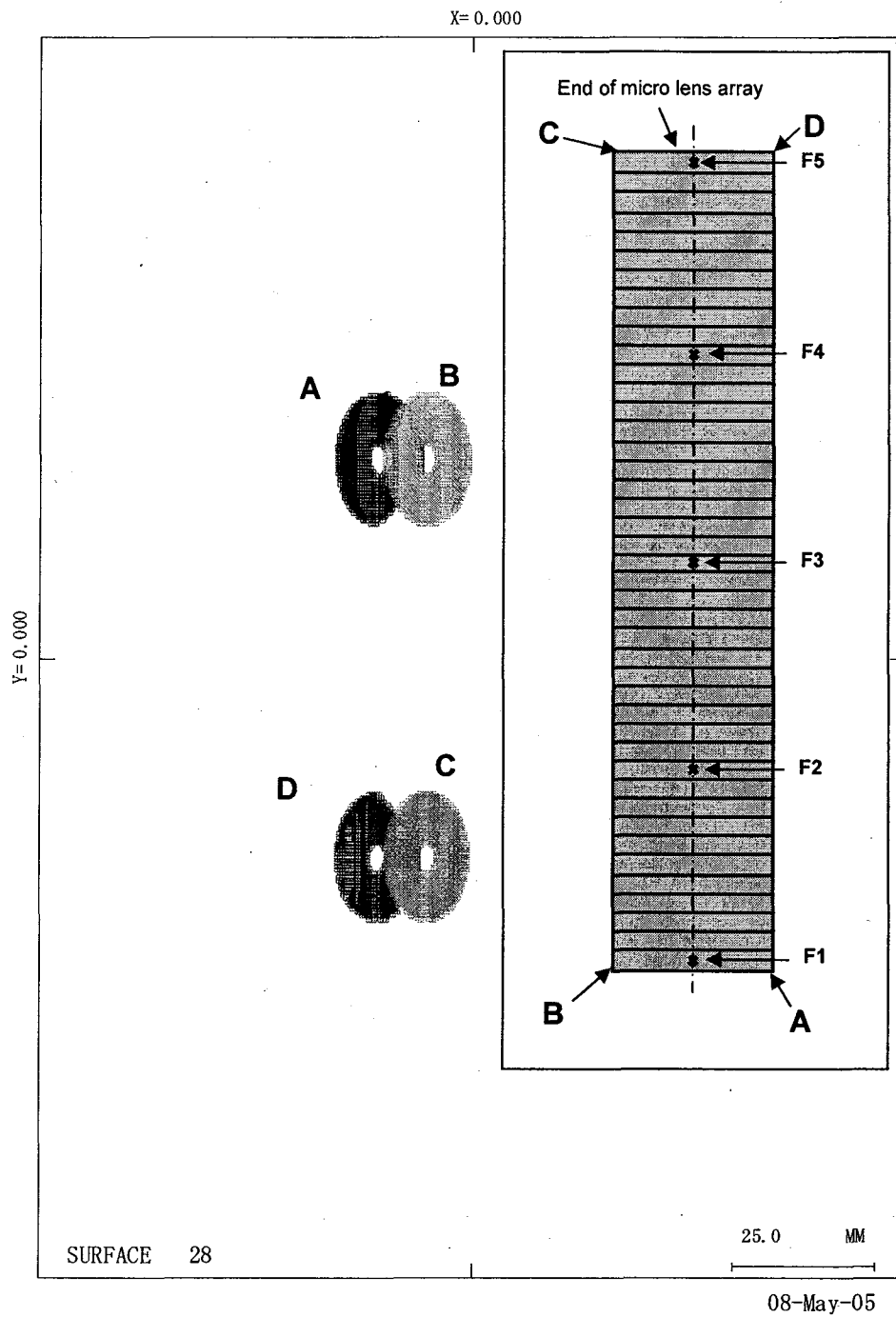
Fig.2.2.2-14 Footprints of the rays started from 4 corners (A, B, C, D) of the micro lens array on the mirror located at the entrance of the divertor cassette for the viewing fan of IV.

X= 0. 000

A   B

D   C

Y= 0.000

SURFACE   39

25. 0   MM
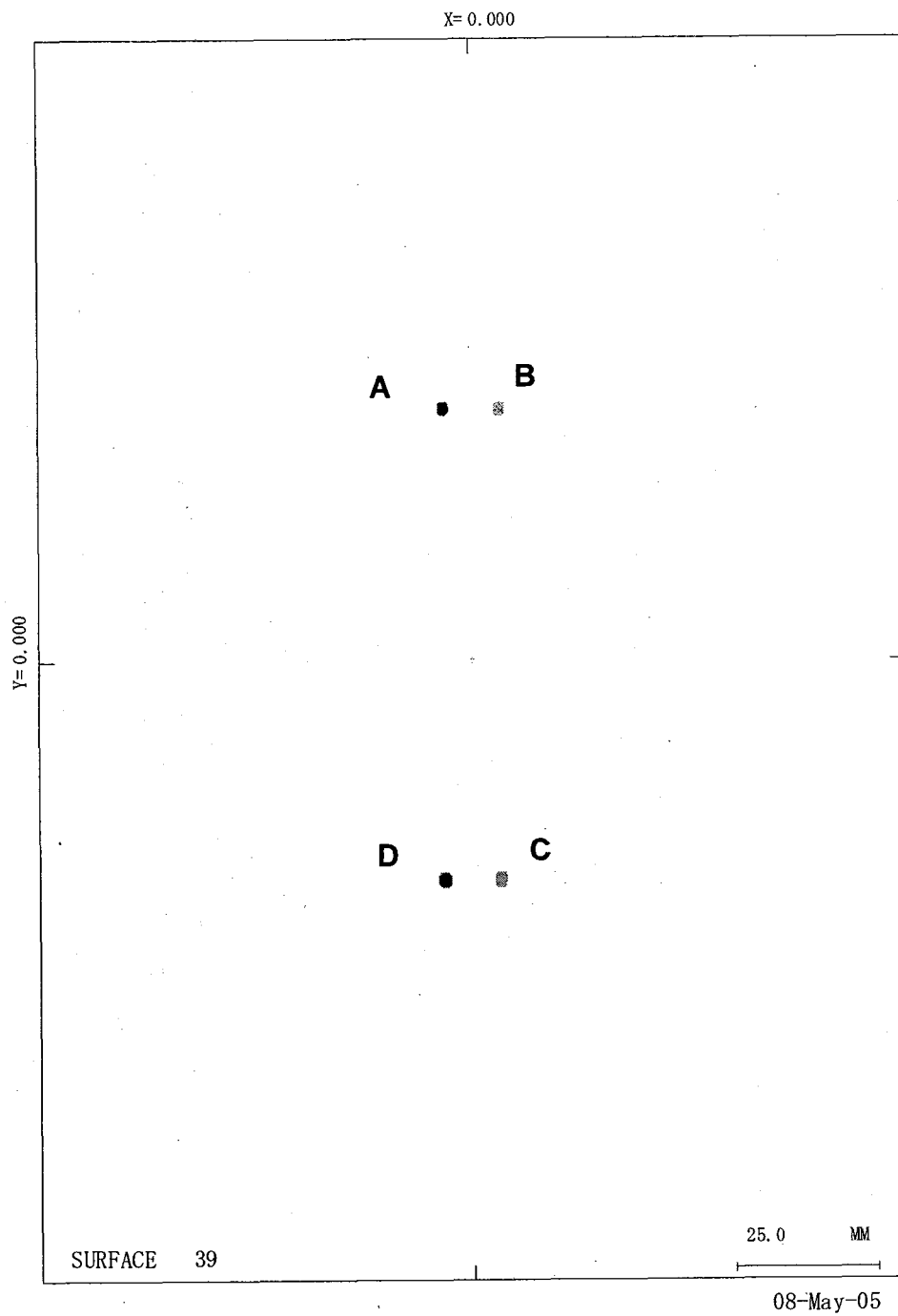
08-May-05

IV-2005 footprint

Fig.2.2.2-15 Footprints of the rays started from 4 corners (A, B, C, D) of the micro lens array on the mirror located at the dome for the viewing fan of IV.

X= 0.000

Effective diameter (120 mm) of window

Y= 0.000

SURFACE   24

25.0   MM
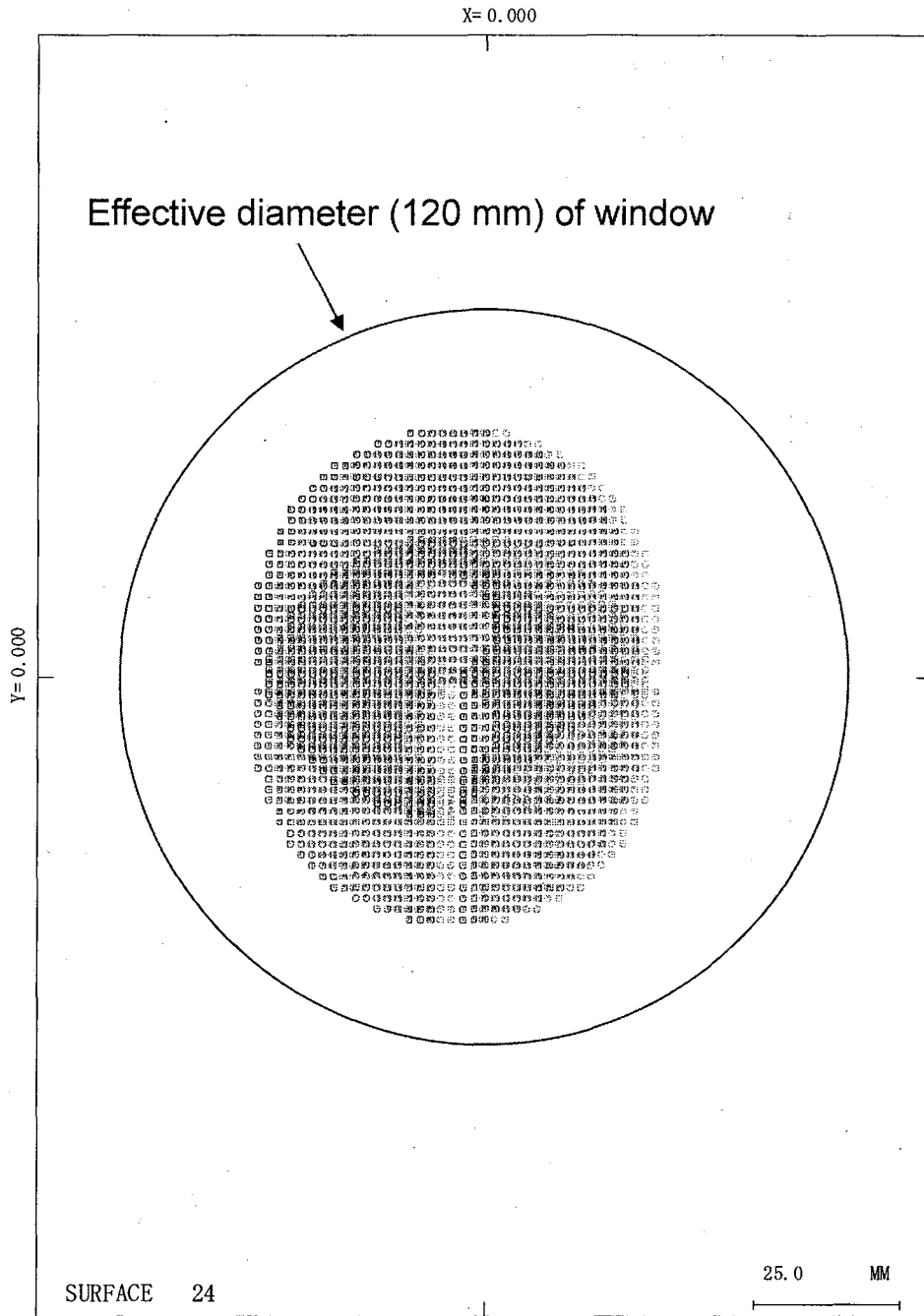
08-May-05

IV-2005 footprint

Fig. 2.2.2-16 Footprints of the rays started from 4 corners (A, B, C, D) of the micro lens array on the
window for the viewing fan of IV.
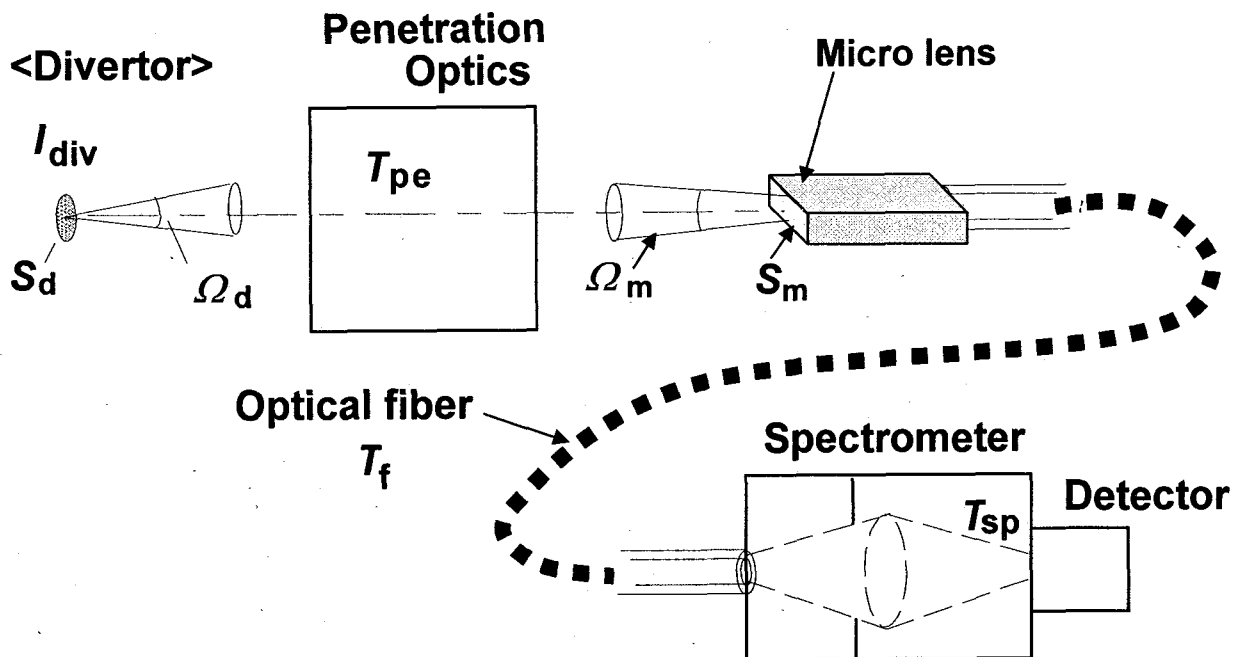
Fig.2.2.2-17 Transmission and solid angle of the optical system.
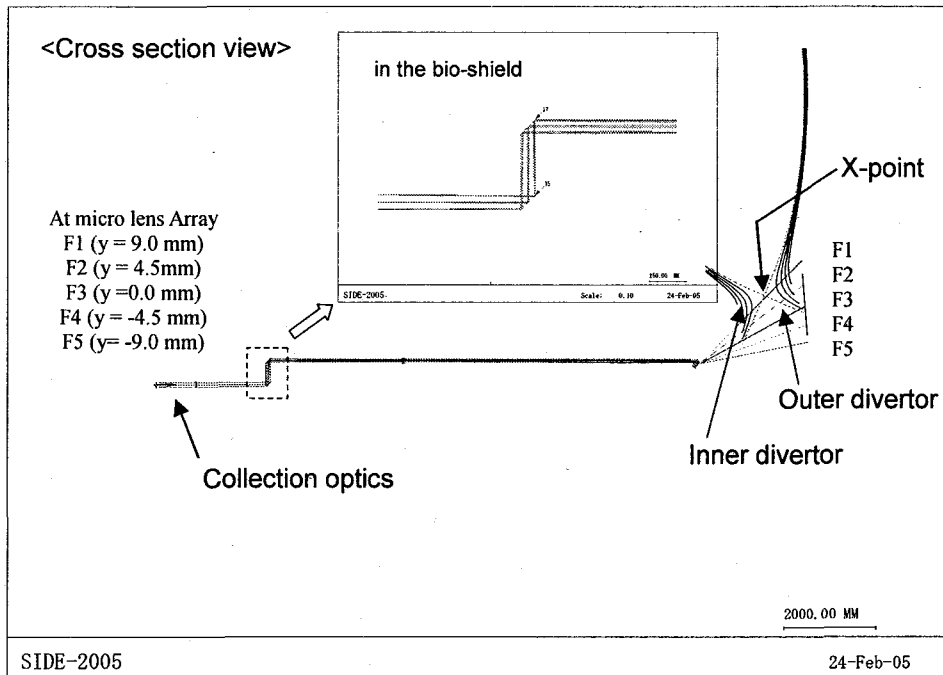
Fig. 2.2.3-1(a) Traced rays for side optics.
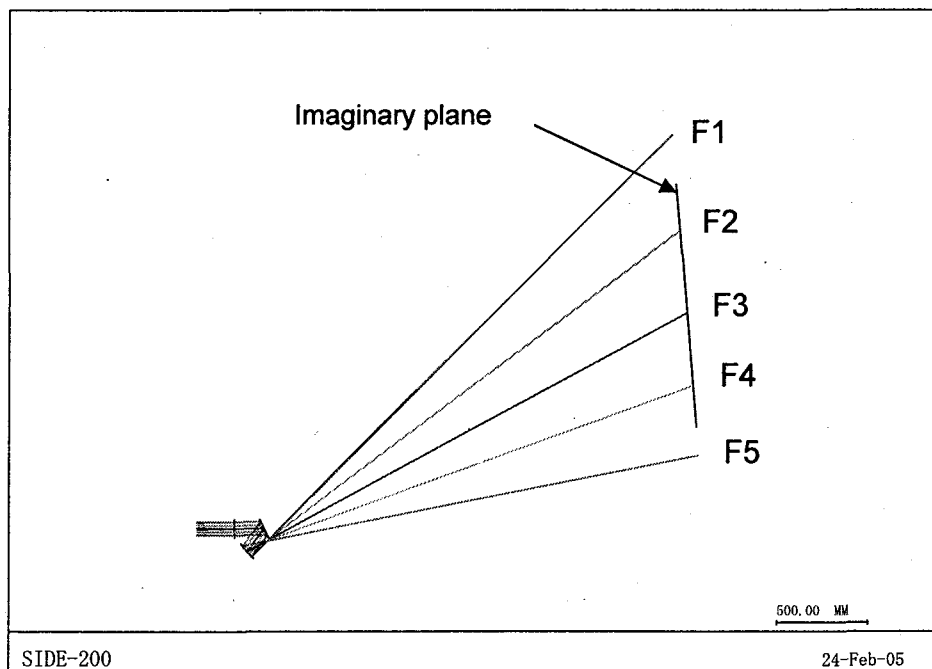
Fig. 2.2.3-1(b) Expanded view of the traced rays for side optics near the divertor.
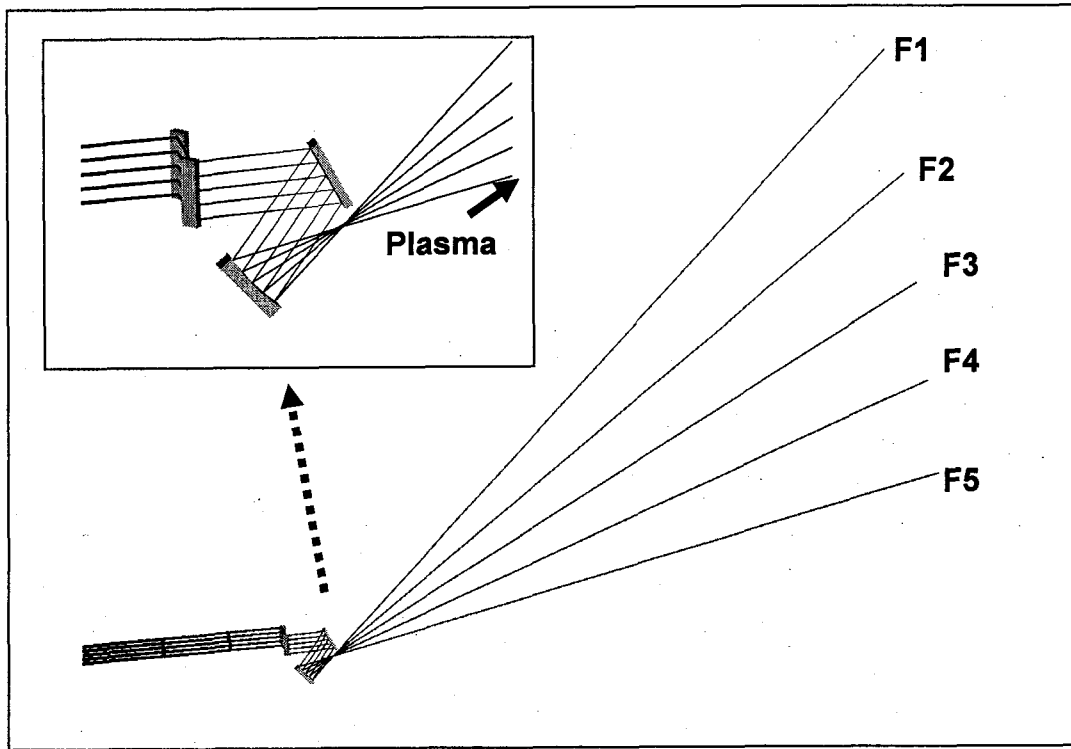
Fig. 2.2.3-2 Mirror arrangement and traced rays near the divertor.
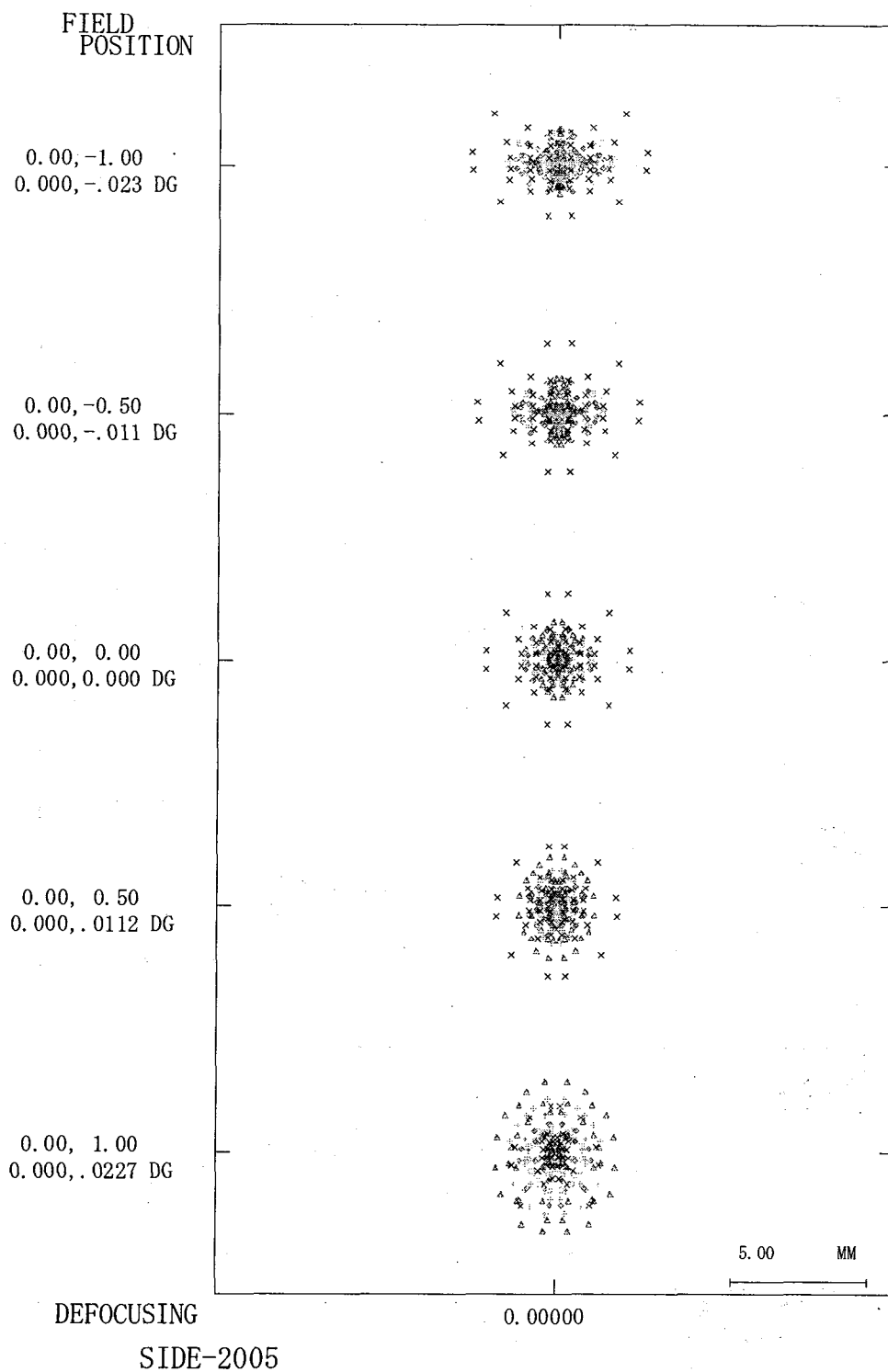
Fig. 2.2.3-3 Spot diagrams for the side optics.
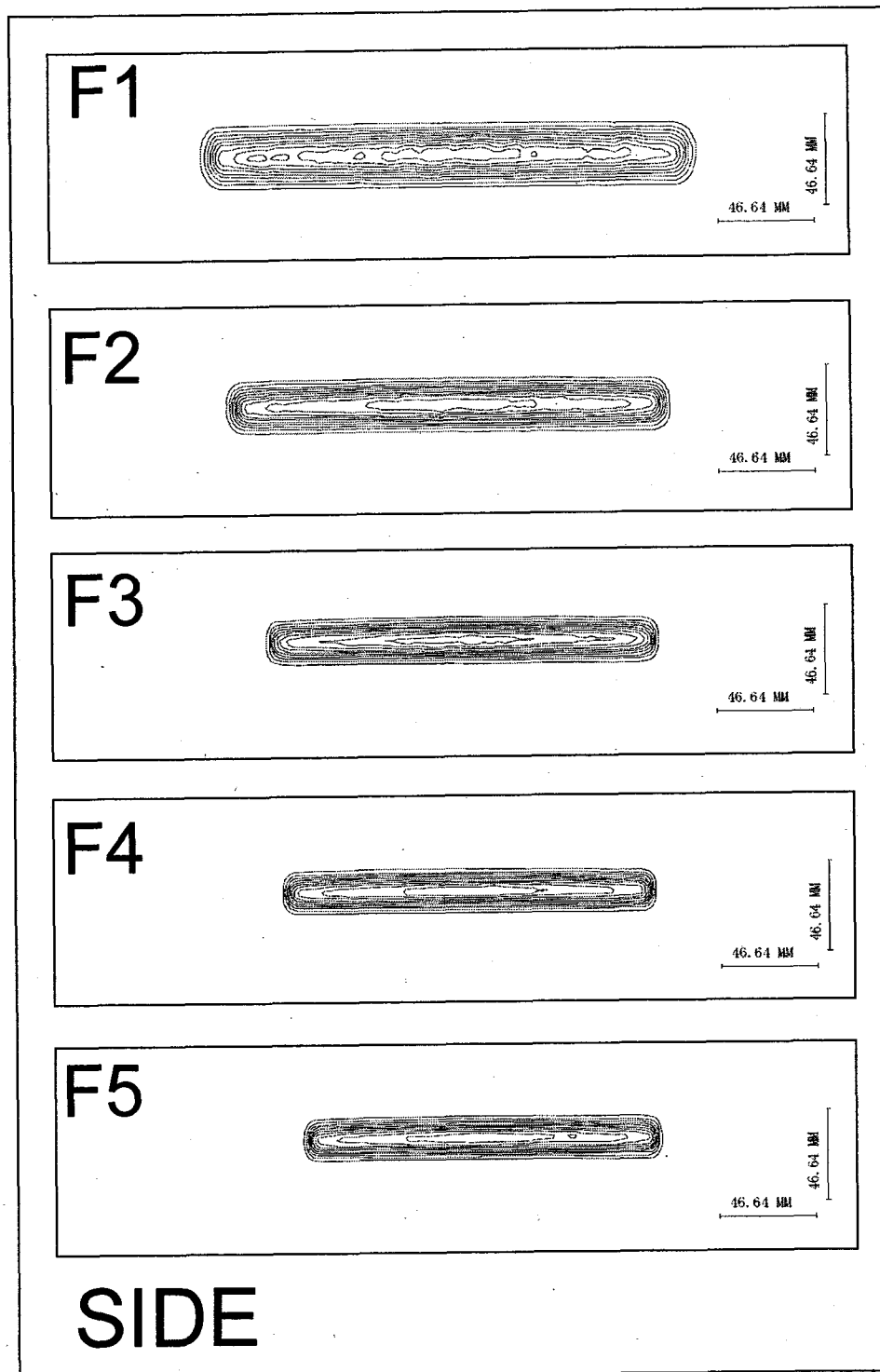
Fig. 2.2.3-4 Relative distributions of irradiances on the imaginary plane located near the dome for the side optics. (Contour)

X= 0. 000

Y= 0. 000

SURFACE   40

25. 0   MM

12-Jun-05
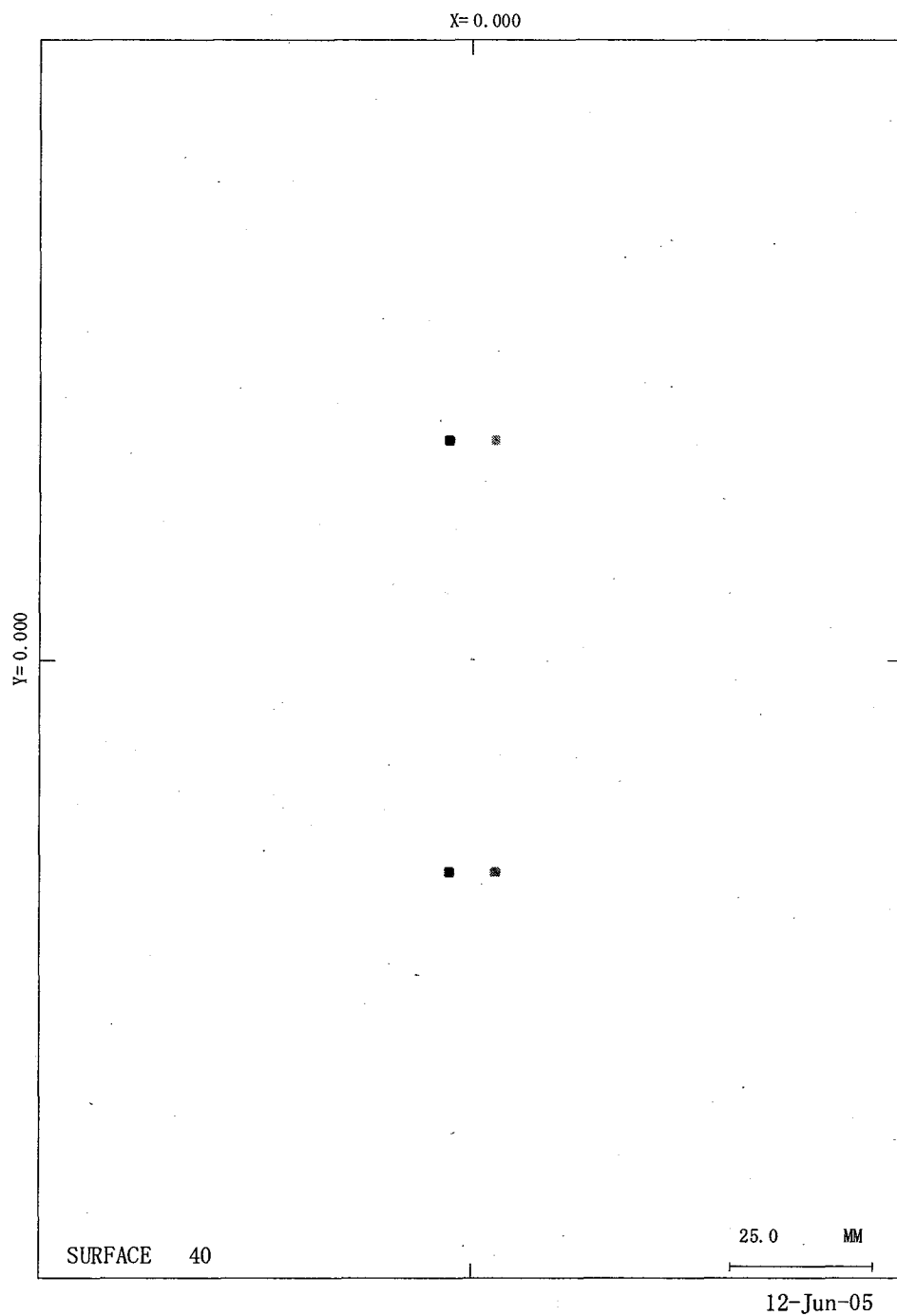
SIDE-2005footprint

Fig. 2.2.3-5 Footprints of the rays started from 4 corners of the micro lens array on the concave mirror
surfaces located near the divertor cassette for the side optics.

X= 0.000

Effective diameter (120 mm) of window

SURFACE   25

25.0   MM

12-Jun-05
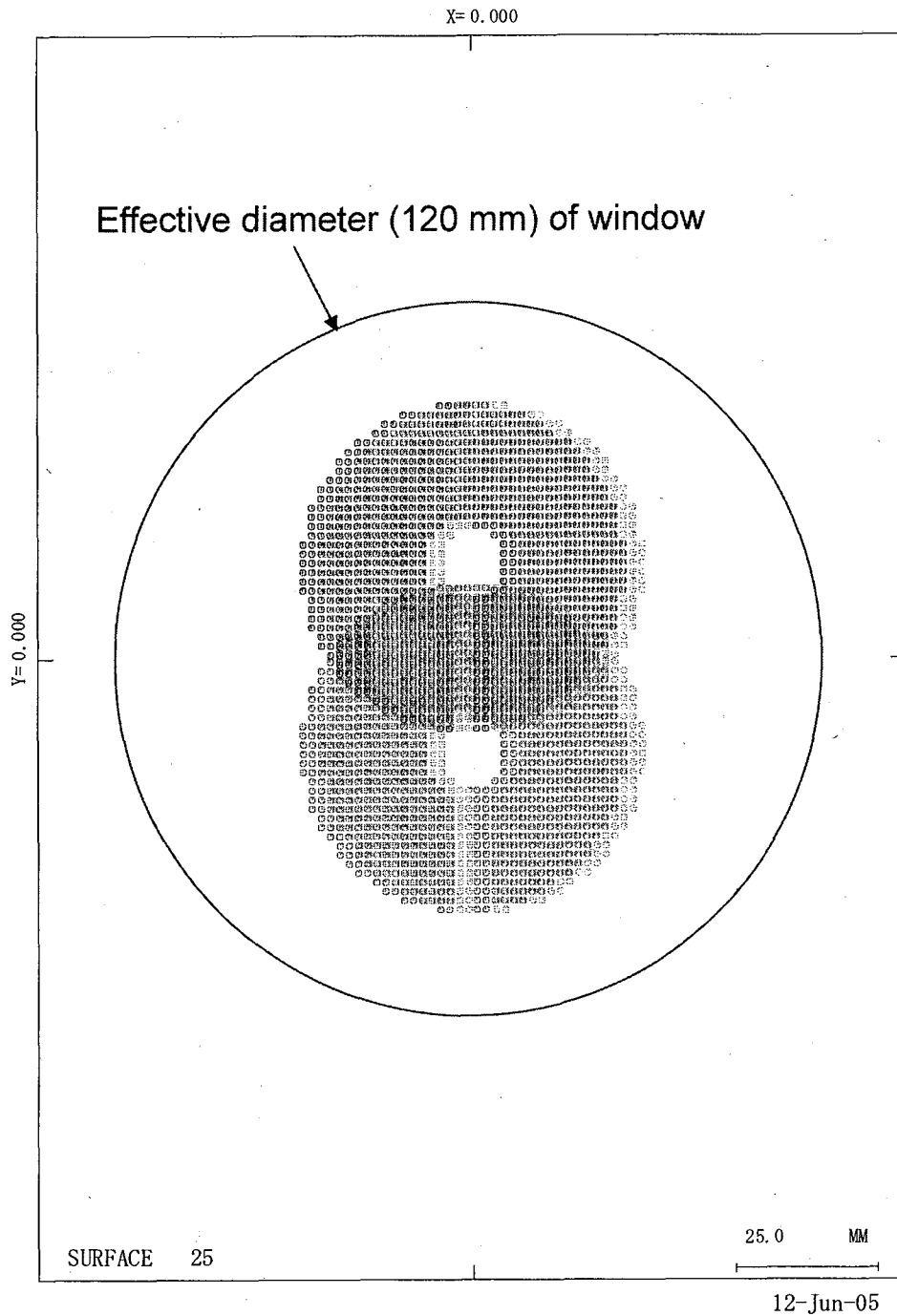
SIDE-2005footprint

Fig. 2.2.3-6 Footprints of the rays started from 4 corners of the micro lens array on the window for the side
optics.
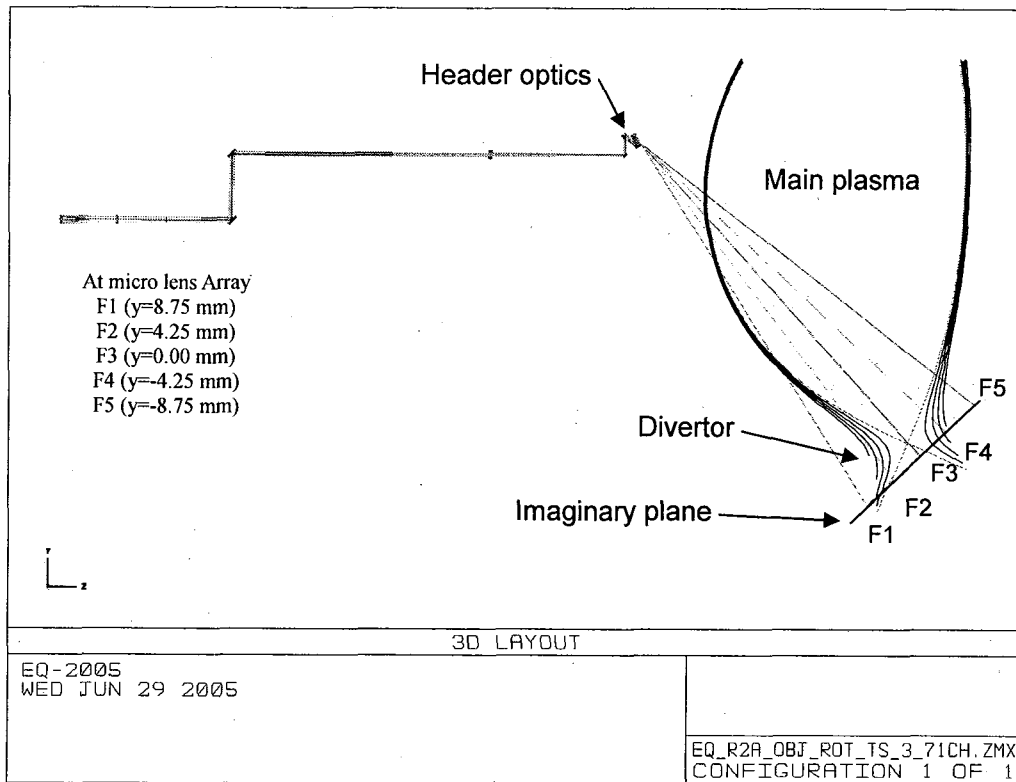
Fig. 2.3.2-1(a)   Traced rays for equatorial port optics with 71 channel micro lens array.
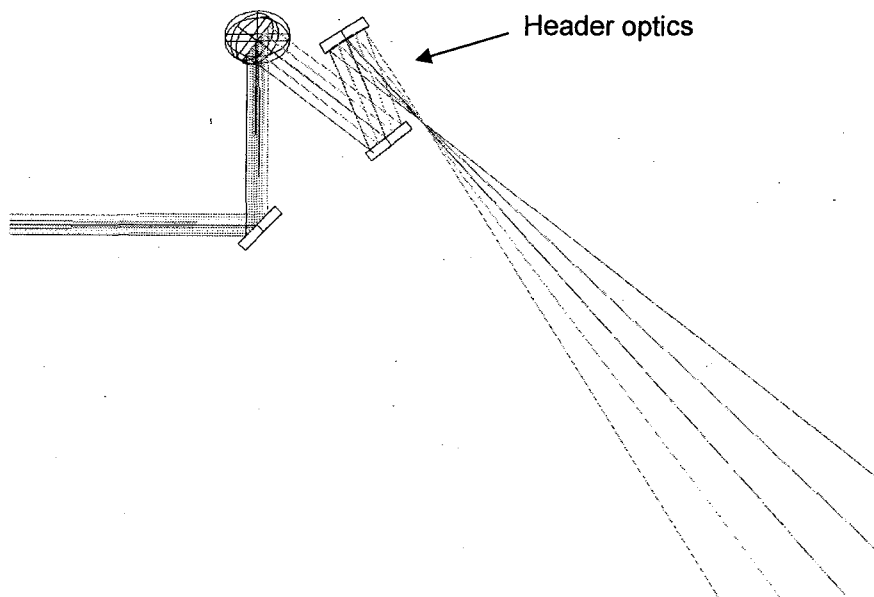
Fig. 2.3.2-1(b) Cross section view of traced rays in the header optics for equatorial port optics with 71 channel micro lens array.
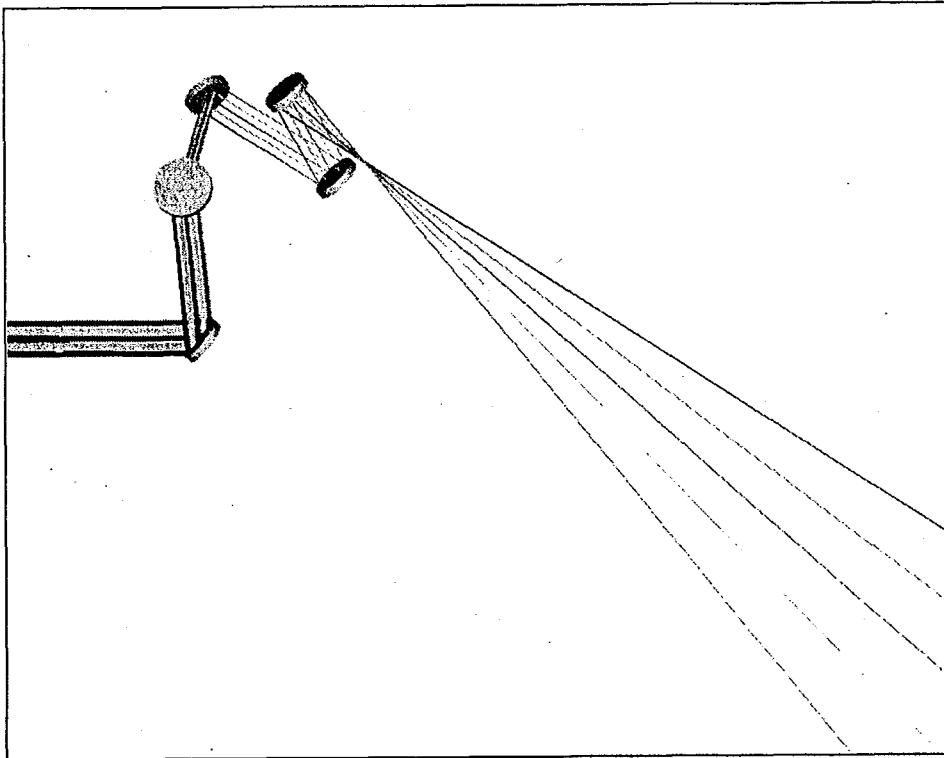
Fig. 2.3.2-2 Shaded view of mirror arrangement and traced rays in the header optics for equatorial port optics with 71 channel micro lens array.
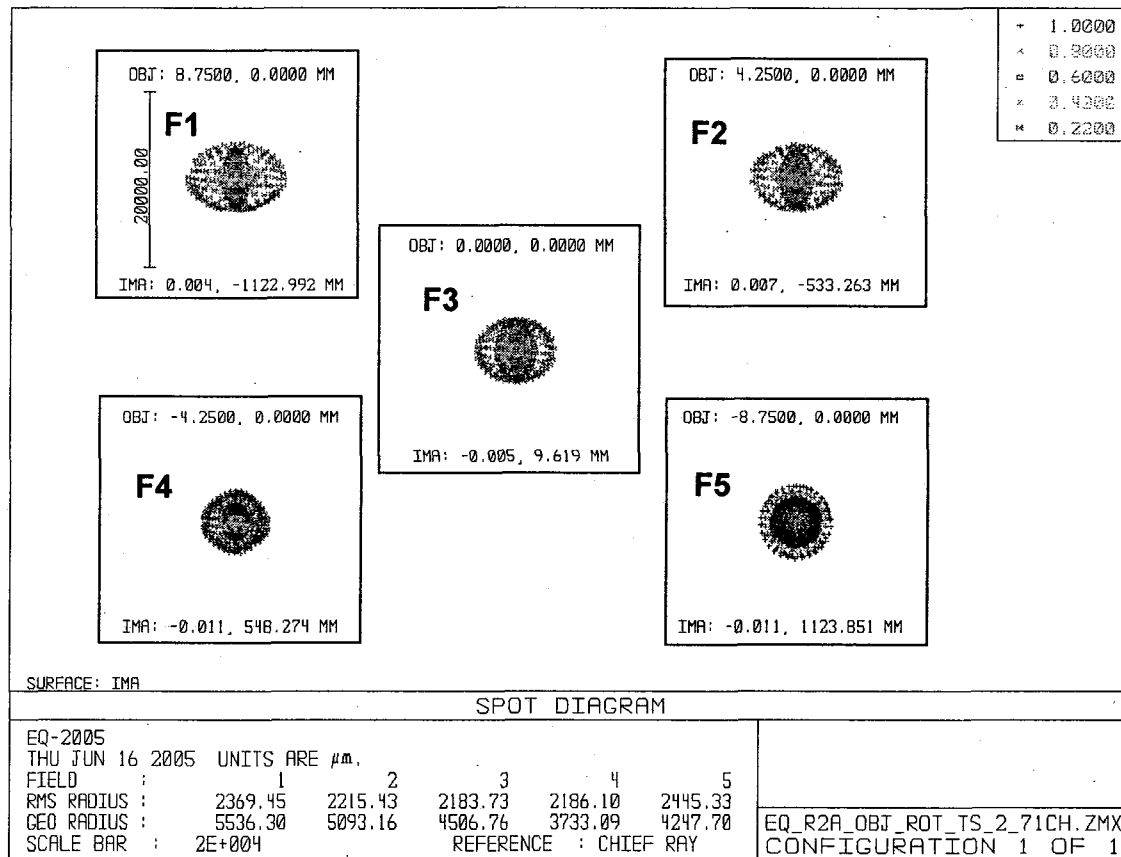
Fig. 2.3.2-3 Spot diagrams of F1, F2, F3, F4 and F5 for the equatorial port optics with 71 channel micro lens array.
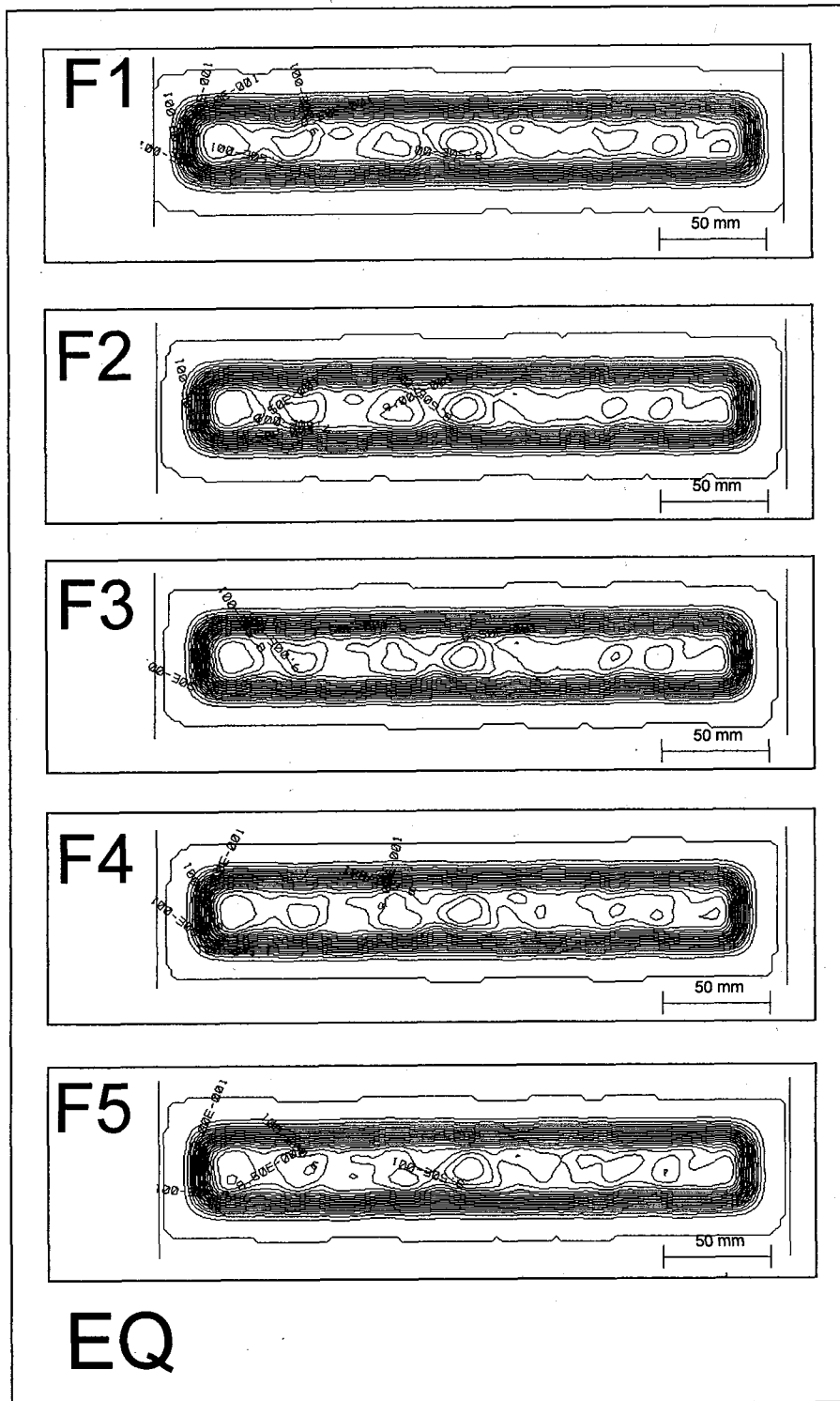
Fig. 2.3.2-4 Relative distributions of irradiances on the imaginary plane located near the dome for the equatorial port optics with 71 channel micro lens array (Contour). Calc. by ZEMAX.

X= 0.000

Y= 0.000

SURFACE   38

25.0   MM

12-Jun-05
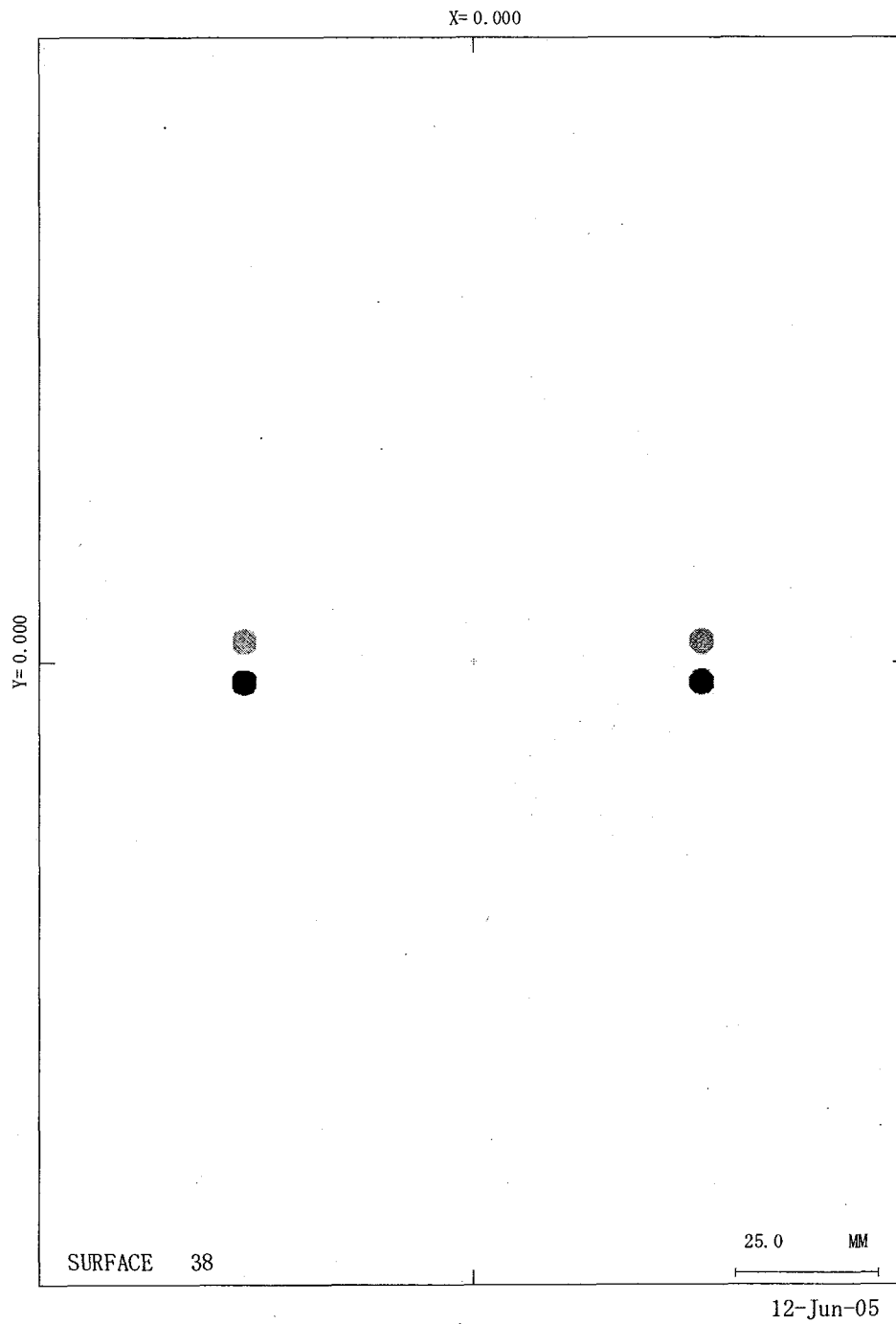
EQ-2005footprint

Fig. 2.3.2-5 Footprints of the rays started from 4 corners of the micro lens array on the concave mirror surfaces located in the header optics for the equatorial port optics.

X= 0.000

Effective diameter (120 mm) of window

Y= 0.000

25. 0   MM

SURFACE   25

12-Jun-05
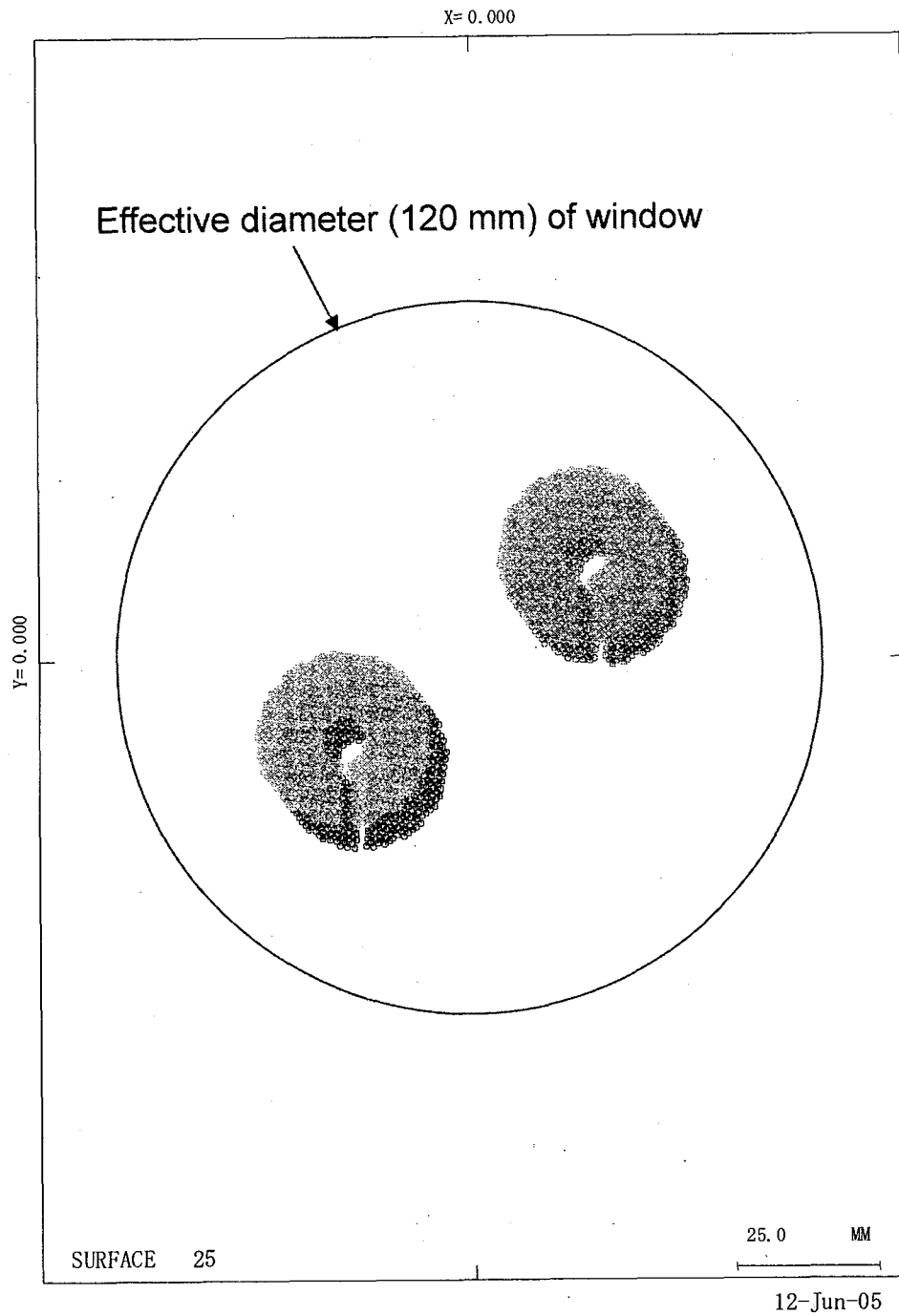
EQ-2005footprint

Fig. 2.3.2-6 Footprints of the rays started from 4 corners of the micro lens array on the window for the equatorial port optics.

At micro lens Array
F1 (y=8.75 mm)
F2 (y=4.25 mm)
F3 (y=0.00 mm)
F4 (y=-4.25 mm)
F5 (y=-8.75 mm)

Header optics

Main plasma

Divertor

Imaginary plane

F1 F2 F3 F4 F5

3D LAYOUT

UP-2005
THU JUN 16 2005

UP_RTS_NO DUMMY_2_71CH.ZMX
CONFIGURATION 1 OF 1
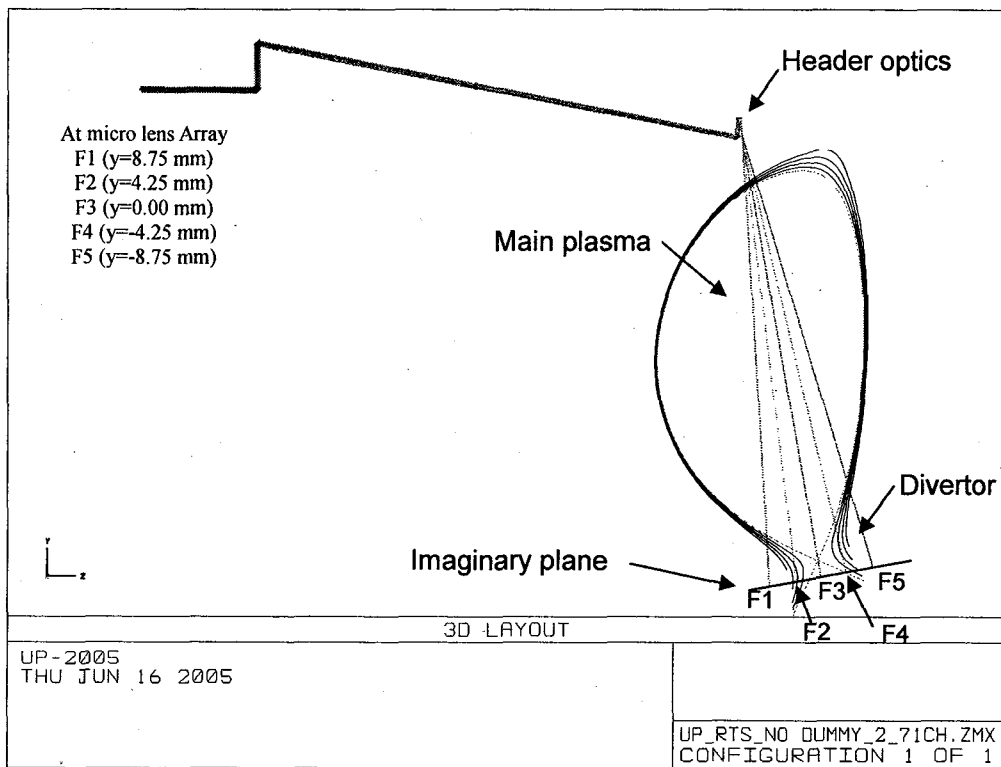
Fig. 2.3.3-1(a) Traced rays of the lines of sight (F1, F2, F3, F4 and F5) for upper port optics with 71 channel micro lens array.
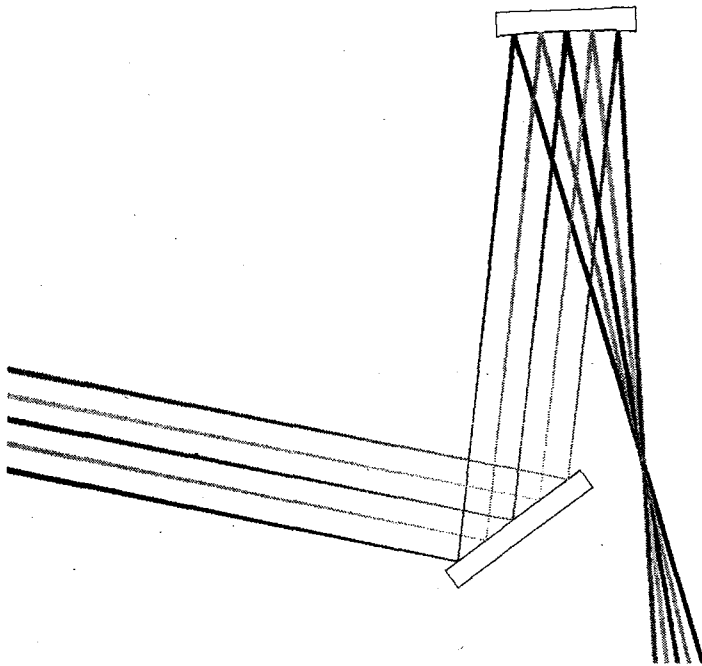
Fig. 2.3.3-1(b) Cross section view of traced rays in the header optics for upper port optics with 71 channel micro lens array.
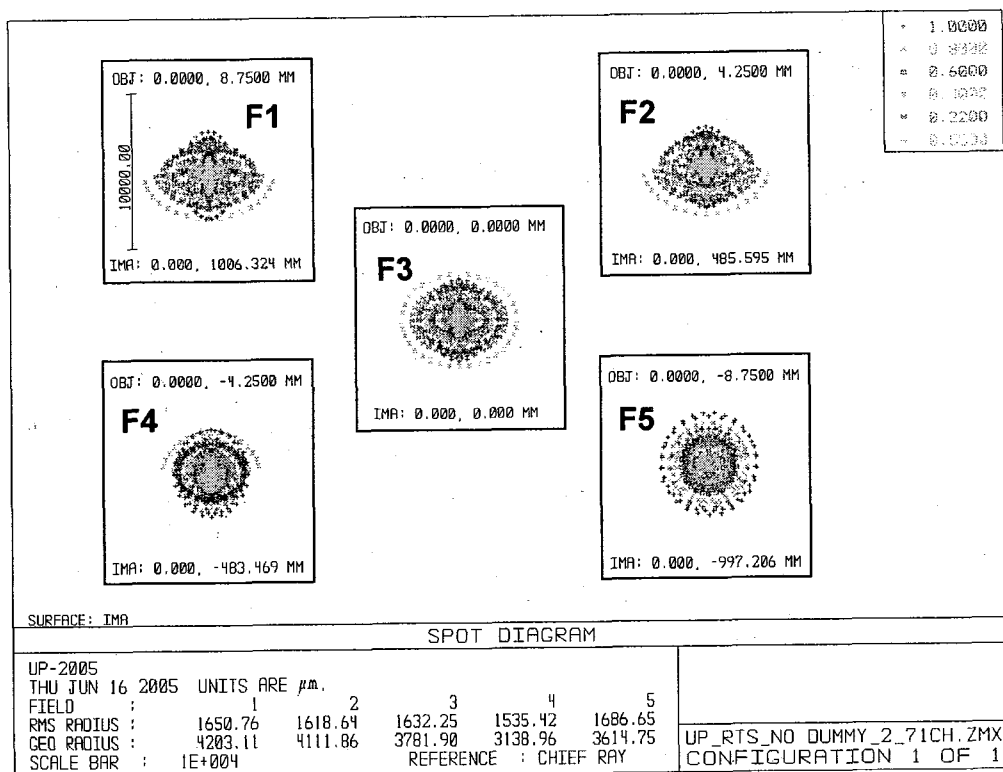
Fig. 2.3.3-2 Spot diagrams for the upper port optics with 71 channel micro lens array.
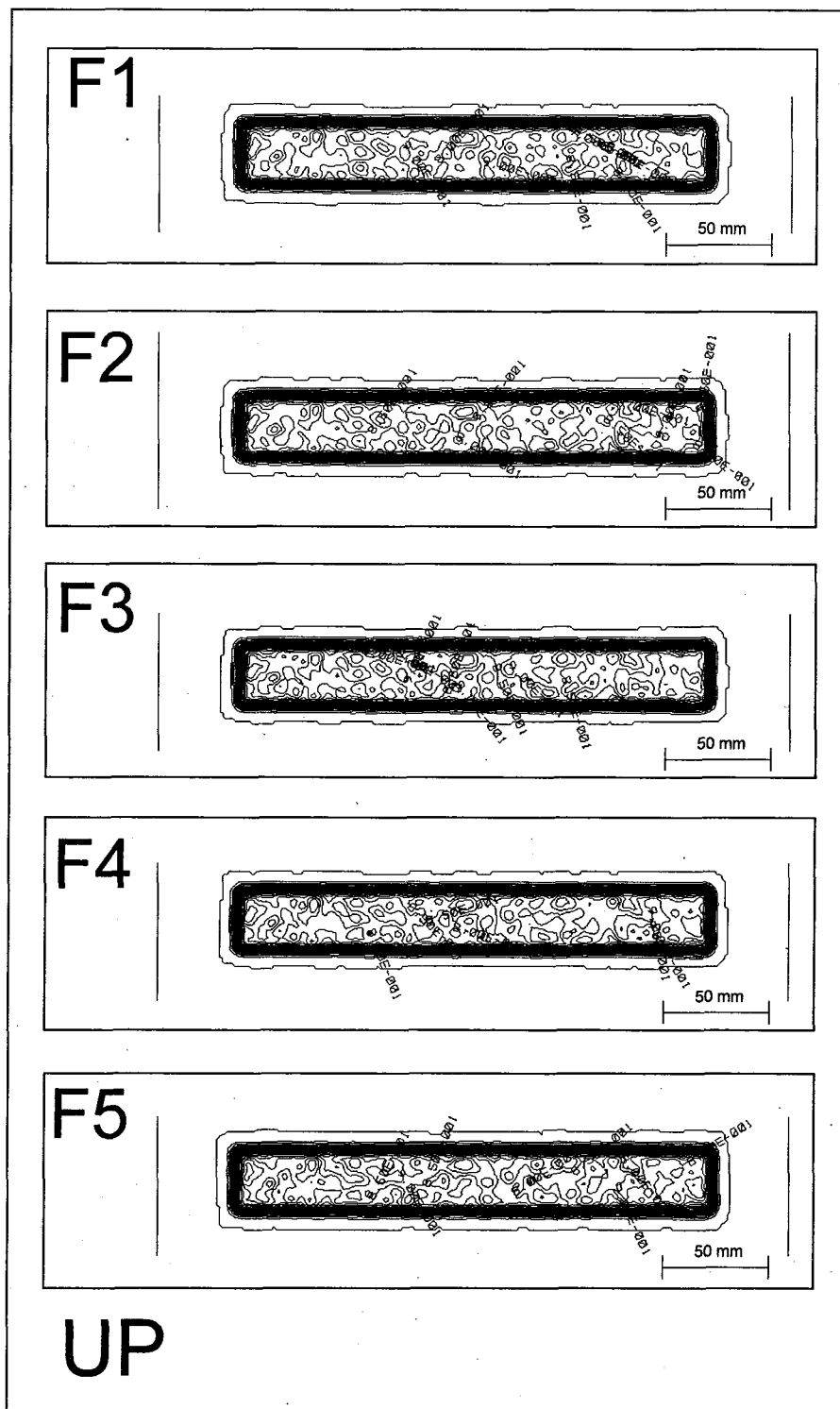
Fig. 2.3.3-3 Relative distributions of irradiances on the imaginary plane located near the dome for the upper
port optics with 71 channel micro lens array (Contour). Calc. by ZEMAX.
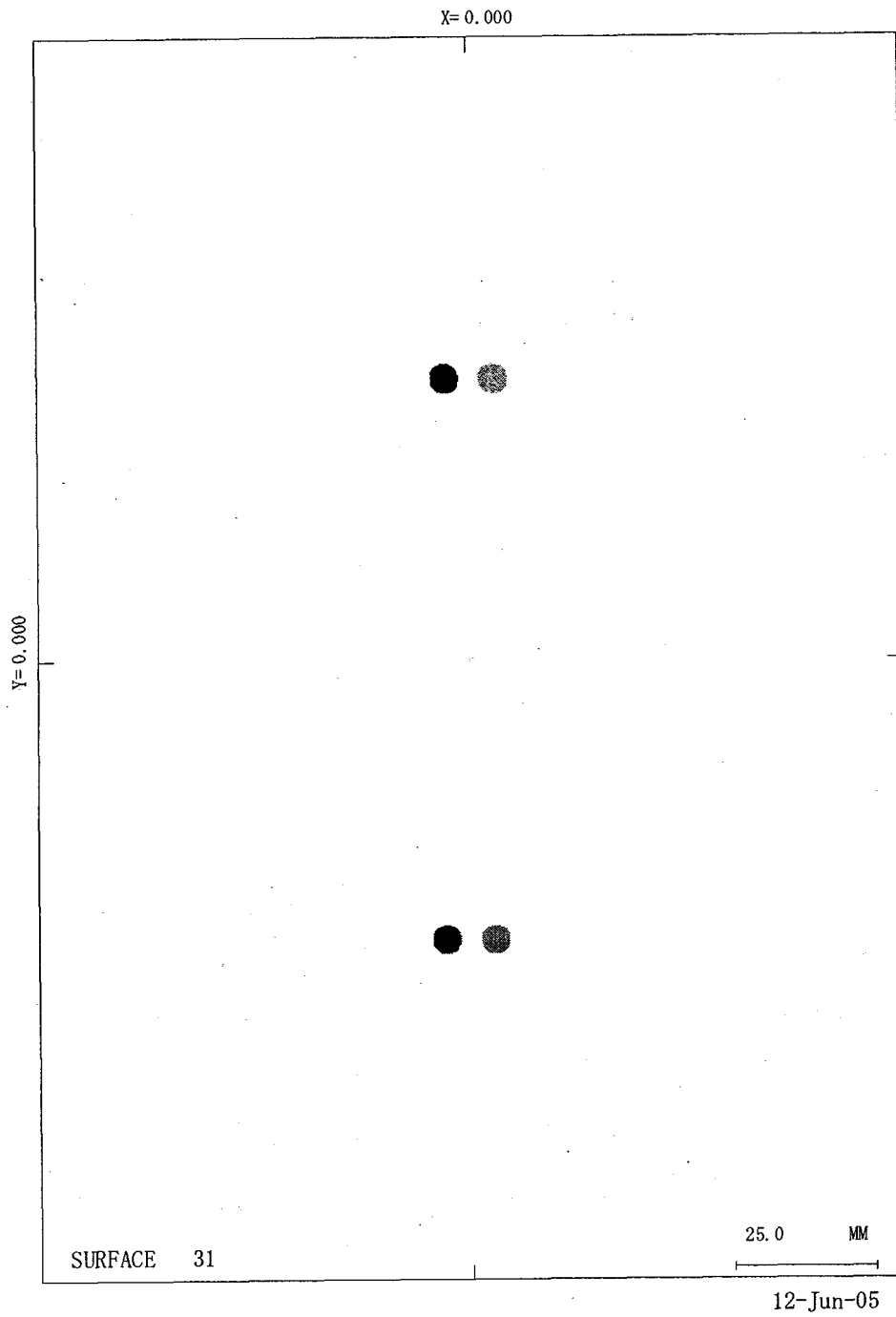
Fig. 2.3.3-4 Footprints of the rays started from 4 corners of the micro lens array on the concave mirror surfaces located in the header optics for the upper port optics.

X= 0.000

Effective diameter (120 mm) of window

SURFACE   25

25.0   MM

12-Jun-05
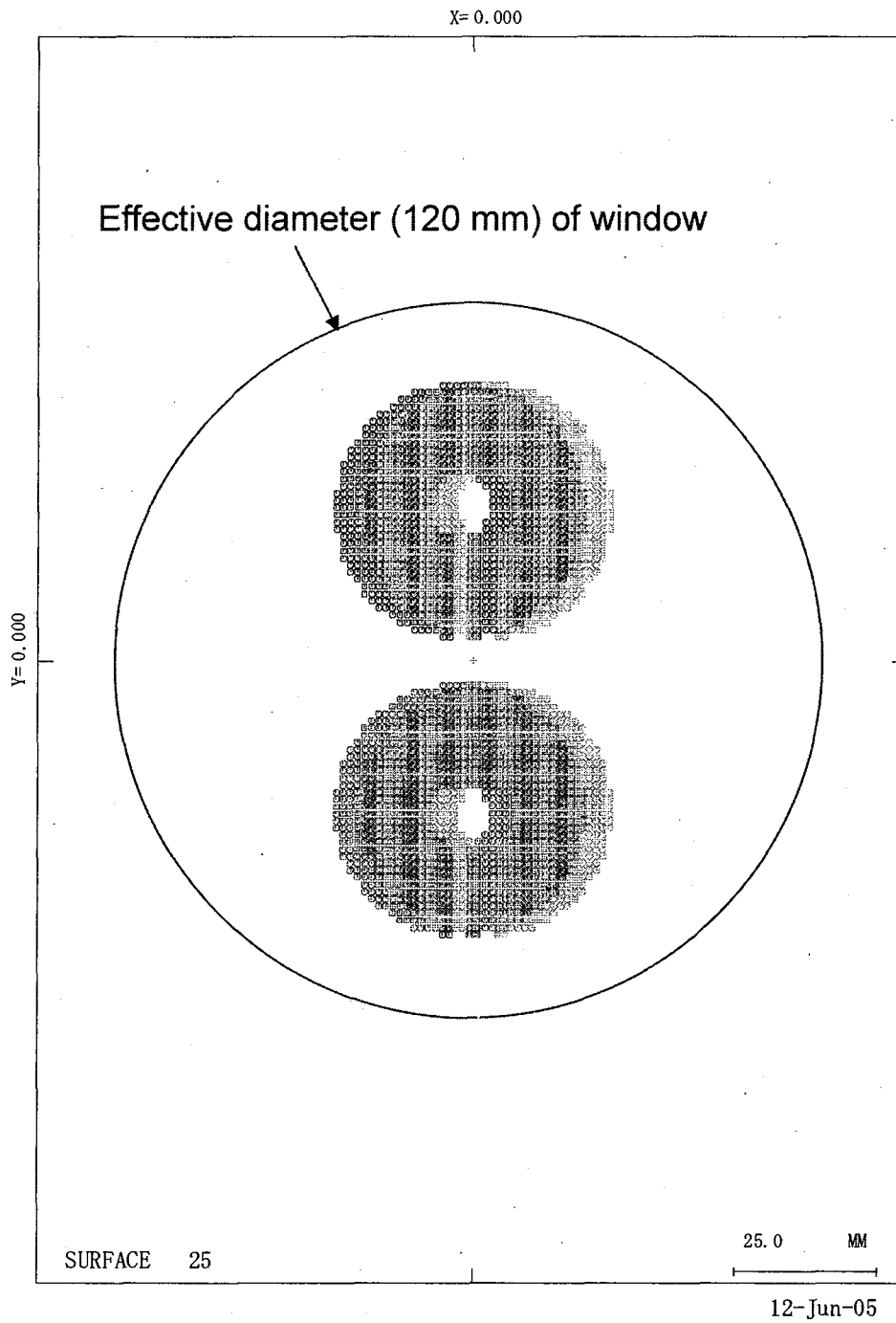
UP-2005footprint

Fig. 2.3.3-5 Footprints of the rays started from 4 corners of the micro lens array on the window for the upper port optics.
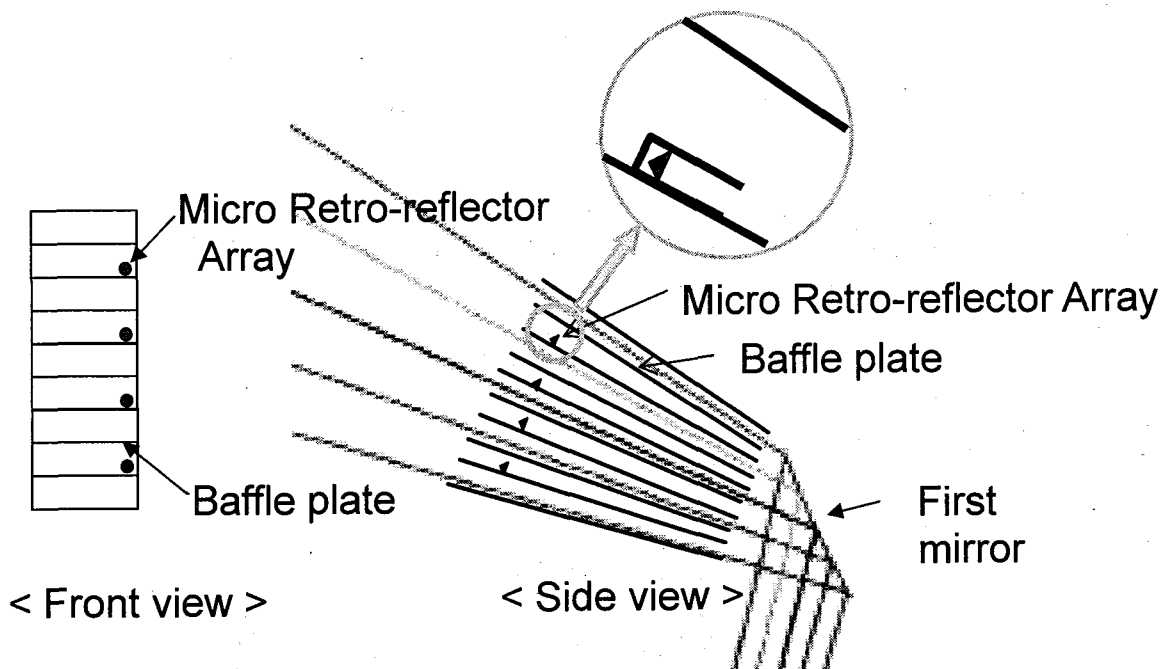
Fig. 2.5.1-1(a) Micro retro-reflectors are installed between the baffle plates for in-situ calibration.
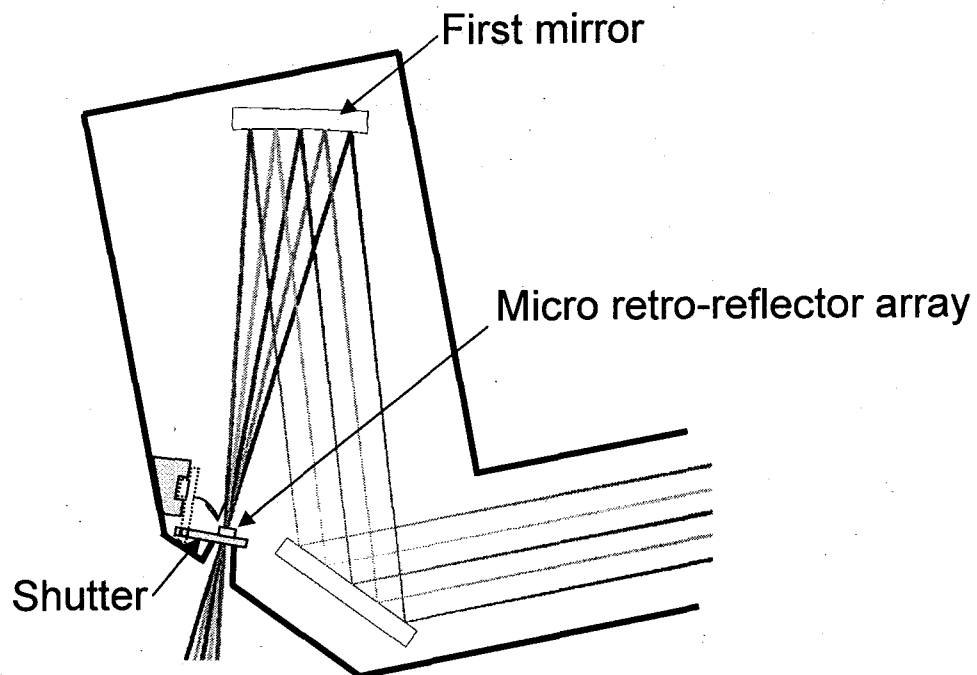
Fig. 2.5.1-1(b) Micro retro-reflector is installed is installed on the shutter. The micro retro-reflector is moved in front of the first mirror during the calibration.
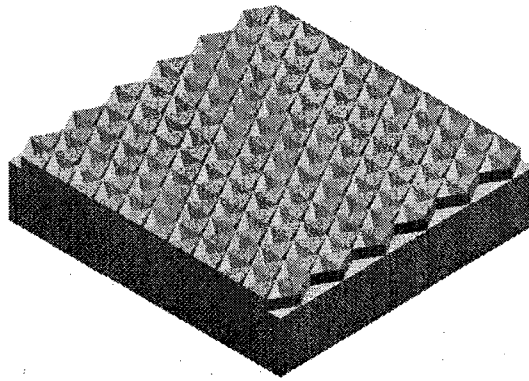
Fig. 2.5.1-2 Micro retro-reflector array.
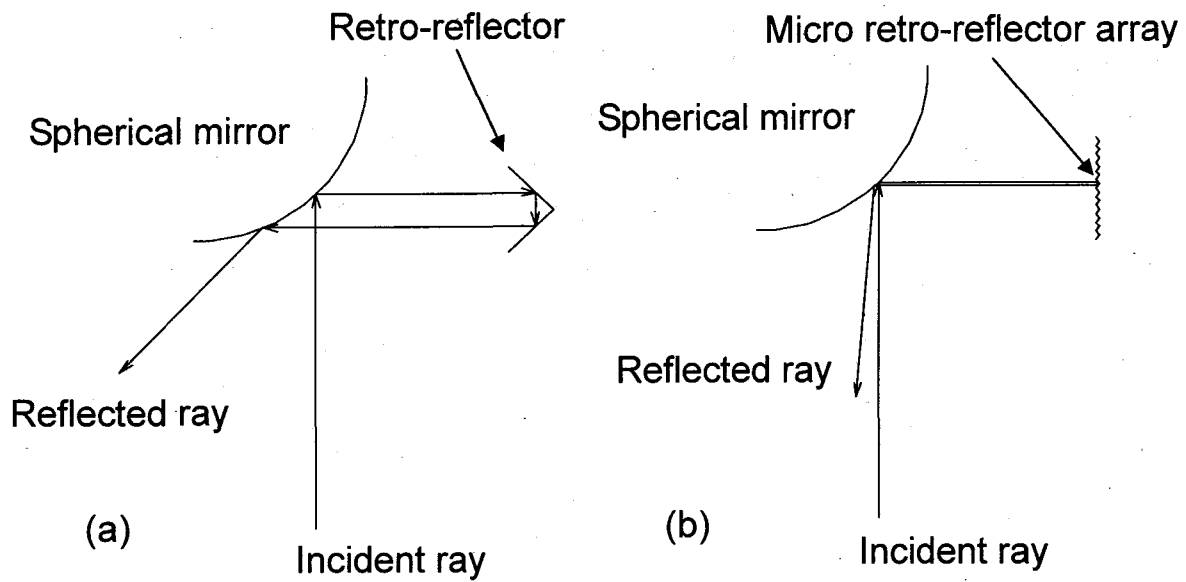
Fig. 2.5.1-3 (a) Almost incident light does not go back to the emission point. (b) Almost incident light go back to the emission point.
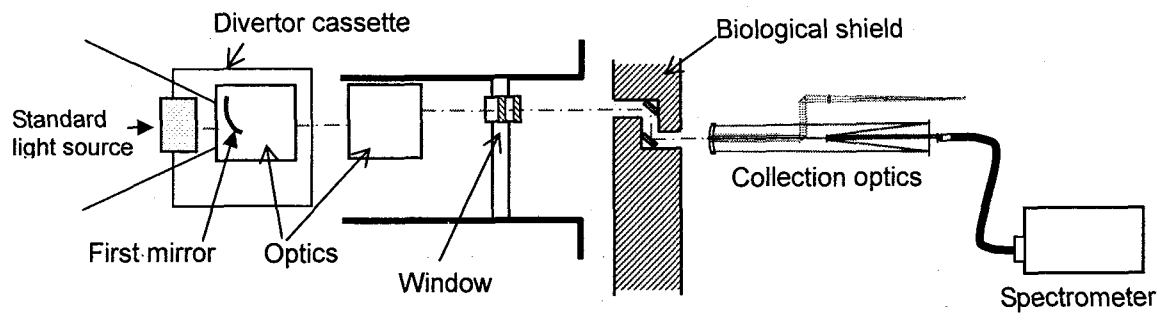
Fig. 2.5.1-4(a) For optics of divertor port: During the installation phase, sensitivity calibration should be carried out by standard light sources set in the divertor cassette.
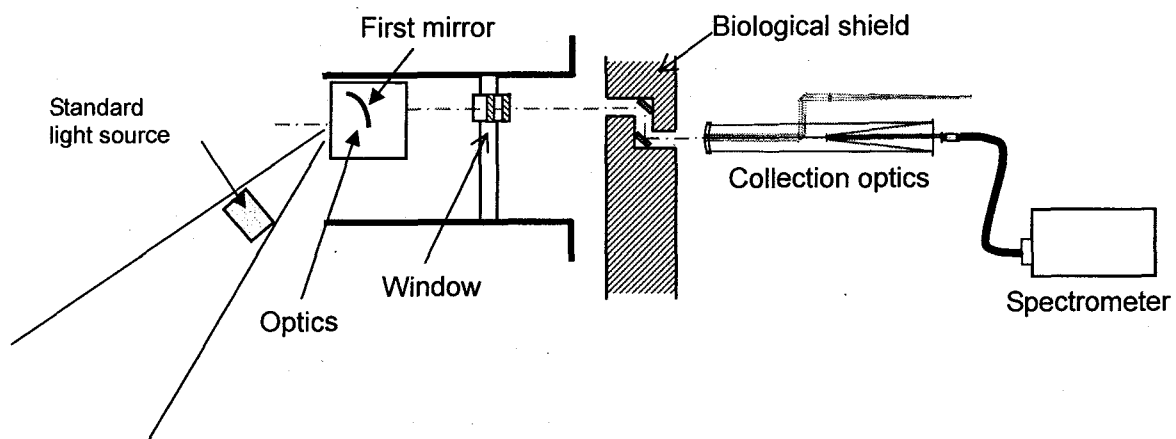
Fig. 2.5.1-4(b) For optics of upper and equatorial port: During the installation phase, sensitivity calibration should be carried out by standard light sources set in front of the first mirror.
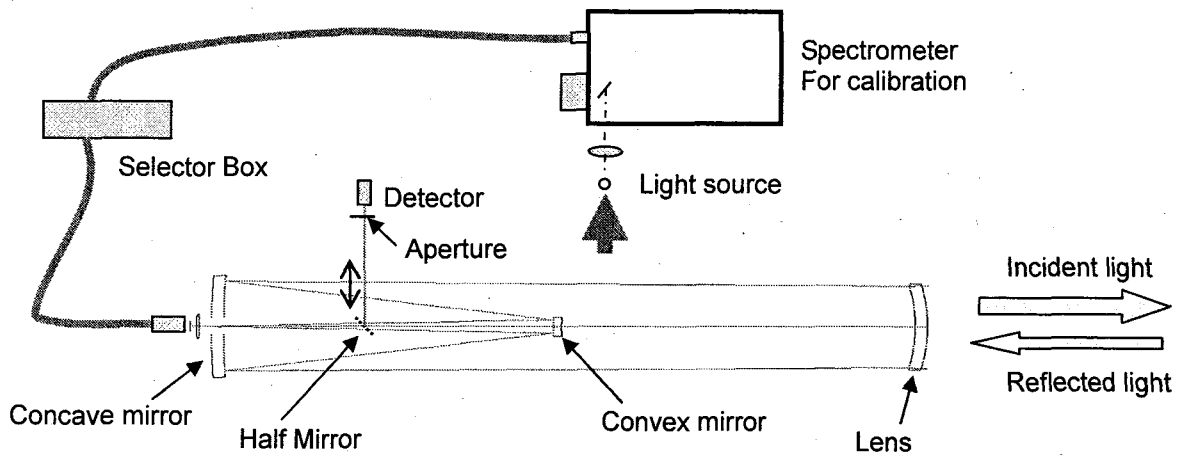
Fig. 2.5.1-5(a) Light is introduced from the exit slit of a dedicated spectrometer for calibration.
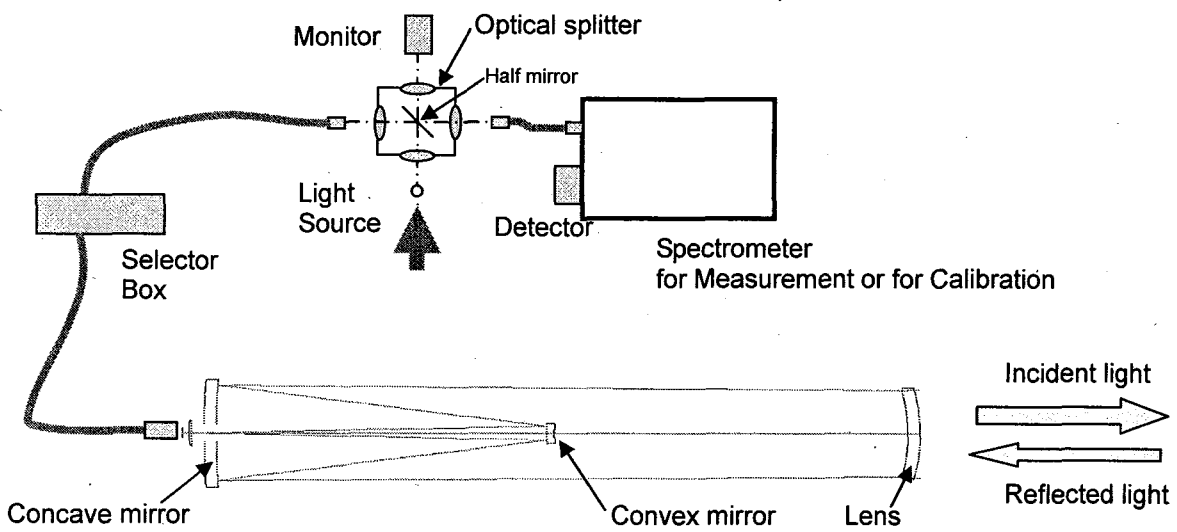
Fig. 2.5.1-5(b) Light is introduced to an optical fiber by an optical splitter located between the spectrometer.
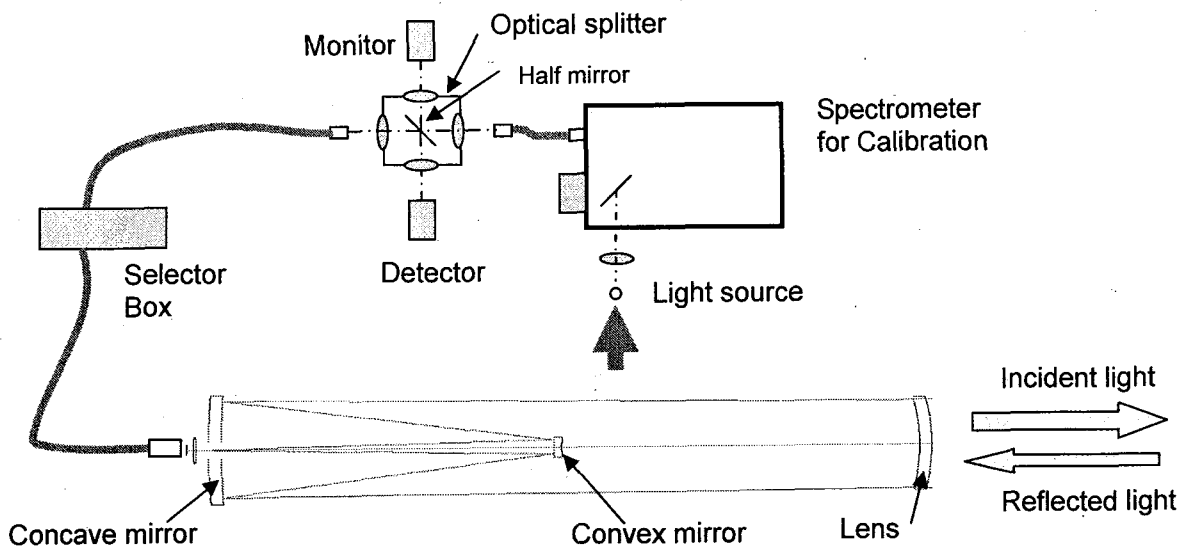
Fig. 2.5.1-5(c) Light is introduced from the exit slit of a dedicated spectrometer for calibration.
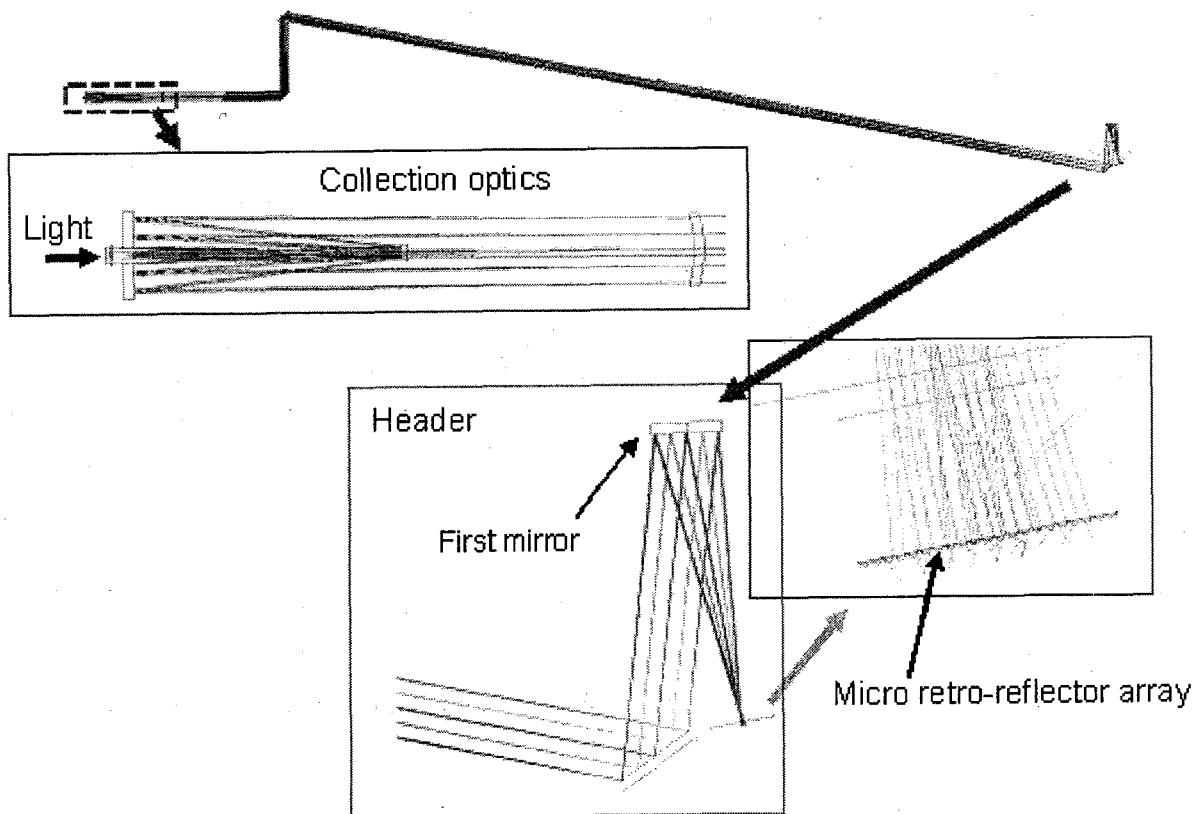
Fig. 2.5.2-1 Optics and ray trace for in-situ calibration system of the upper port optics.
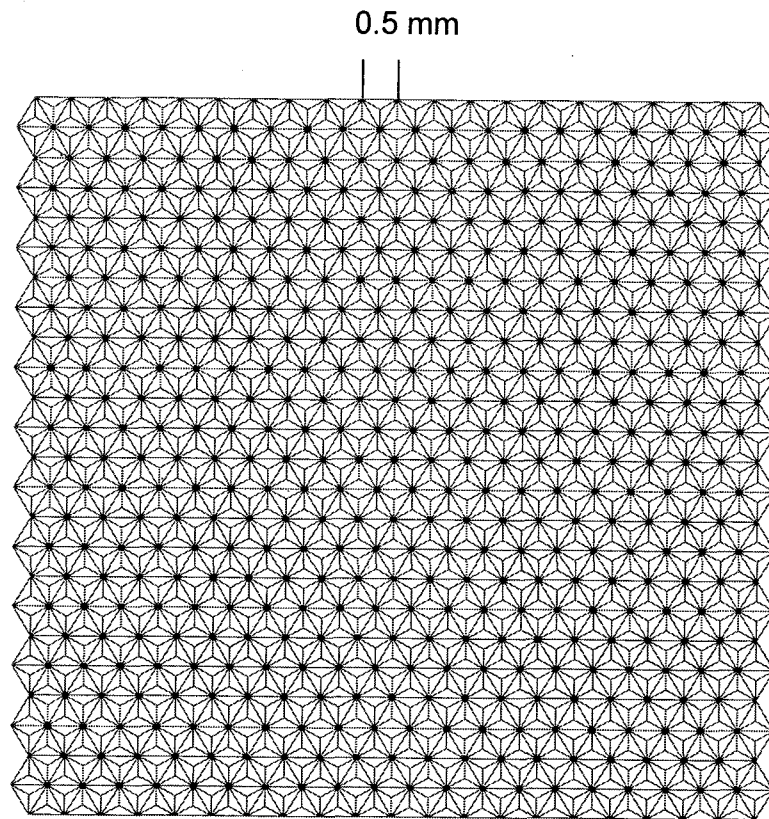
0.5 mm

Fig. 2.5.2-2 Plan view of micro retro-reflector array composed of small retro-reflector with an equilateral
triangle 0.5 mm on a side.

Field 1

Field 2

Field 3

Field 4

Field 5

SURFACE: IMA

FULL FIELD SPOT DIAGRAM

UP-2205
SAT JUN 11 2005　UNITS ARE μm.
FIELD　　　　　　　　　　　ALL
RMS RADIUS :　　　7943.08
GEO RADIUS :　　　1.1E+004
SCALE BAR　:　　4E+004　　　　　REFERENCE　: CHIEF RAY

CALIB_UP_M3_B.ZMX
CONFIGURATION 1 OF 1
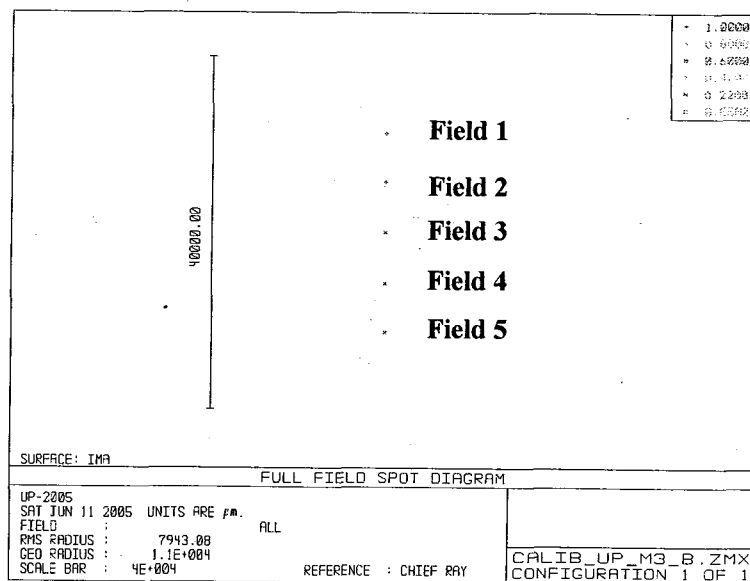
Fig. 2.5.2-3 Spot diagram of returned rays on the image surface (surface of the micro lens array).
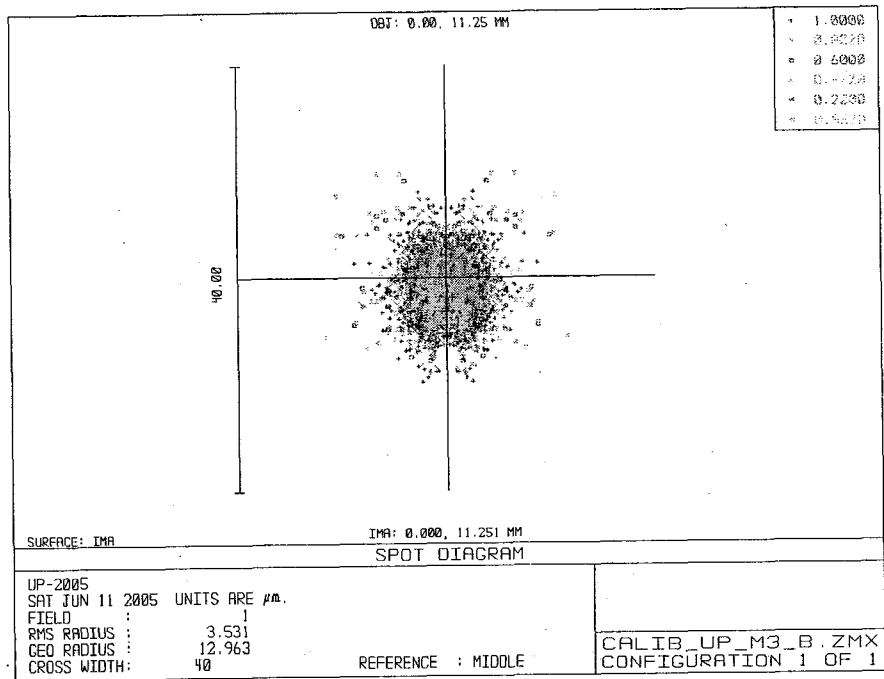
Fig. 2.5.2-4(a) Spot diagram of returned rays of field 1 (0 mm, 11.25 mm) on the image surface.
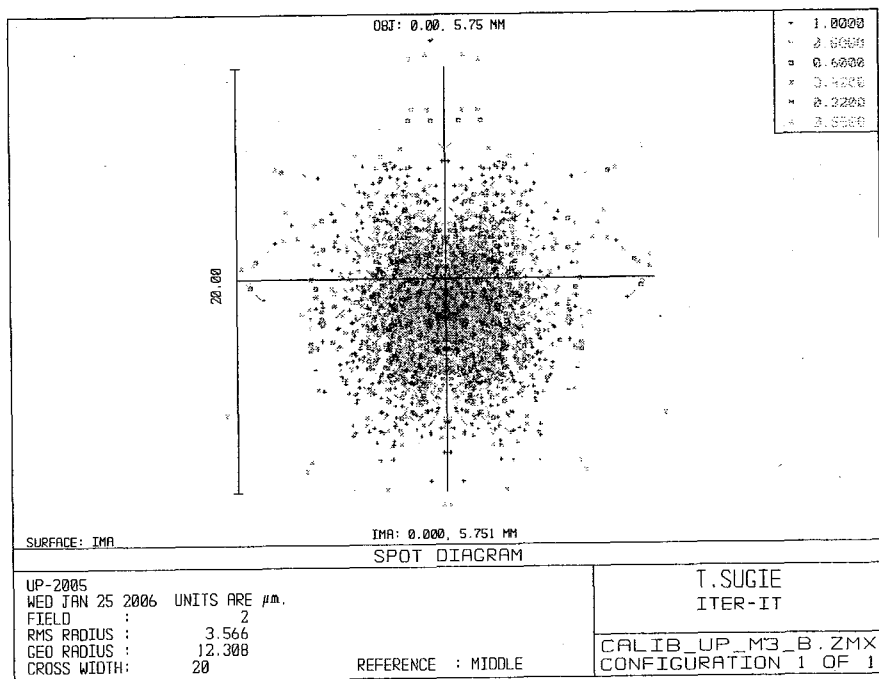
Fig. 2.5.2-4(b) Spot diagram of returned rays of field 2 (0 mm, 5.75 mm) on the image surface.
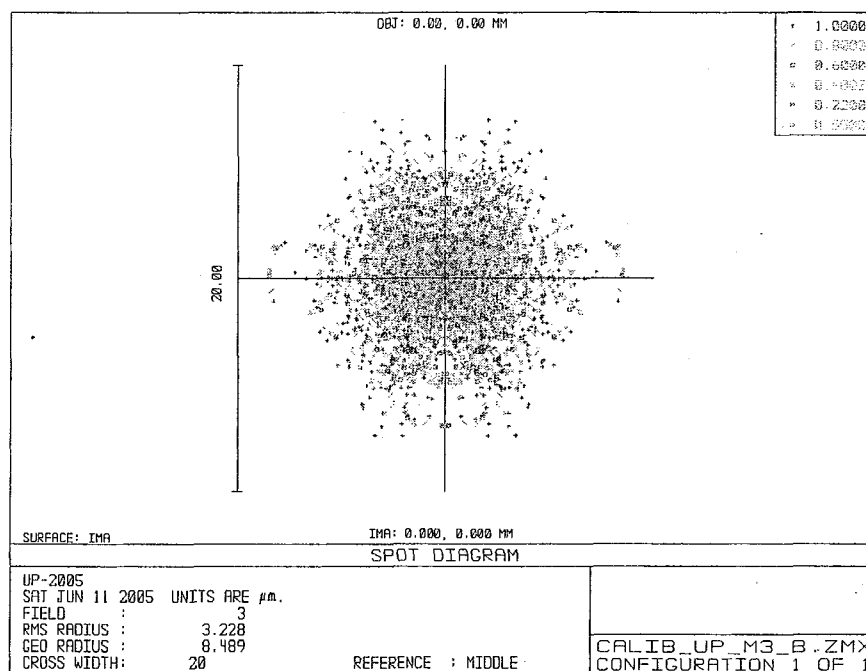
Fig. 2.5.2-4(c) Spot diagram of returned rays of field 3 (0 mm, 0 mm) on the image surface.
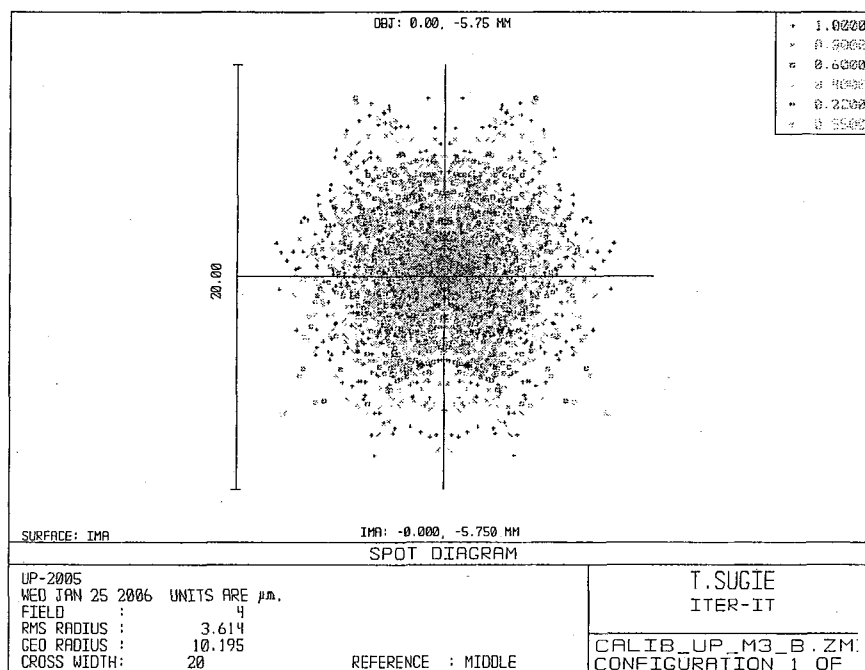
Fig. 2.5.2-4(d) Spot diagram of returned rays of field 4 (0 mm, -5.75 mm) on the image surface.
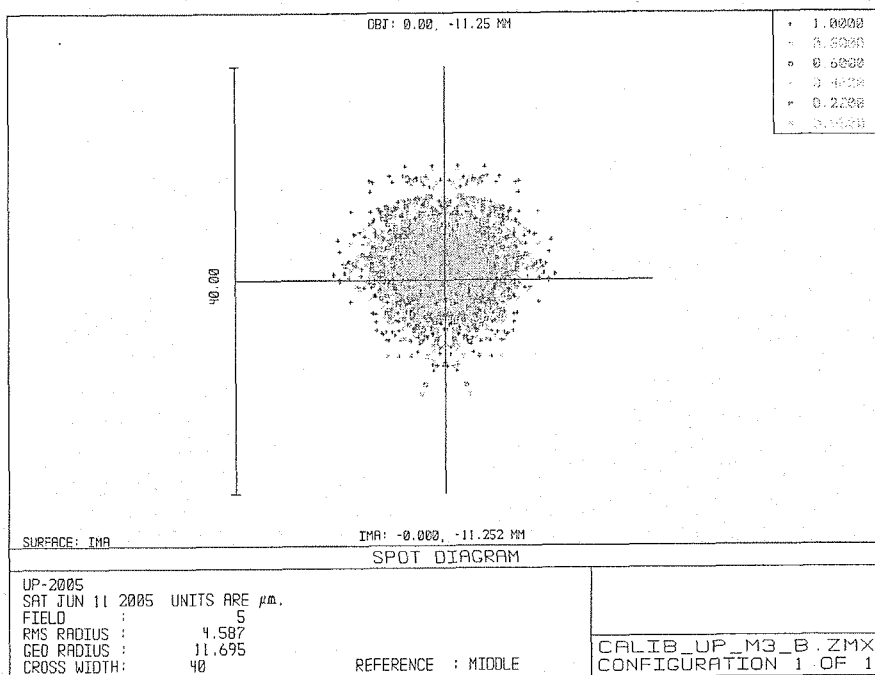
Fig. 2.5.2-4(e) Spot diagram of returned rays of field 5 (0 mm, -11.25 mm) on the image surface.
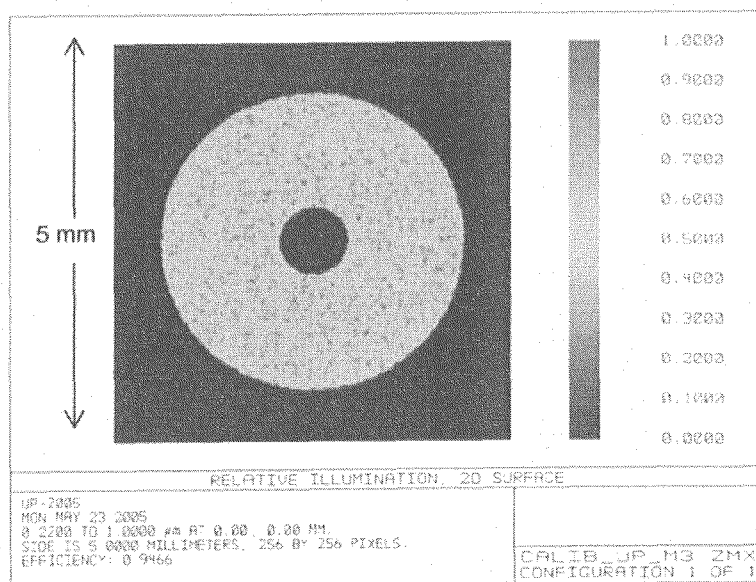
Fig. 2.5.2-5 Irradiance of the light source on the micro retro-reflector array. The light source (2.0 mm x 0.25 mm) is located at the field 3 (0, 0) on the micro lens array. In this case, the micro retro-reflector array of the size 1cm x 1 cm is sufficient.
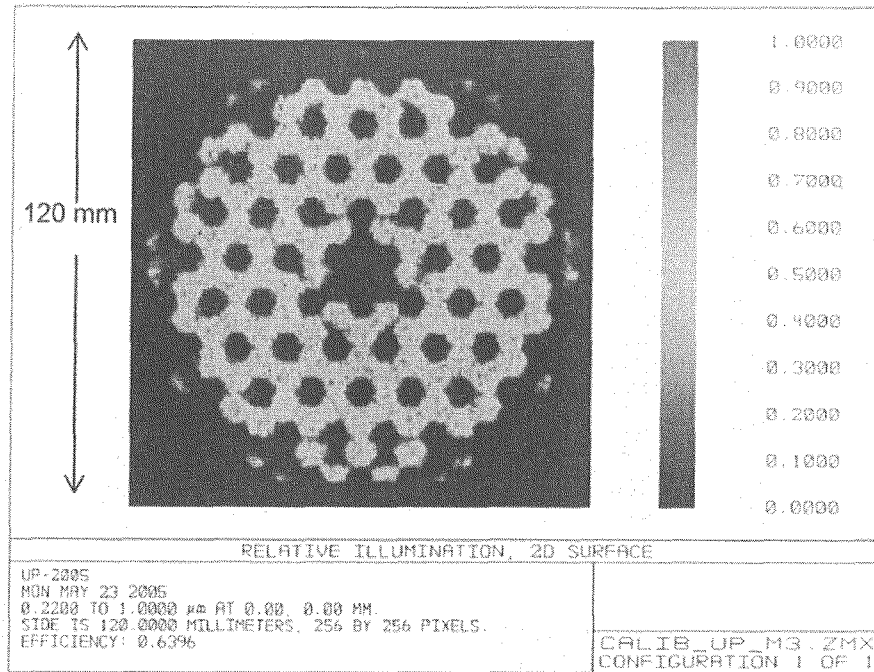
Fig. 2.5.2-6 Irradiance of the light source located at the field 3 (0, 0) on the collection lens.   In this case, almost light back in to the collection lens with the diameter of 110 mm.
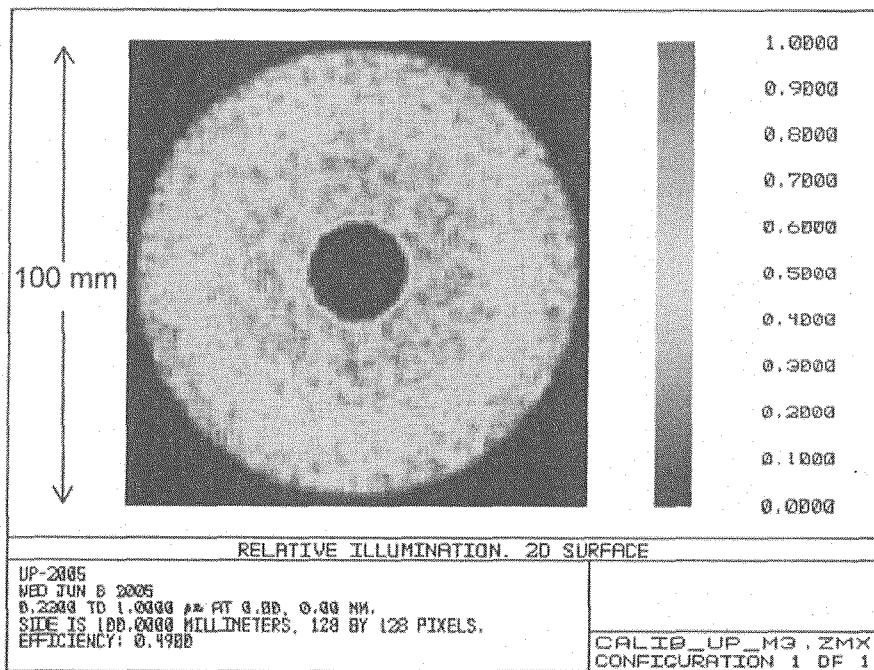
Fig. 2.5.2-7 Irradiance of the light source located at the field 3 (0, 0) on the collection lens. In order to confirm the hexagonal pattern is caused by the plasma facing spherical first mirror, the ray trace was carried out by changing the spherical mirror to plane mirror.

RELATIVE ILLUMINATION, 2D SURFACE

UP-2005
MON MAY 23 2005
0.2200 TO 1.0000 μm AT 0.00, 0.00 MM.
SIDE IS 3.0000 MILLIMETERS, 256 BY 256 PIXELS.
EFFICIENCY: 0.6135

CALIB_UP_M3.ZMX
CONFIGURATION 1 OF 1
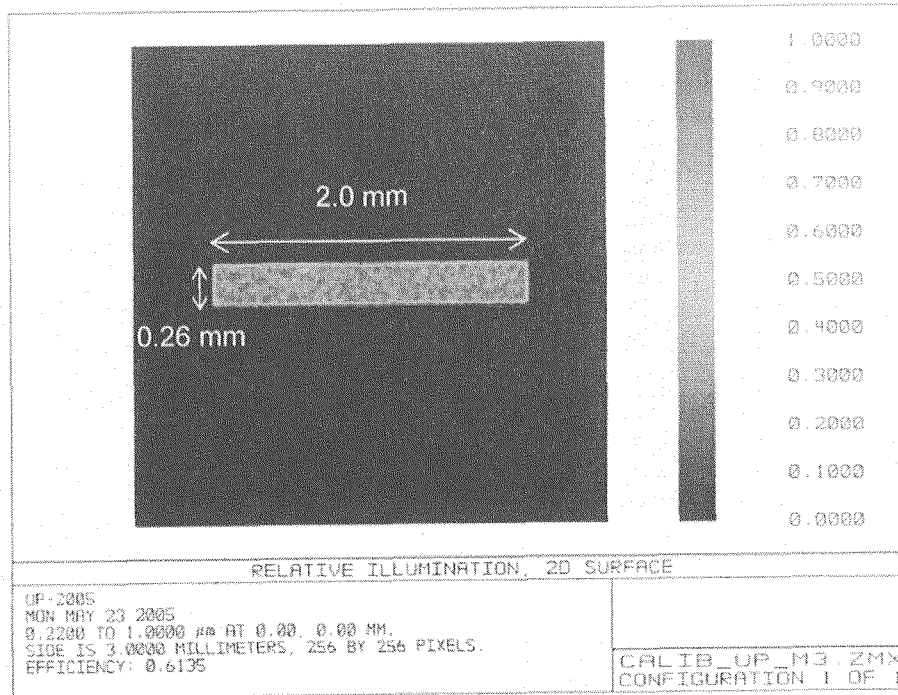
Fig. 2.5.2-8 Irradiance of the light source located at the field 3 (0, 0) on the image surface (surface of the micro lens array).
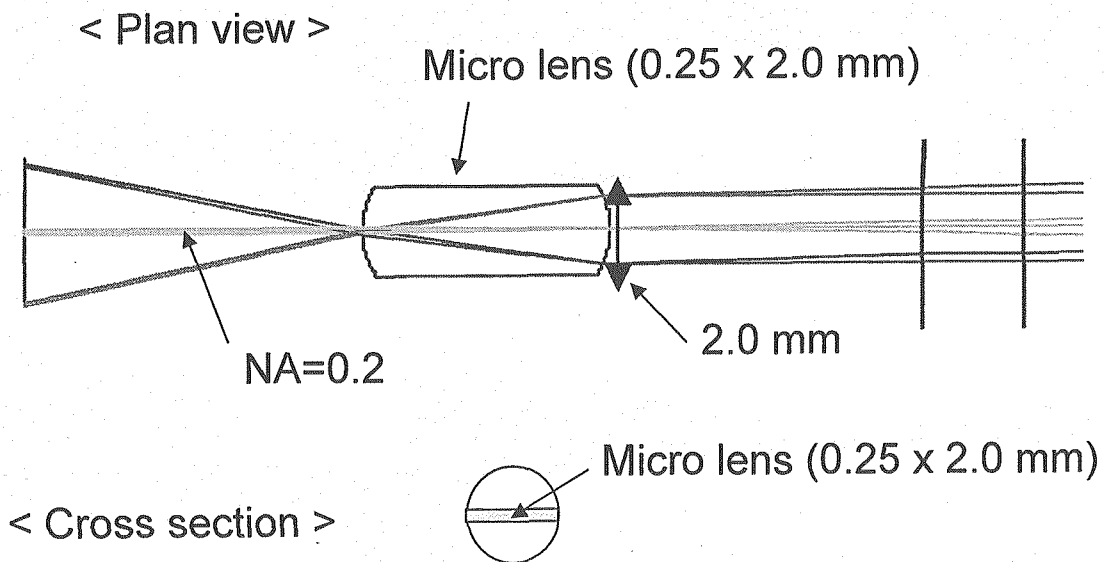
Fig. 2.5.3-1 Micro lens and the geometric aspect. The light from the optical fiber with the NA=0.2 enter the micro lens and (0.25 × 2.0)/π of the incident light is emitted from the micro lens to the collection optics.
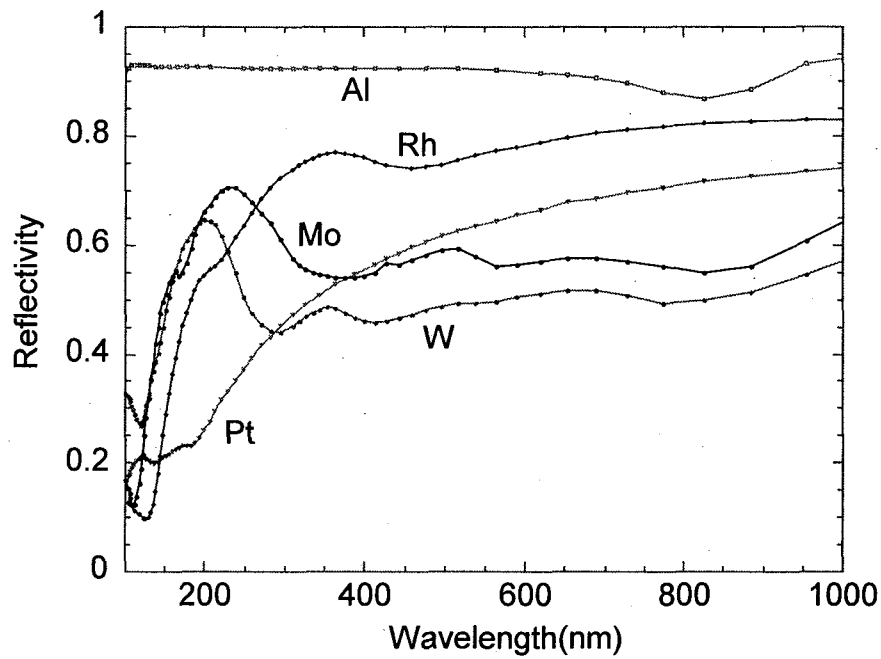
Fig. 2.5.3-2 Reflectivities of mirror materials as a function of wavelength.
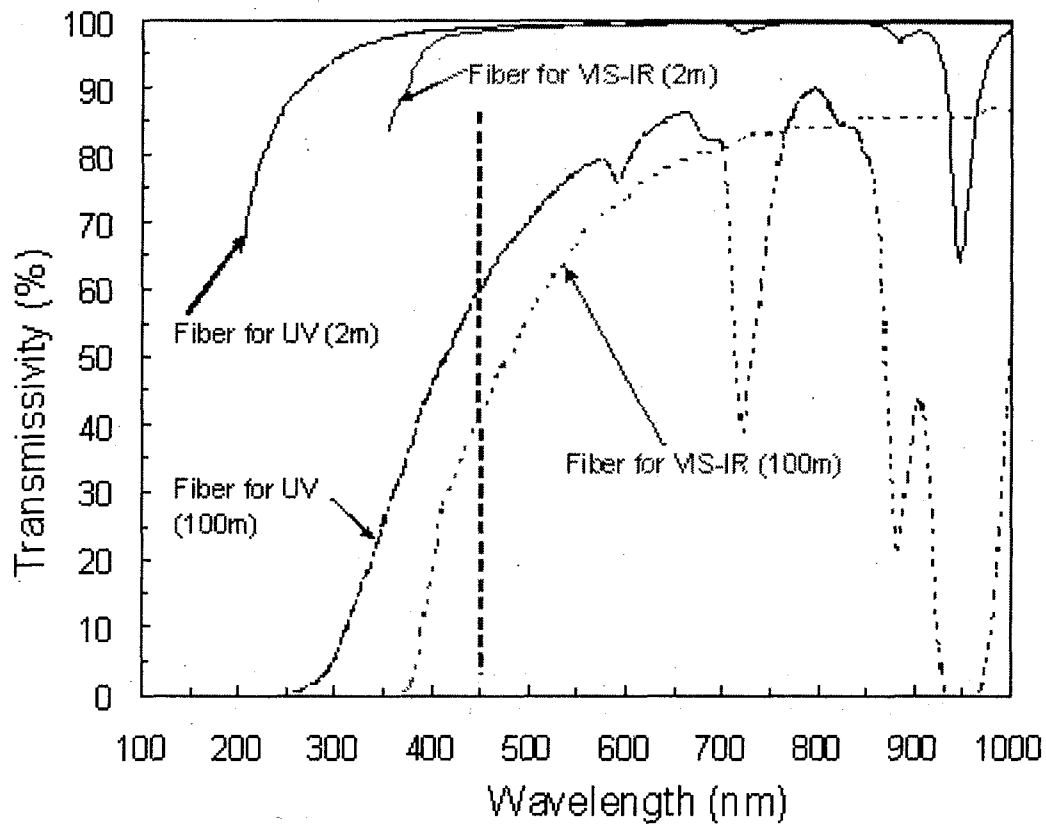
Fig. 2.5.3-3 Transmissivities of typical optical fibers as a function of wavelength.
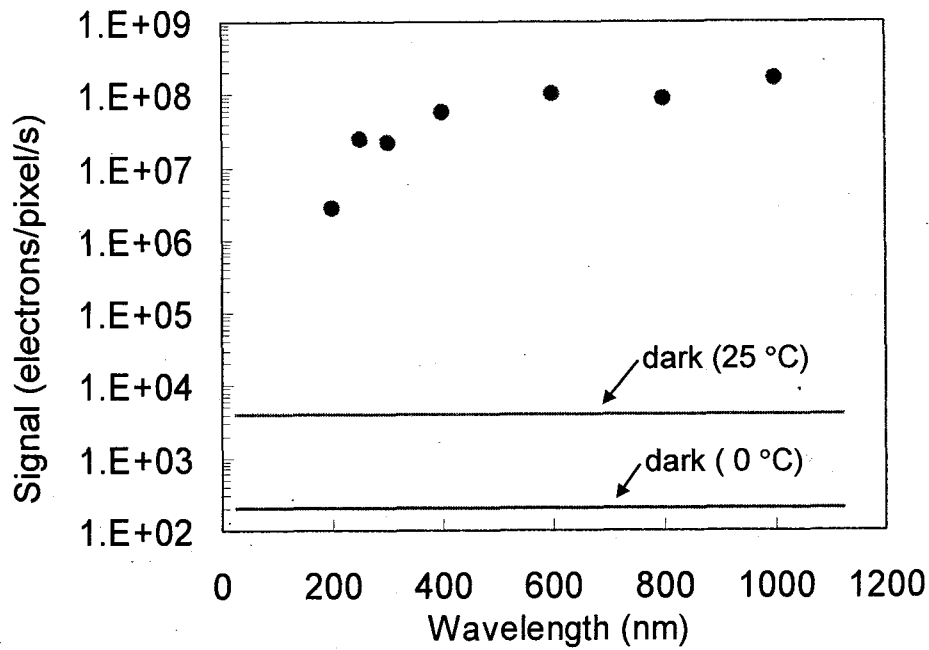
Fig. 2.5.3-4 Detected signal and dark count of detector.
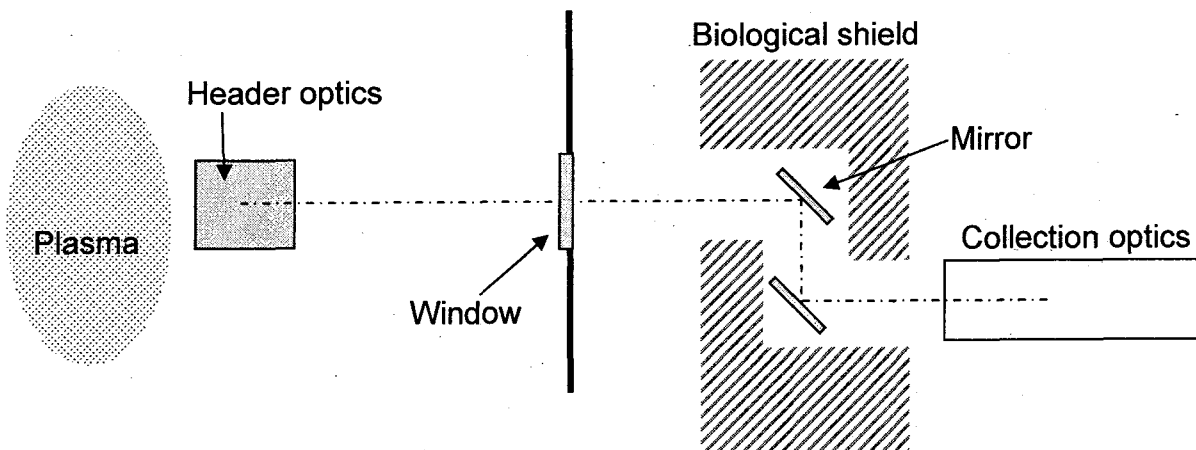
Fig. 2.6.1-1 Schematic view of optics for Impurity Influx Monitor (divertor). Optical alignment will be realized by tilting and shifting a mirror located in the biological shield.
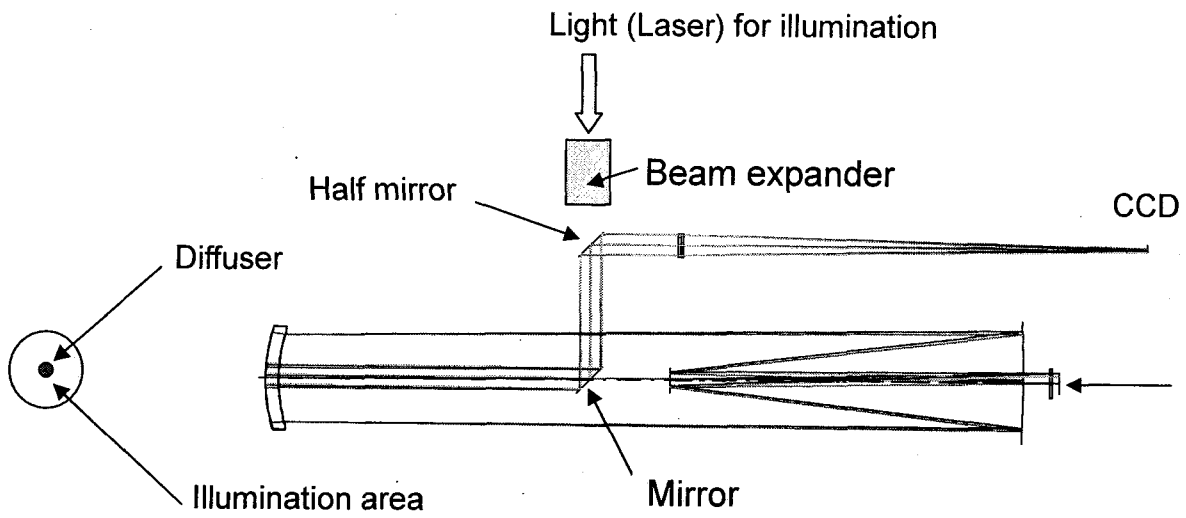
Fig. 2.6.1-2(a) Optical alignment system (a).
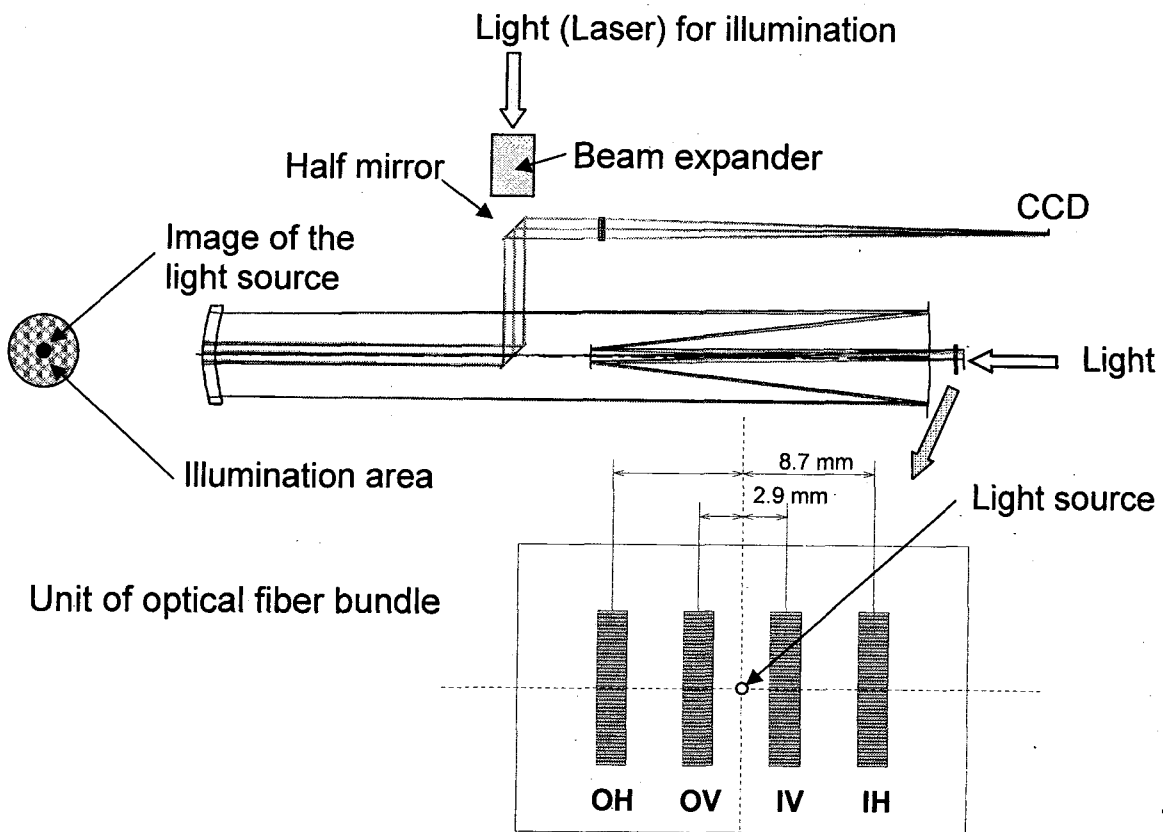
Fig. 2.6.1-2(b) Optical alignment system (b).

Off-axis aspherical mirror system

Aspherical mirror

Aspherical mirror

Optical fiber bundle

Cassegrain telescope

Lens

Spherical mirror

Field lens
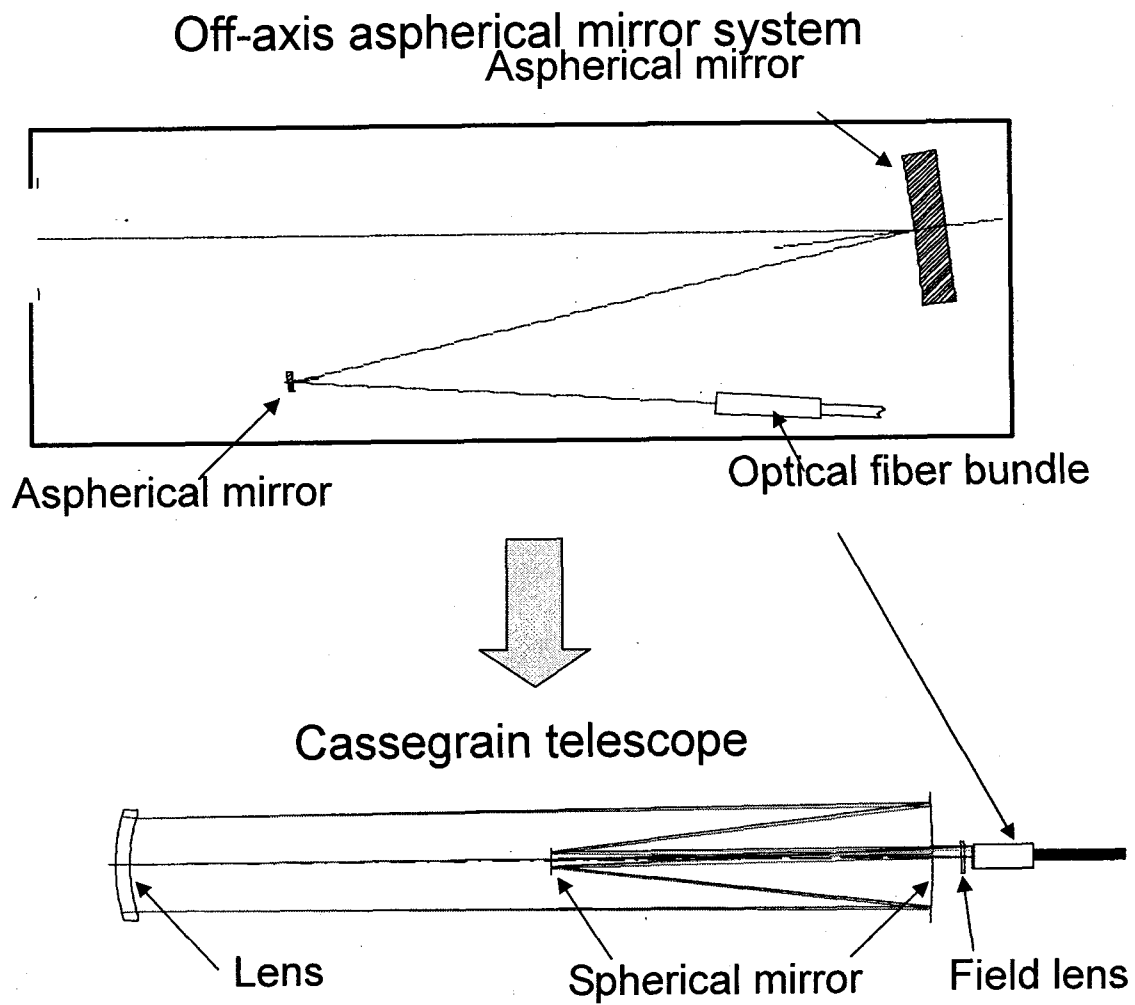
Fig. 2.6.2-1 Old and new design of collection optics.
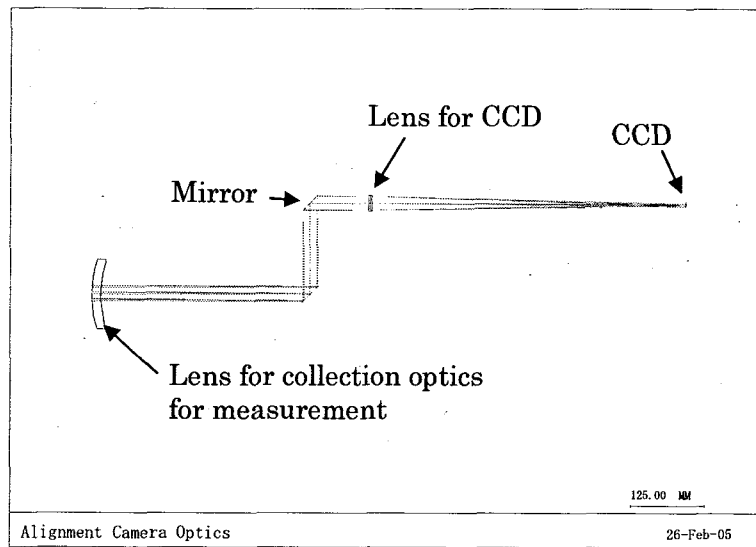
Fig. 2.6.2-2 Ray-trace of alignment system.
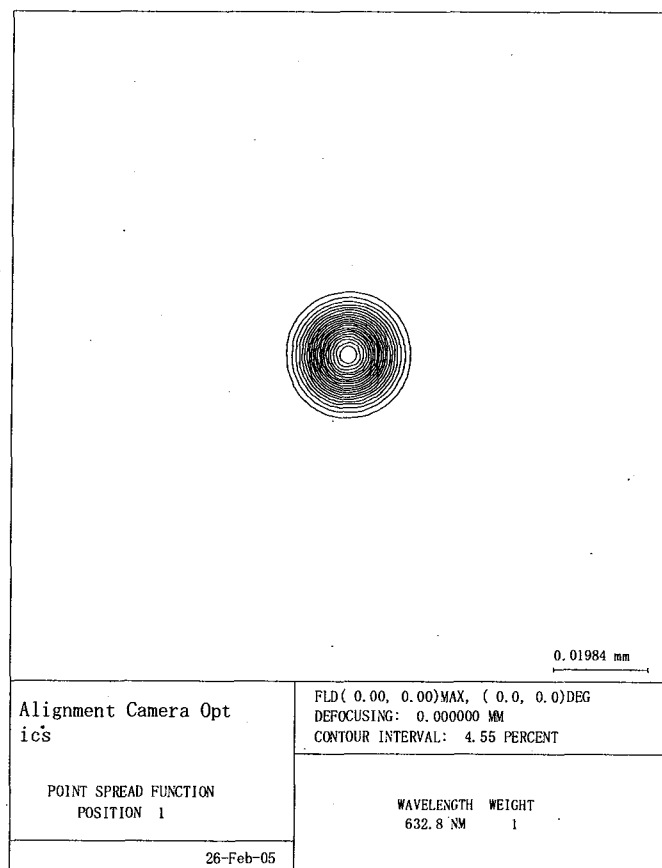
Fig. 2.6.2-3 Point spread function of the field 1 (y = 0 mm) on the CCD of alignment system.
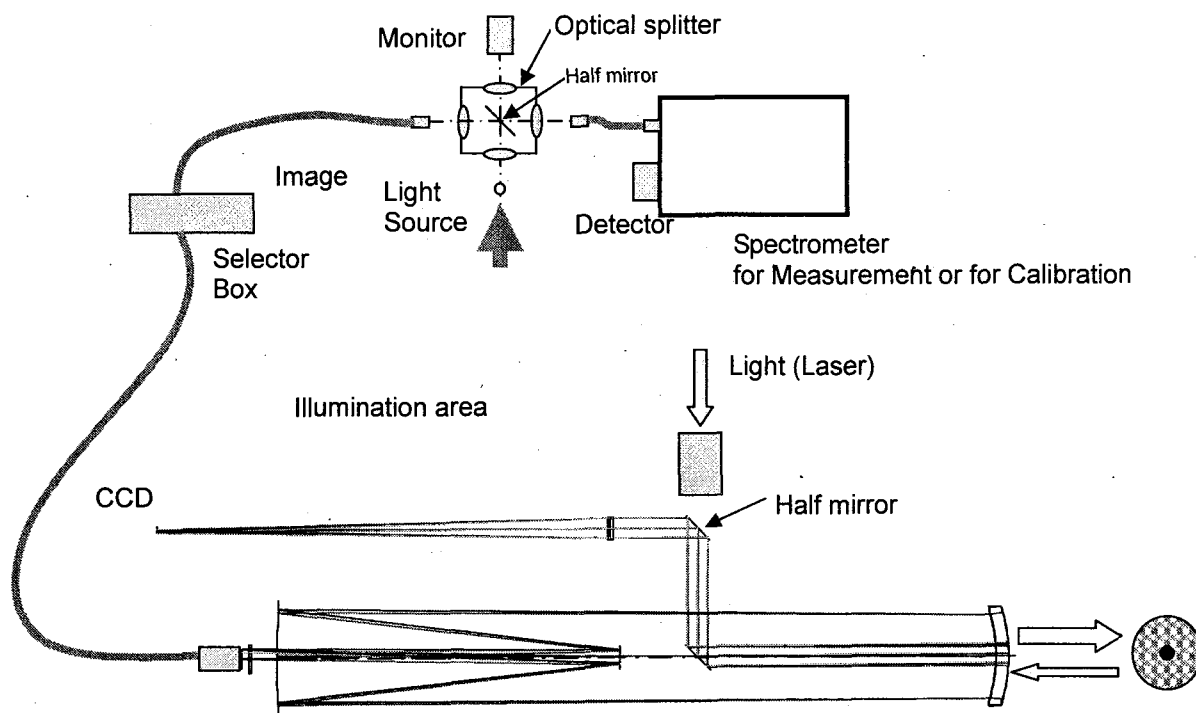
Fig. 2.7-1 Integration of optical systems for plasma measurement, calibration, alignment and focusing.
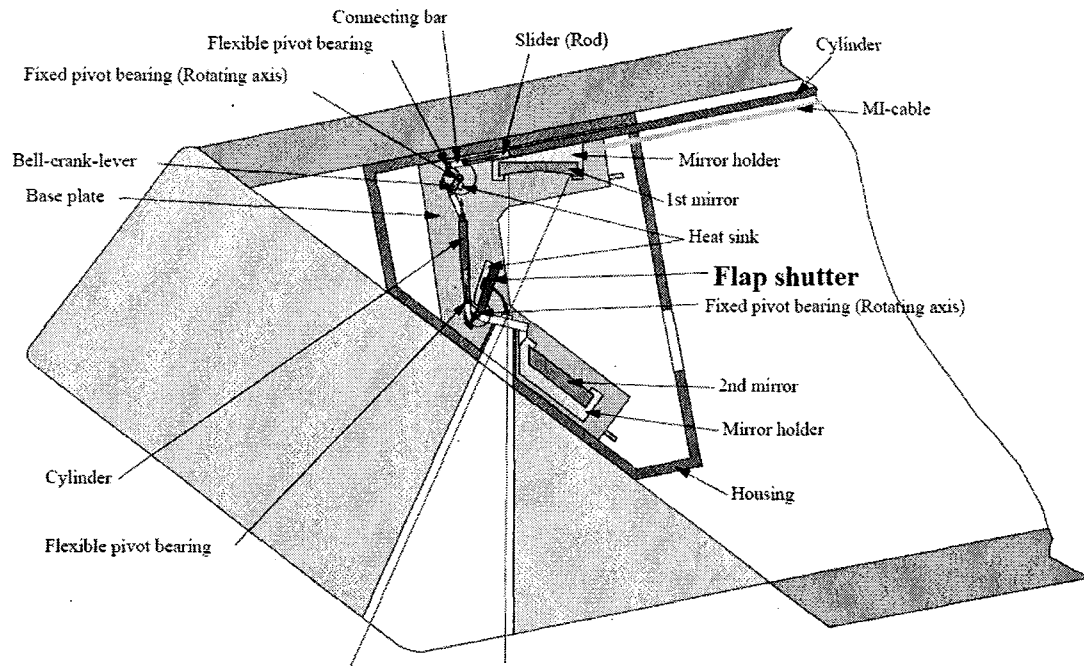
Fig.2.8-1(a) Schematic diagram of the flap type shutter mechanism installed in the upper port plug.
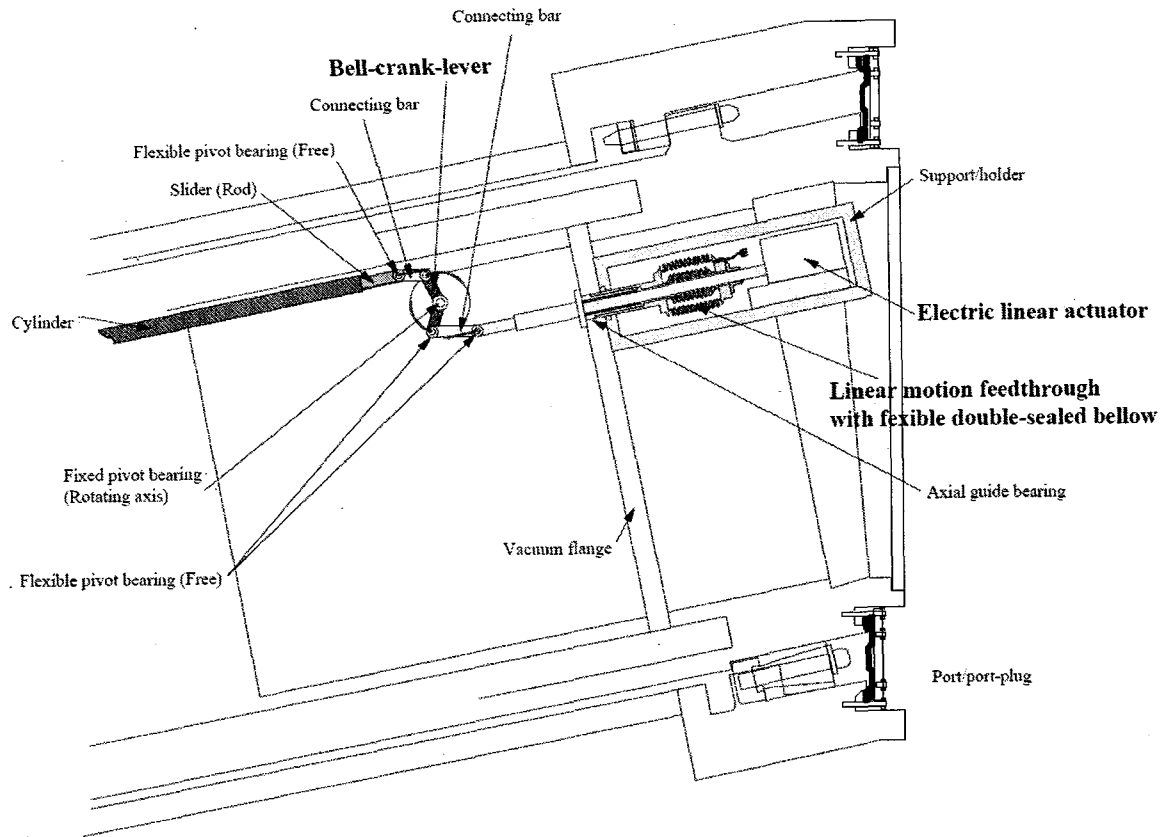
Fig.2.8-1(b) Schematic diagram of the driving mechanism (electric linear actuator, double-sealed bellow linear motion feedthrough and bell-crank-lever, etc.) of the flap type shutter mechanism installed in the upper port plug.
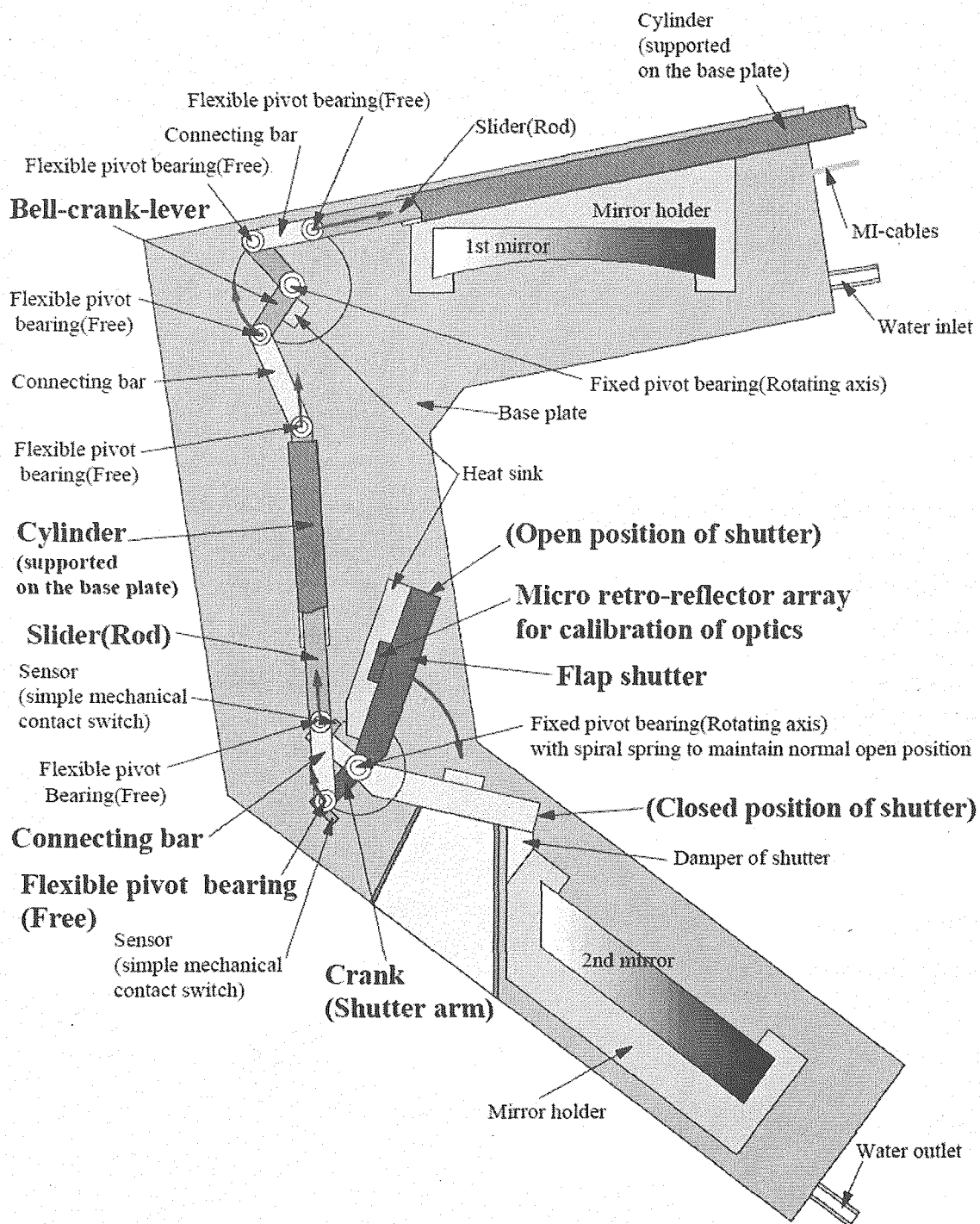
Fig.2.8-1(c) Main parts of the flap type shutter mechanism installed in the upper port plug.
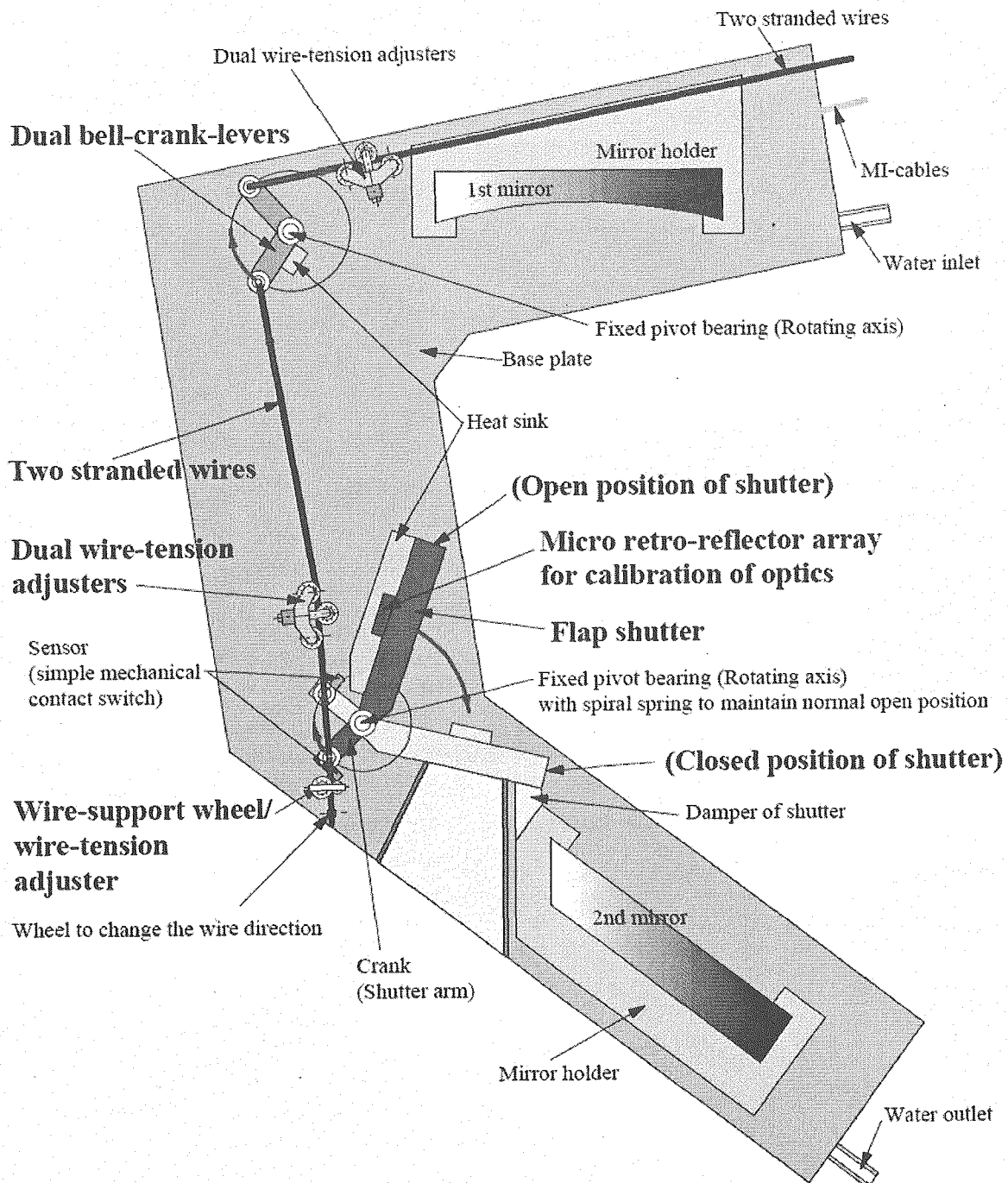
Fig.2.8-1(d) Main parts of the flap type shutter mechanism installed in the upper port plug. Stranded wires, dual wire-tension adjusters, dual bell-crank-levers, etc. are used as the driving mechanism.
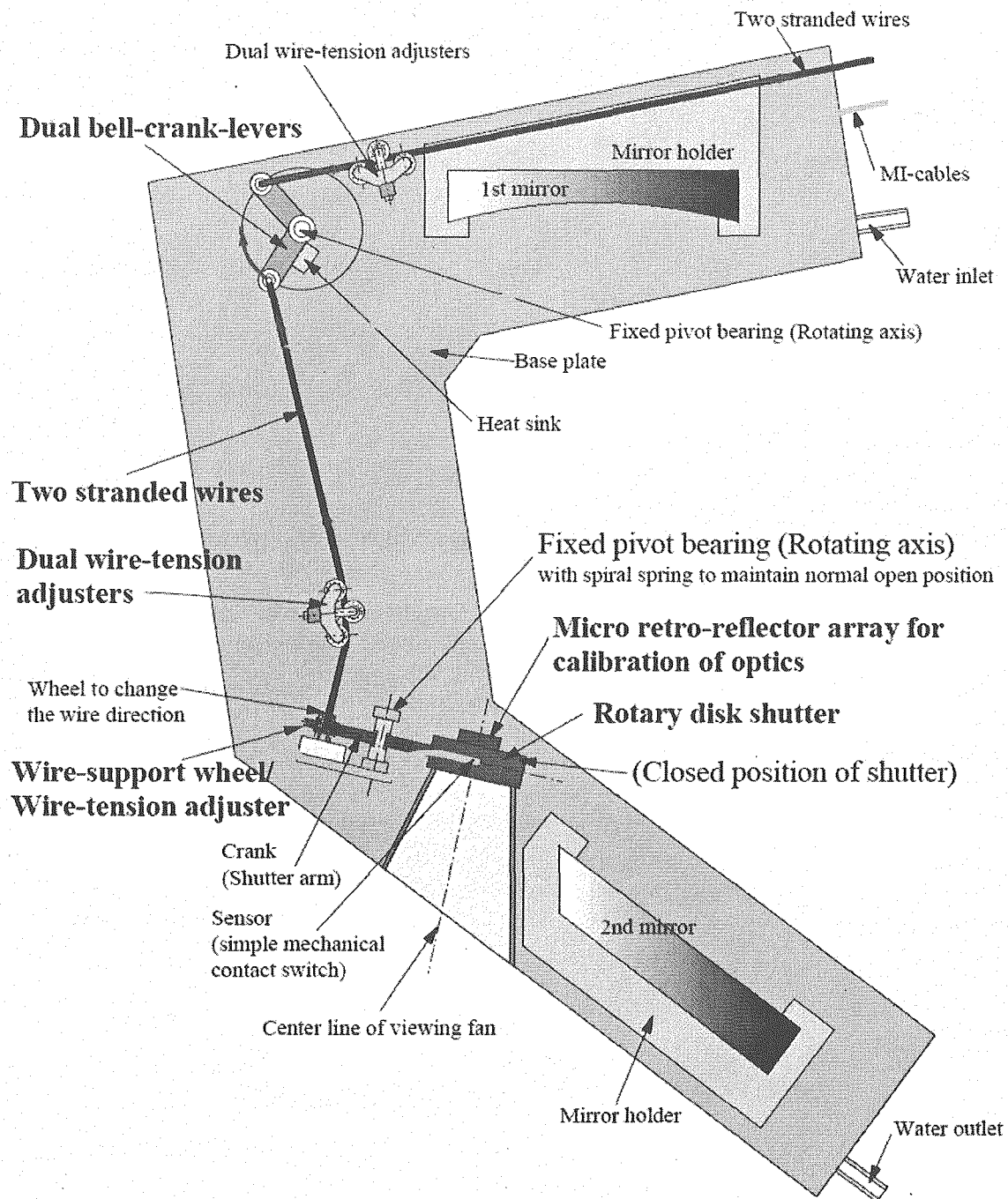
Fig.2.8-2(a) Main parts of the rotary disk type shutter mechanism installed in the upper port plug. Stranded wires, dual wire-tension adjusters, dual bell-crank-levers, wire-support wheel/wire-tension adjuster etc. are used as the driving mechanism.

Top View

Sensor
(simple mechanical
contact switch)

(Open position of shutter)

Wheel to change the wire
direction

Wire-support
wheeel/
wire-tension
adjusters

~50 degrees

(Closed position of shutter)

Crank
(Shutter arm)

Micro retro-reflector
array for calibration
of optics

Stranded wires

Rotary disk shutter

Wire-support
wheeel/
wire-tension
adjusters

Heat sink

Sensor
(simple mechanical
contact switch)

Fixed pivot bearing(Rotating axis)
with spiral spring to maintain normal open position

Wheel to change the wire
direction

Side View

Stranded wires

Micro retro-reflector array
for calibration of optics

Wheel to change the wire
direction

Crank
(Shutter arm)

Wire-tension
adjusters

Rotary disk shutter

Sensor
(simple mechanical
contact switch)

Heat sink

Fixed pivot bearing (Rotating axis)
with spiral spring to maintain normal open position

Fig.2.8-2(b) Schematic diagram of the top and side views of the rotary disk shutter, and the part of the driving mechanism.

**Expanded picture of dual wire-winding mechanism
(from the viewpoint of the direction of the A-arrow)**

Wheels to wind wire

Wire-support wheel

Worm gear

Stranded wire for open

Worm gear shaft

Stranded wire for close

A

Two stranded wires

Dual wire-tension adjusters

Worm gear

Dual wheels to change
the wire direction

Rotary feedthrough

Vacuum flange

Stranded wires

Dual wheels to wind wire

Support/holder

Electric stepping motor

Port/port-plug
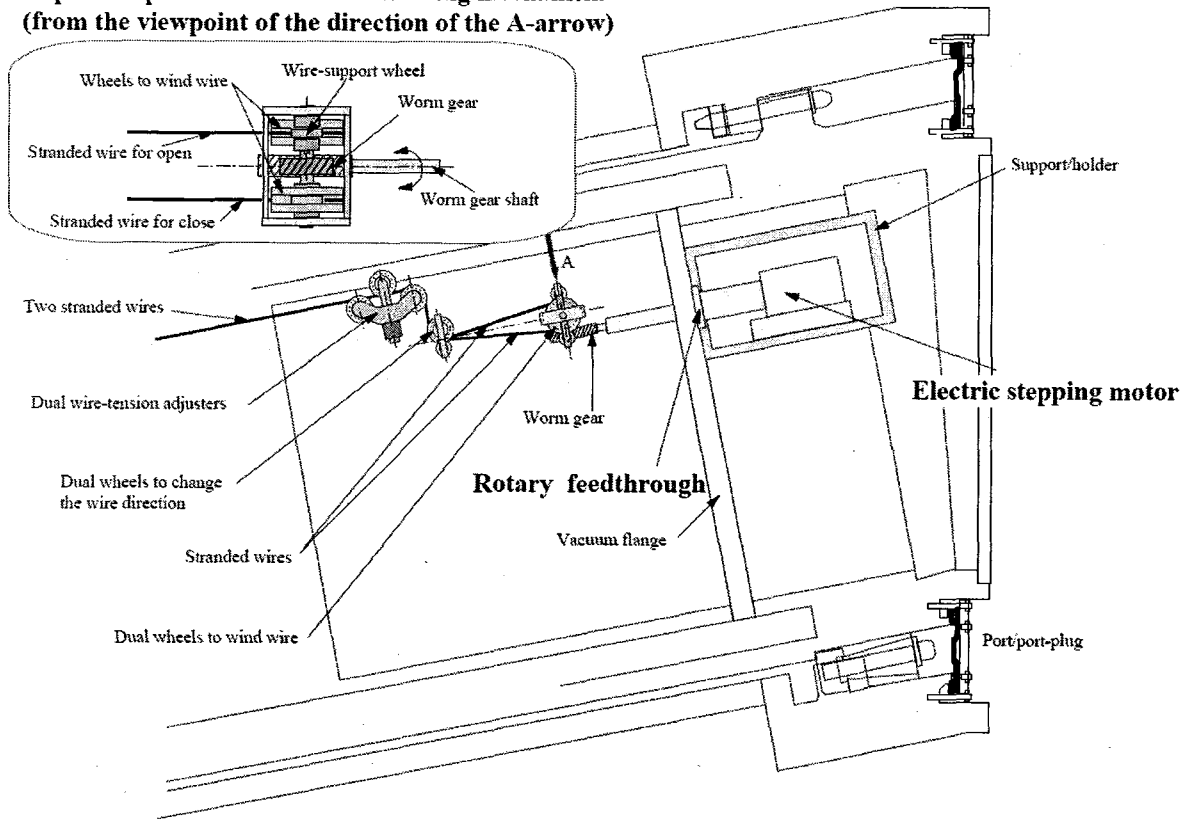
Fig.2.8-2(c) Schematic diagram of the wire-winding mechanism, rotary feedthrough, electric stepping motor, etc., which are the parts of the driving mechanism of the shutter.
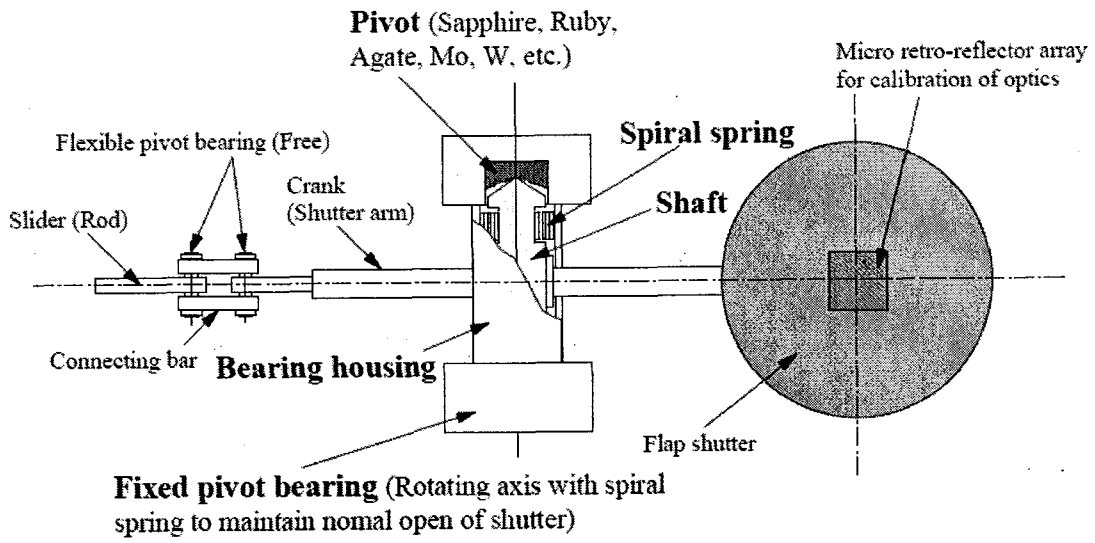
Fig.2.8-3 Schematic diagram of the fixed pivot bearing of the shutter.
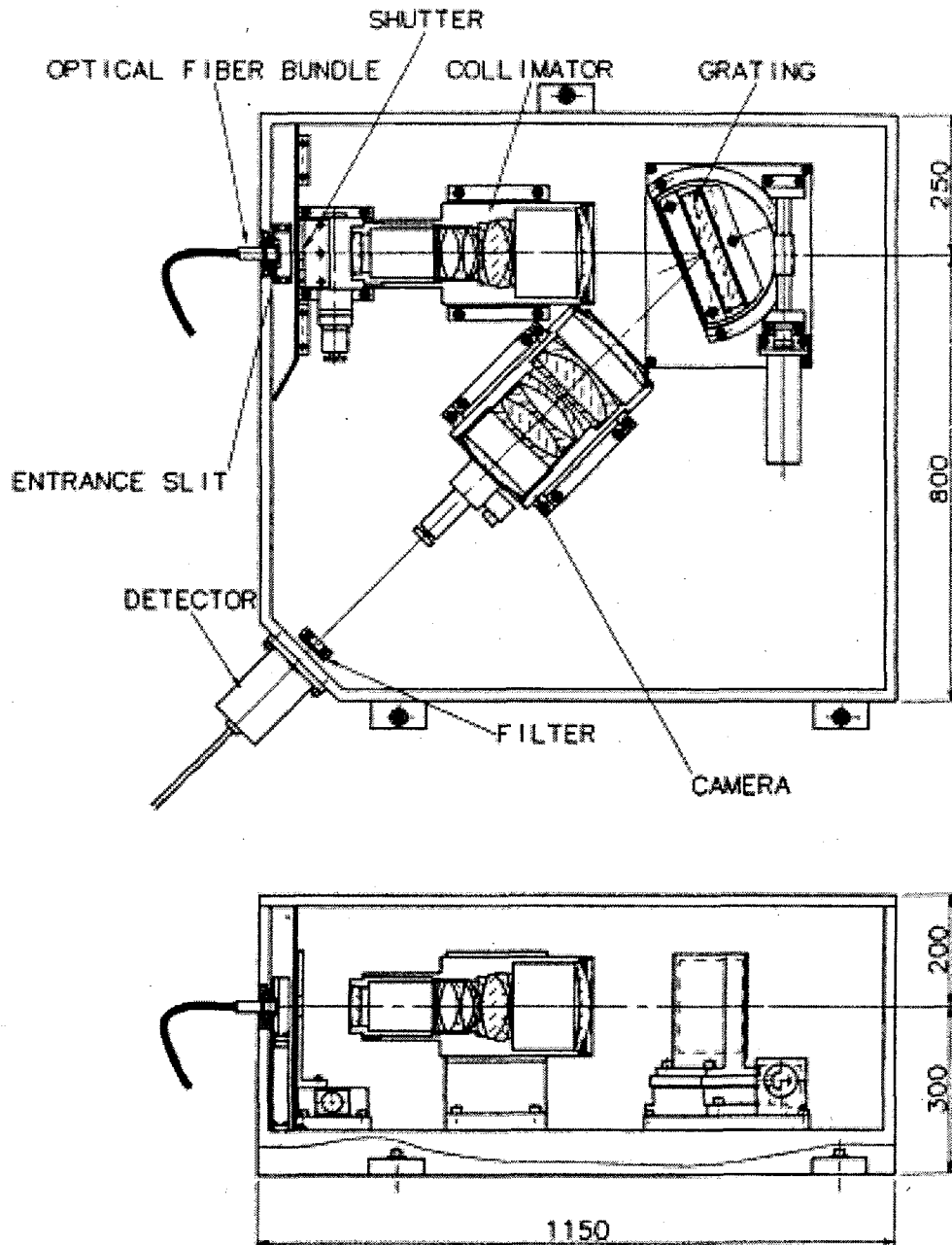
Fig. 3.2-1 Visible Survey Spectrometer (VSS) for UV
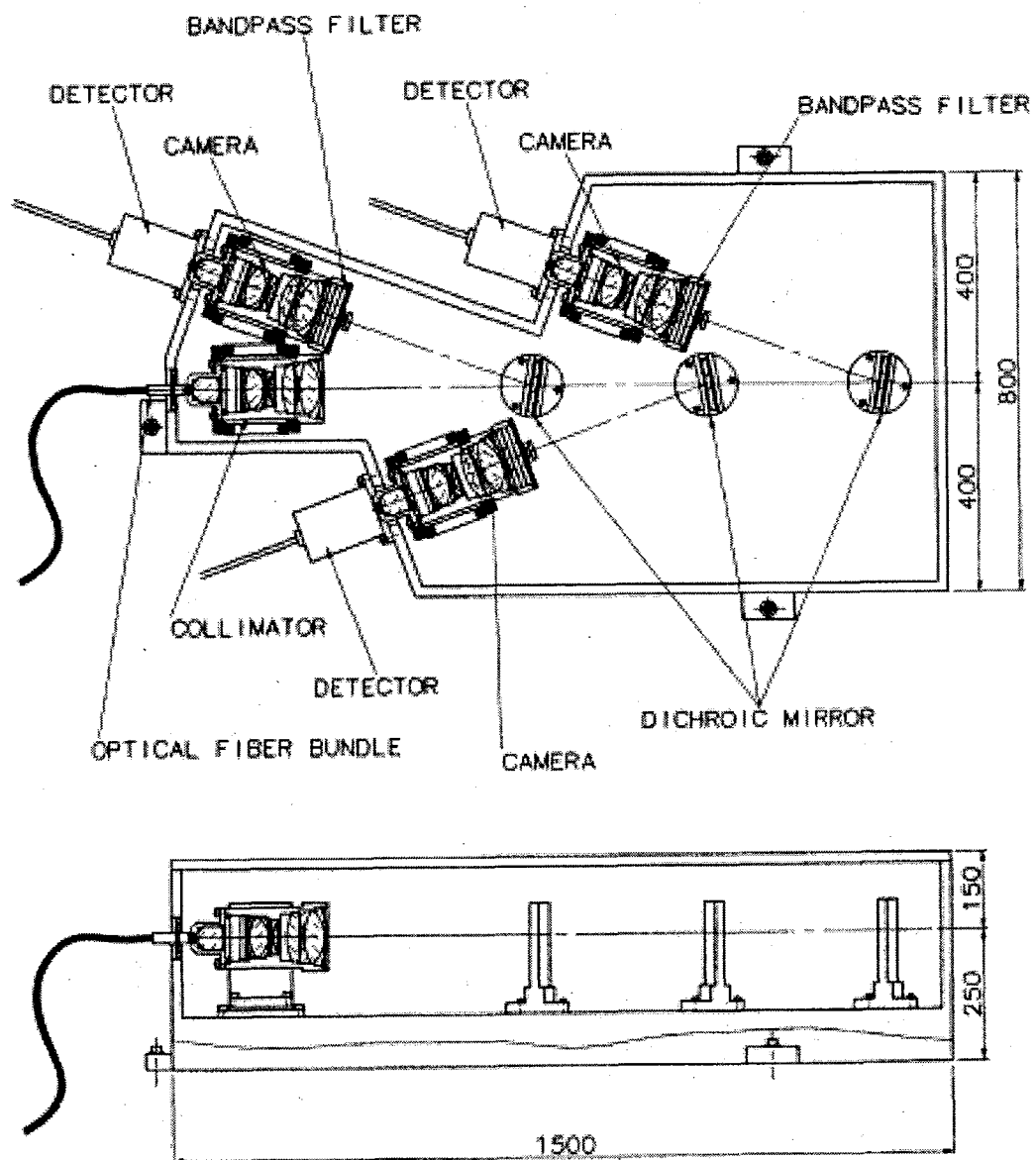
Fig. 3.2-2 Filter Spectrometer (FS) for UV region
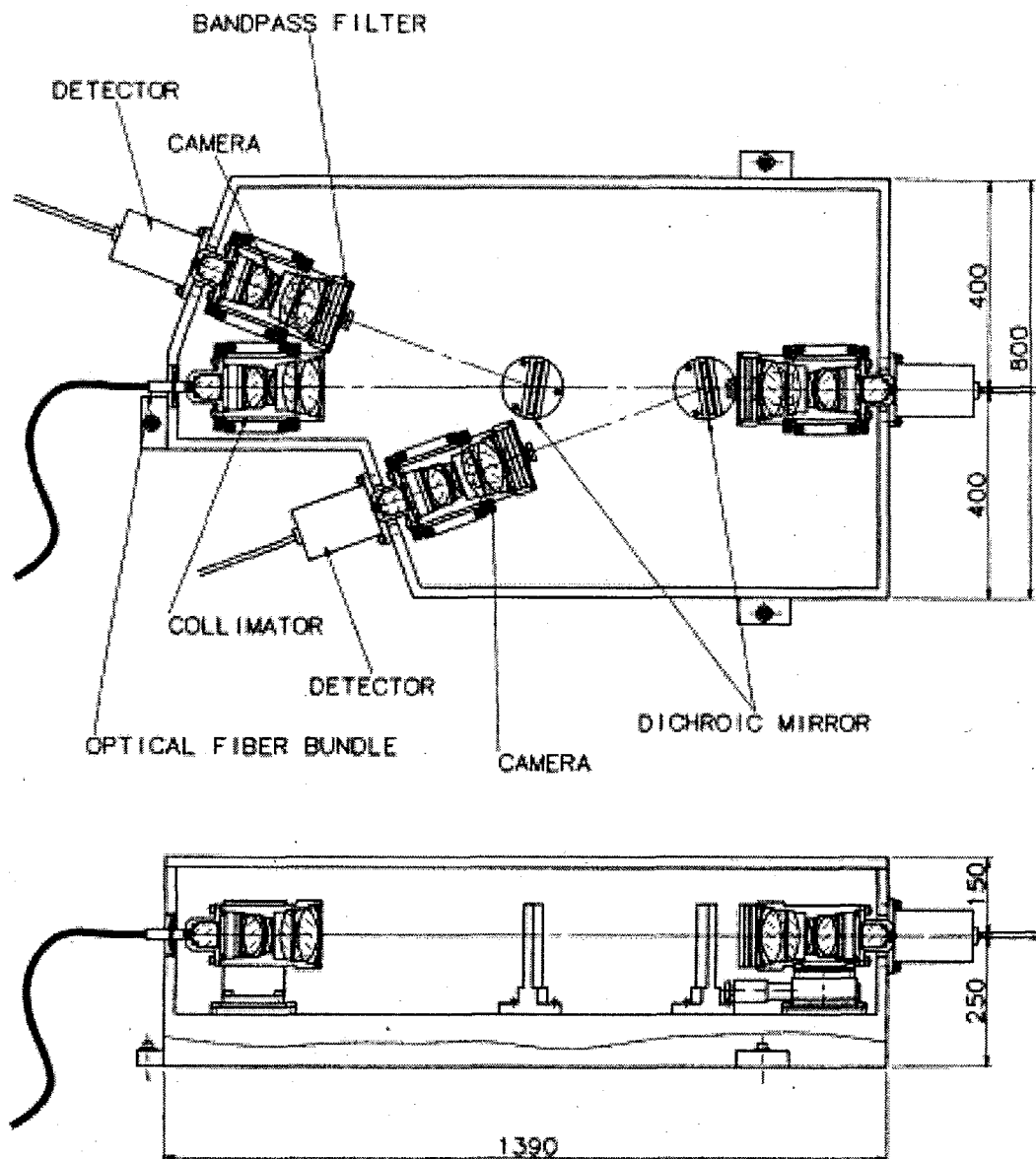
Fig. 3.2-3 Filter spectrometer (FS) for visible region
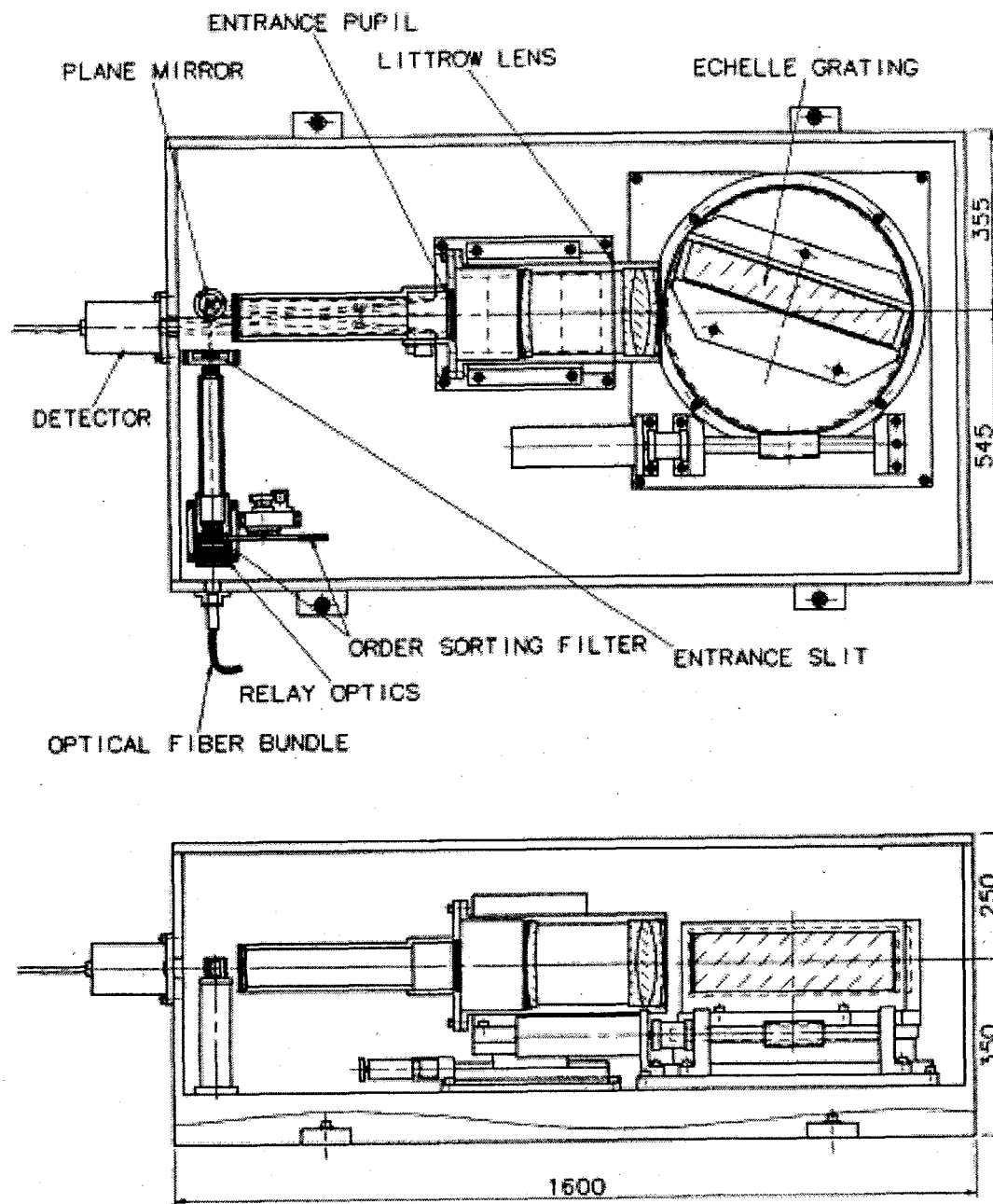
Fig. 3.2-4 High dispersion spectrometer (HDS)

DETAIL OF ELEMENTS ENCIRCLED
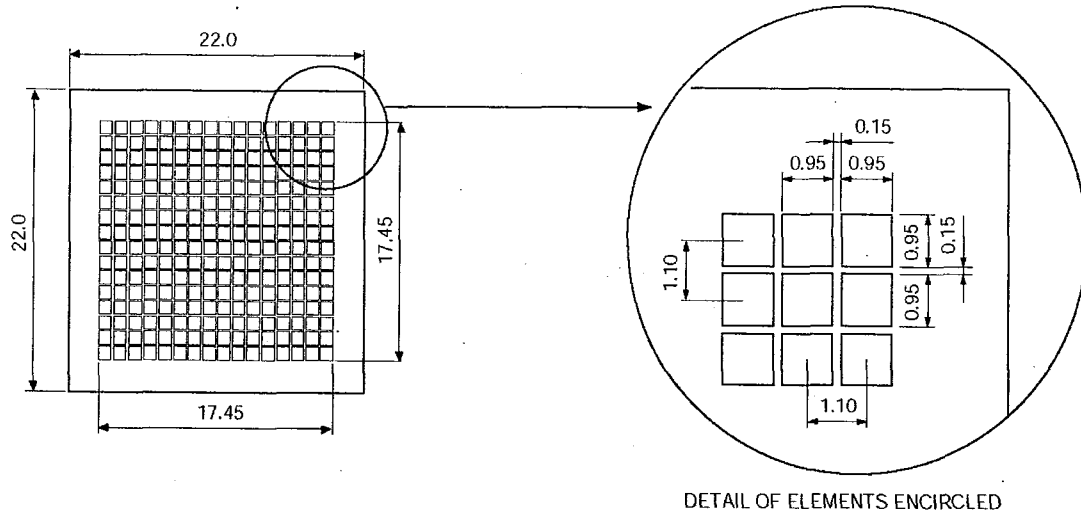
Fig. 3.3.1-1 Magnification Figure of Active Area
(C4675)
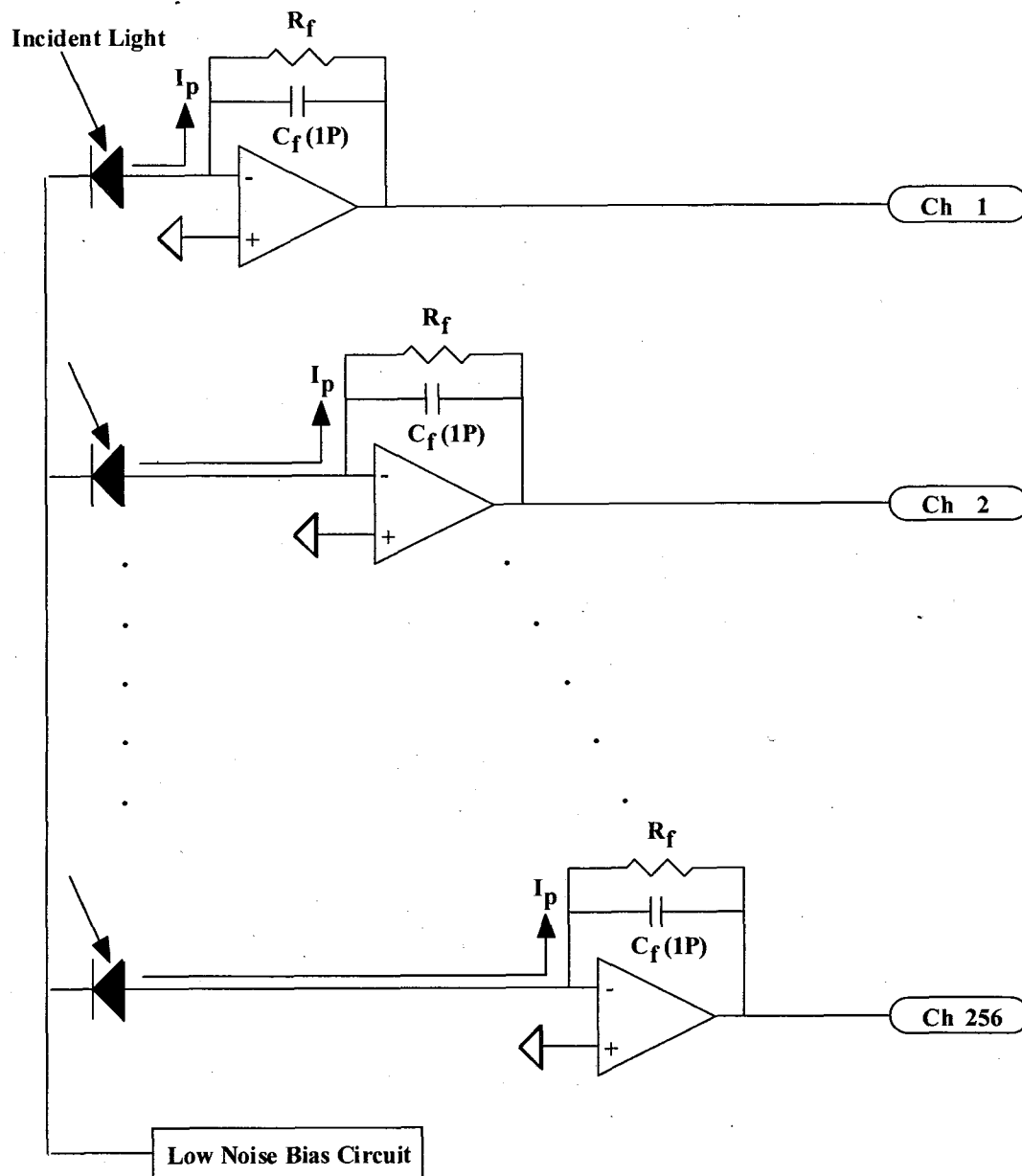
Fig. 3.3.1-2 Block Diagram of C4675 Detector
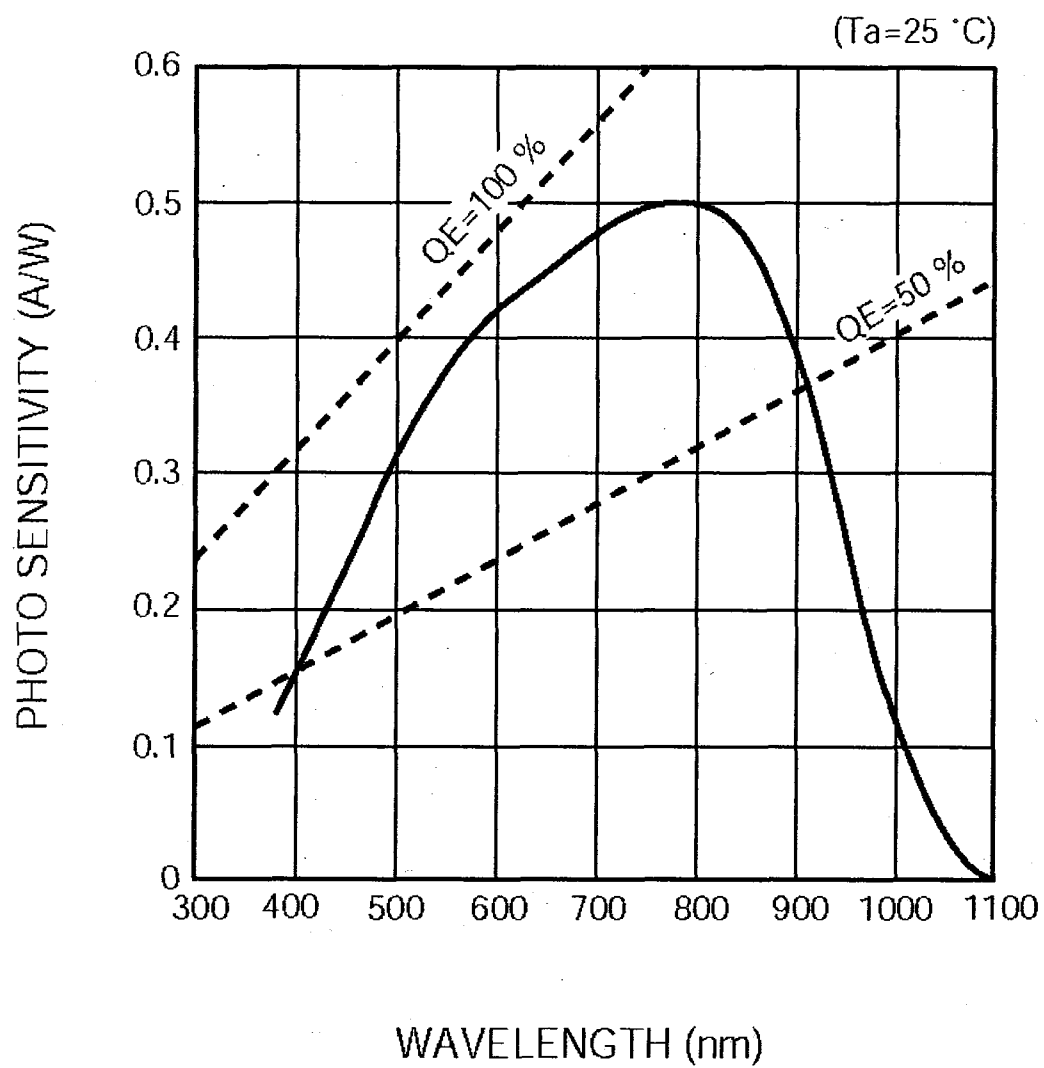
Fig. 3.3.1-3 Photosensitivity of S4529

136

136

2.5

151

φ94

HAMAMATSU **C4675-xxx**

PCD80 (4 x) M3 DEPTH 4

7.1 (FOCAL PLANE)

CN. 1

CN. 4

CN. 2

CN. 3

CN1 to CN4
(KEL, 8850-080-170L)
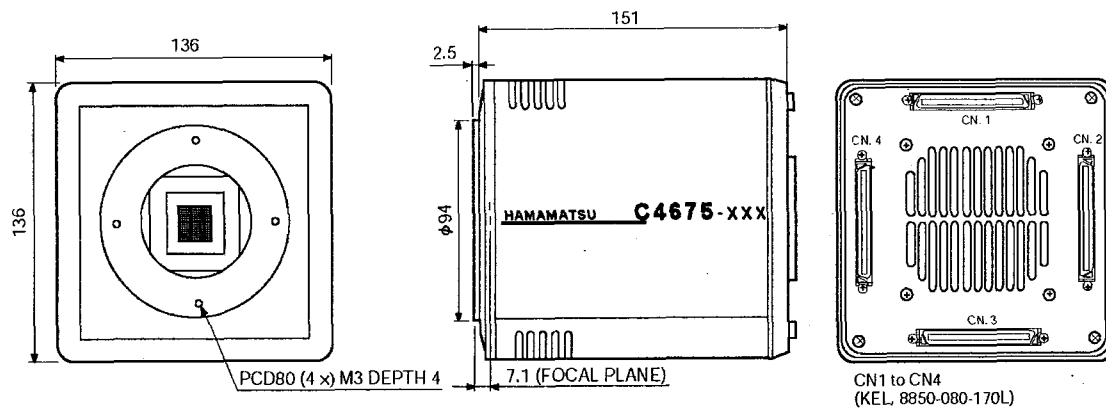
Fig. 3.3.1-4 Dimensional Outline of C4675
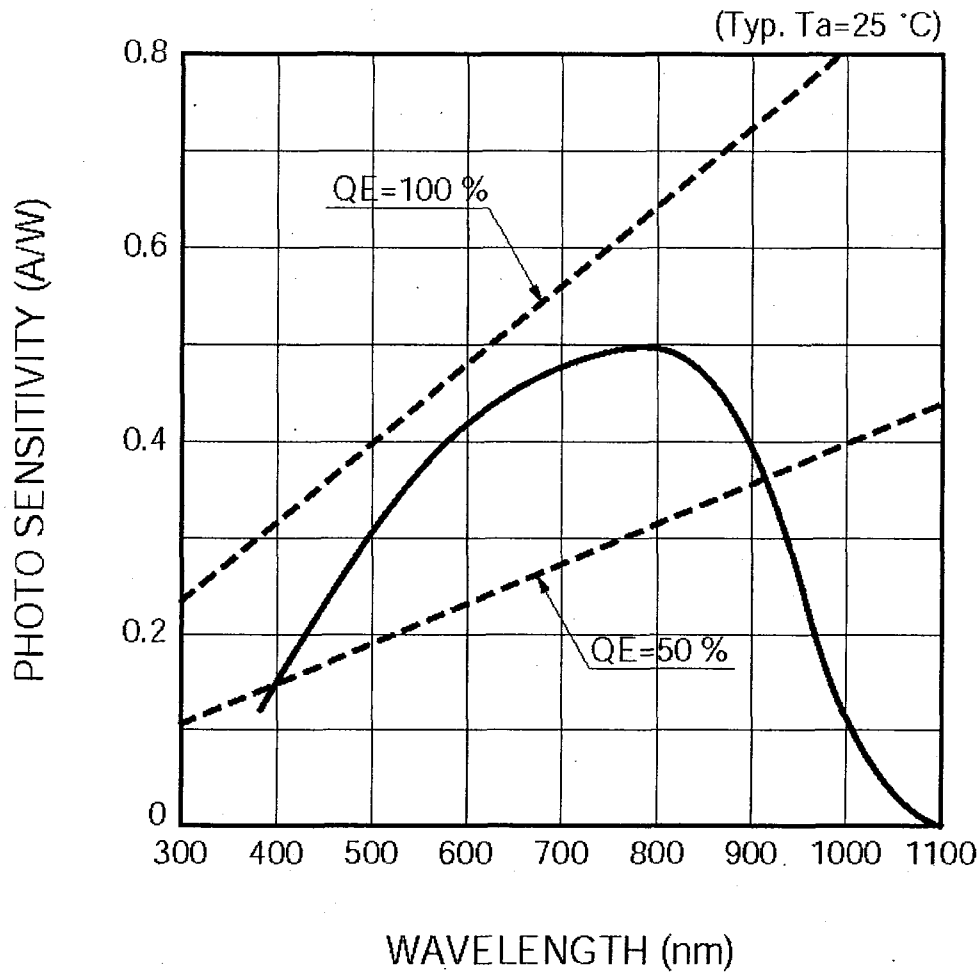
Fig. 3.3.1-5 Photosensitivity of S3805

Active Area of S3805
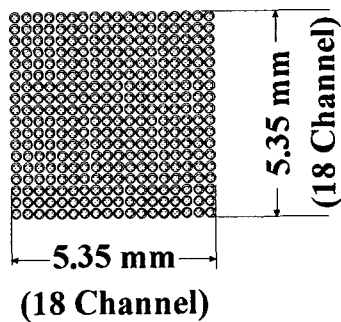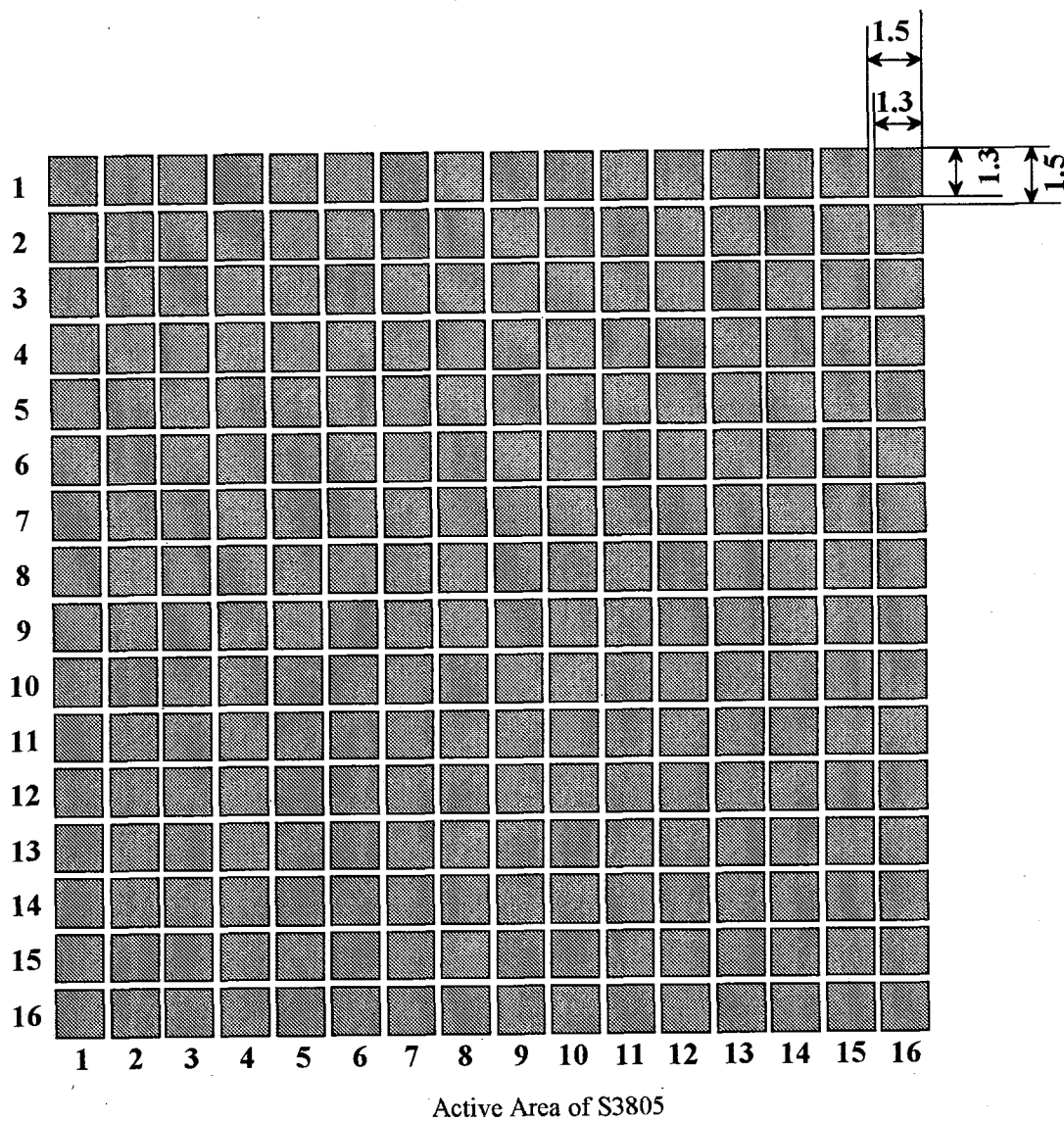
Image of Optical Fiber Array on the Detector

Fig. 3.3.1-6 Magnification Figure of Active Area (S3805) and Image of Optical Fiber Array
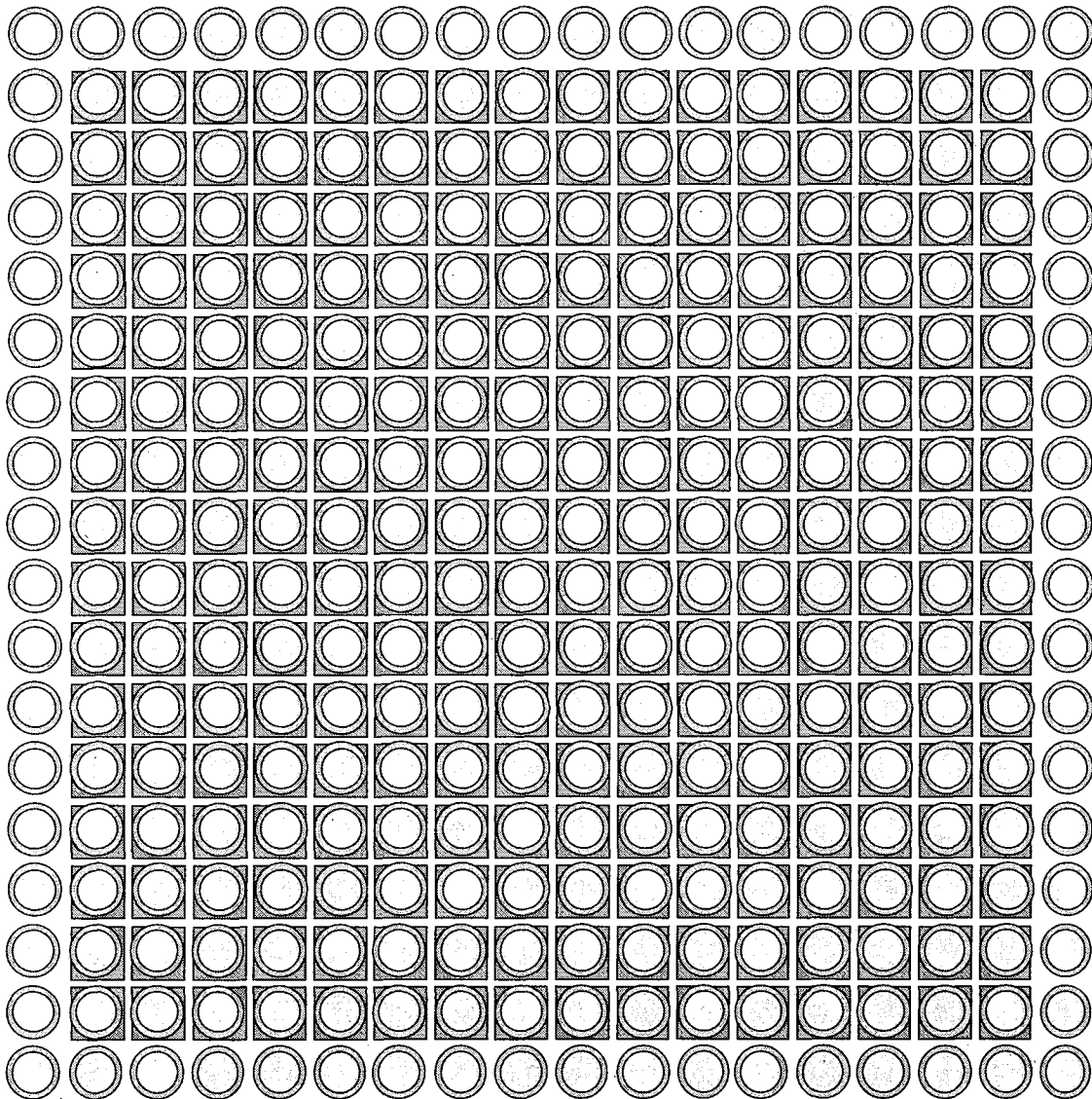
Fig. 3.3.1-7 Coupling of Fiber array and S3805 detector
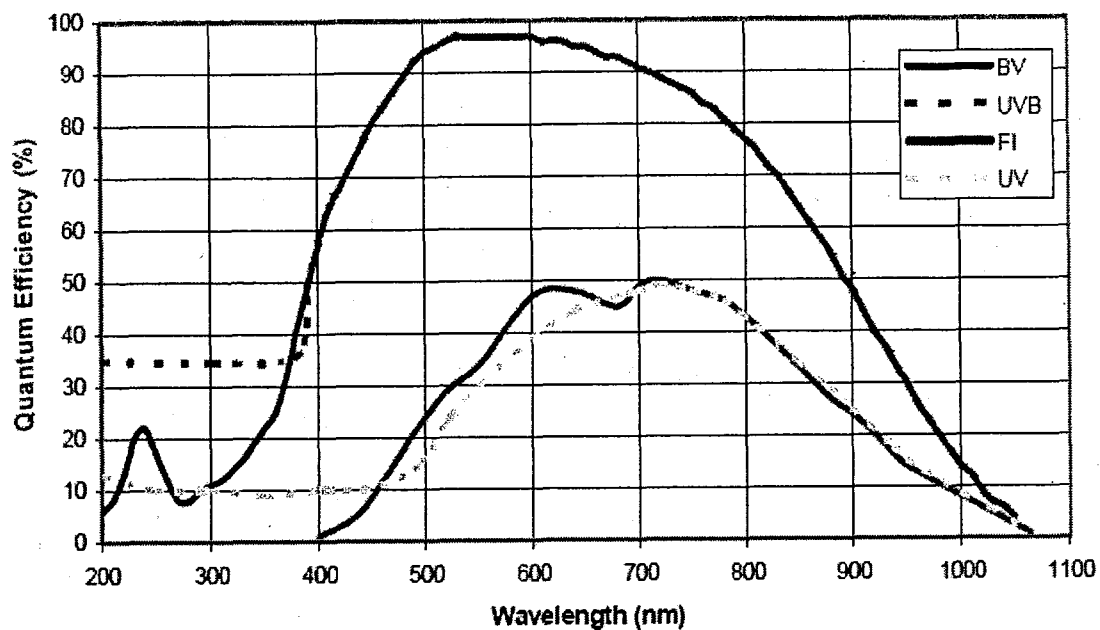
Fig. 3.3.2-1 (a) Quantum Efficiency at +25 °C
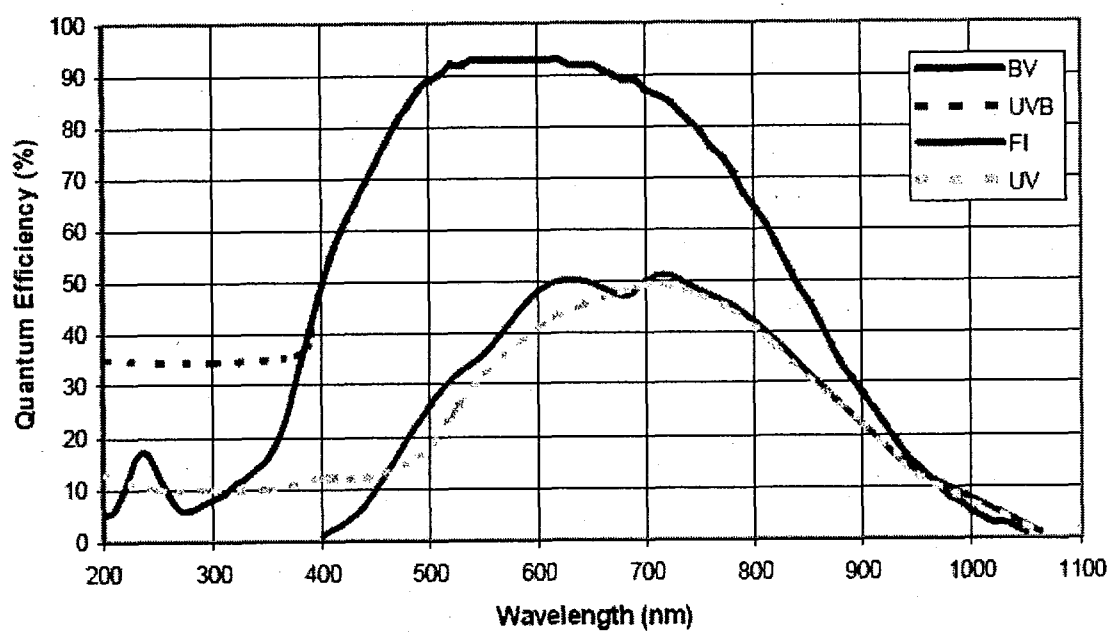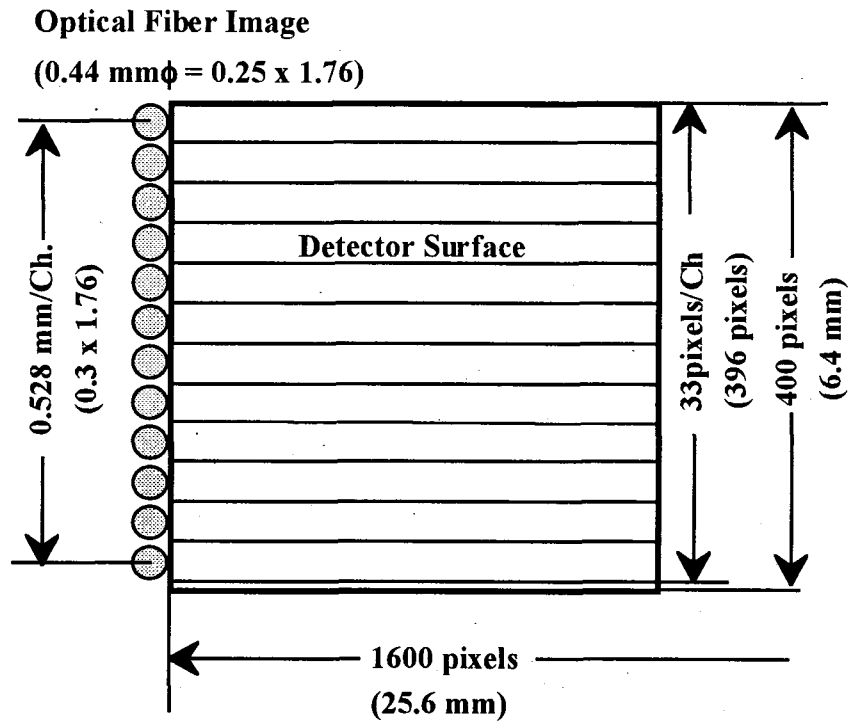

Fig. 3.3.2-1(b) Quantum Efficiency at － 100 °C

Optical Fiber Image

(0.44 mmφ = 0.25 x 1.76)

Detector Surface

0.528 mm/Ch.
(0.3 x 1.76)

33pixels/Ch
(396 pixels)

400 pixels
(6.4 mm)

1600 pixels
(25.6 mm)

Fig.3.3.2-2 Coupling of Fiber array and DU971N detector
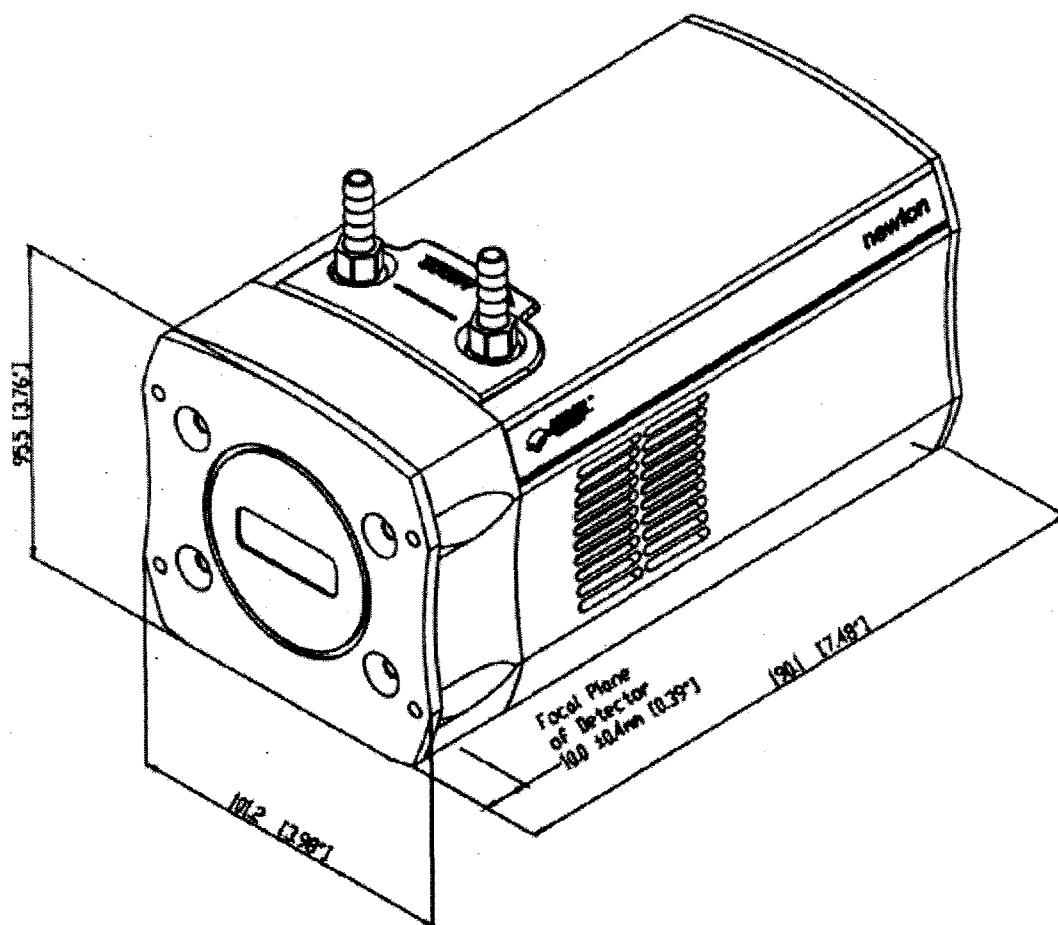
Fig. 3.3.2-3 Schematic Drawing of DU741N

① Superconductingmagnet
② Laser diode(LD,680nm)
③ Interferometer
④ Objective lens
⑤ CCD camera
⑥ VTR system
⑦ Temperature control unit
⑧ LD driver
⑨ Magnetic field controller
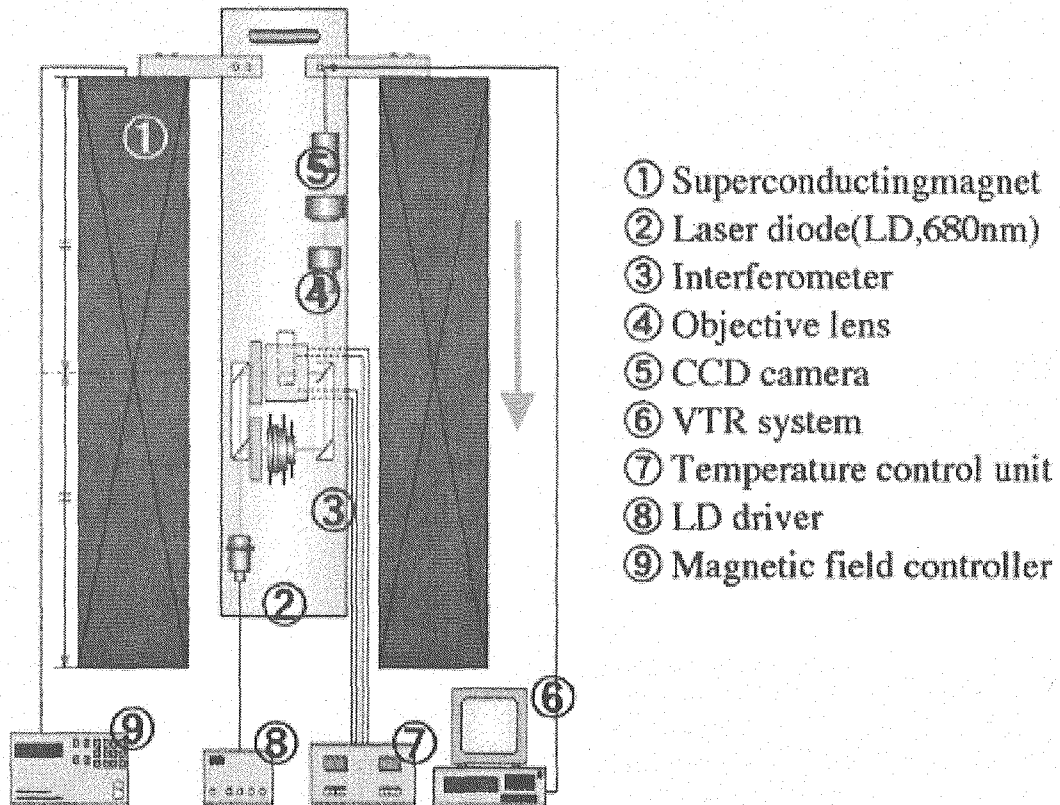
Fig. 3.3.3-1 Experimental Apparatus of Microscope System Prepared for Observation of Orientation of Amino Acid Crystal in the Magnetic Field
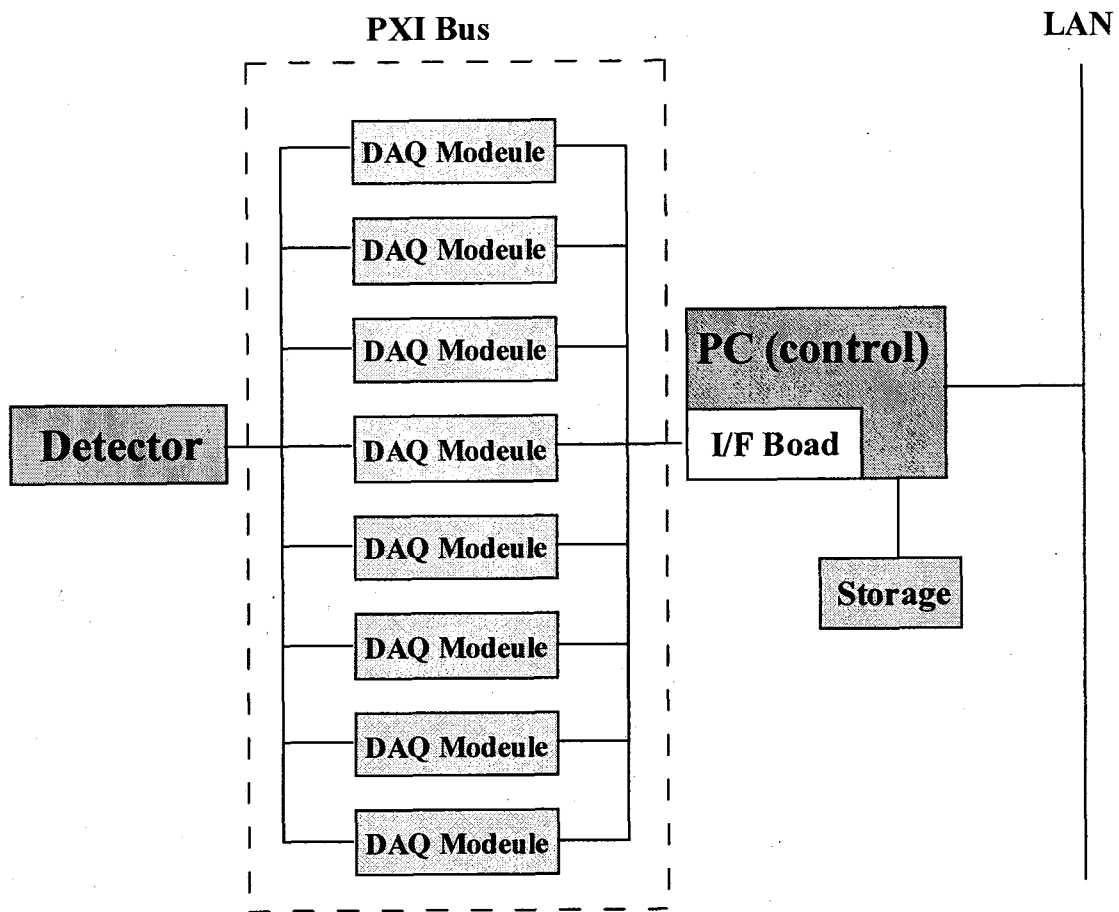
(K. Ogawa,et al., J. Che. Emg. Jp. 35 (2002) 1123.)

PXI Bus   **LAN**

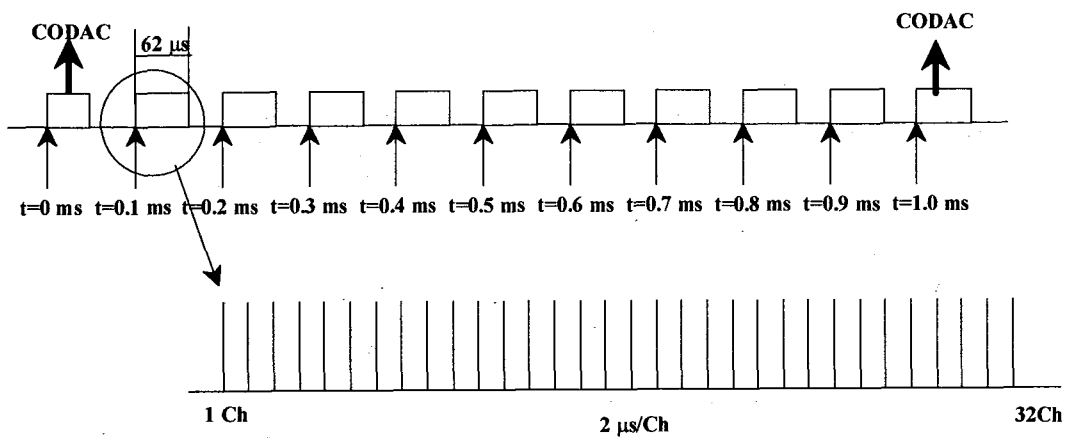Fig. 3.5-1 Data Acquisition System for Fiber Spectrometer

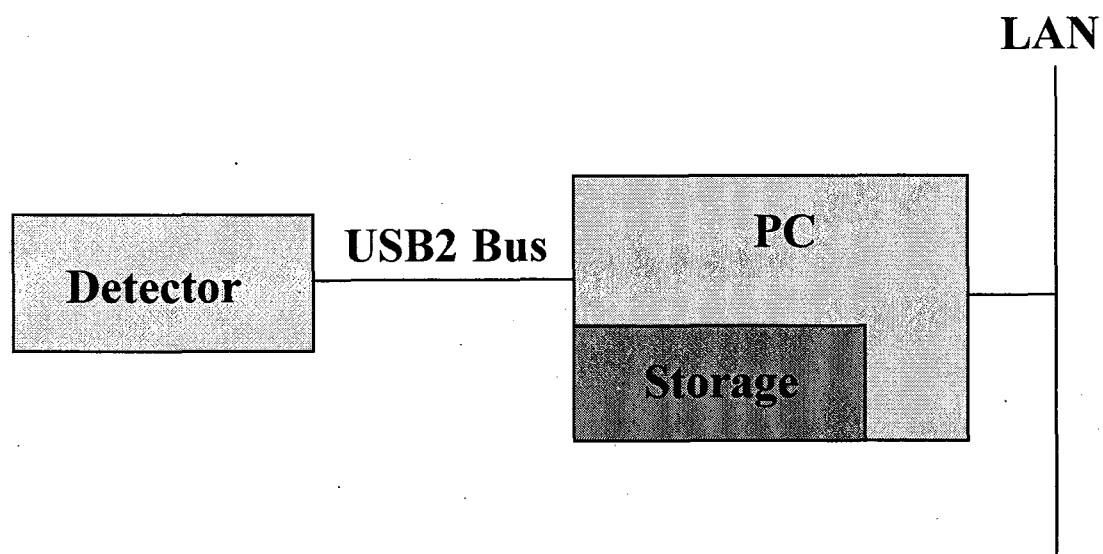Fig. 3.5-2 Data Flow in Fiber Spectrometer

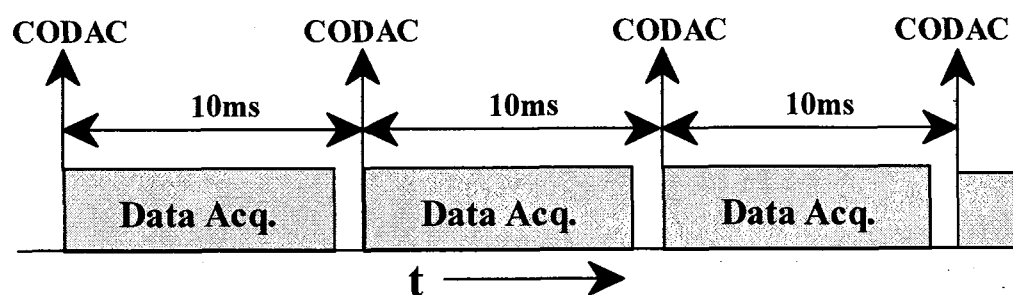Fig. 3.5-3 Data Acquisition System of Visible Survey and High Dispersion Spectroscopy

Fig. 3.5-4 Data Flow of Data Acquisition System of Visible Survey and High Dispersion Spectroscopy